Uncertainty Analysis and Robust Optimization of a Single Pore in a Heterogeneous Catalytic Flow Reactor System

by

Donovan Chaffart

A thesis

presented to the University of Waterloo

in fulfilment of the

thesis requirement for the degree of

Masters of Applied Science

in

Chemical Engineering

Waterloo, Ontario, Canada, 2017

Author's Declaration

I hereby declare that I am the sole author of this thesis. This is a true copy of the thesis, including any required final revisions, as accepted by my examiners.

I understand that my thesis may be made electronically available to the public.

Abstract

Catalytic systems are crucial to a wide number of chemical production processes, and as a result there is significant demand to develop novel catalyst materials and to optimize existing catalytic reactor systems. These optimization and design studies are most readily implemented using model-based approaches, which require less time and fewer resources than the alternative experimental-based approaches. The behaviour of a catalytic reactor system can be captured using multiscale modeling approaches that combine continuum transport equations with kinetic modeling approaches such as kinetic Monte Carlo (kMC) or the mean-field (MF) approximation in order to model the relevant reactor phenomena on the length and time scales on which they occur. These multiscale modeling approaches are able to accurately capture the reactor behaviour and can be readily implemented to perform robust optimization and process improvement studies on catalytic reaction systems. The problem with multiscale-based optimization of catalytic reactor systems, however, is that this is still an emerging field and there still remain a number of challenges that hinder these methods. One such challenge involves the computational cost. Multiscale modeling approaches can be computationally-intensive, which limit their application to model-based optimization processes. These computational burdens typically stem from the use of fine-scale models that lack closed-form expressions, such as kMC. A second common challenge involves model-plant mismatch, which can hinder the accuracy of the model. This mismatch stems from uncertainty in the reaction pathways and from difficulties in obtaining the values of the system parameters from experimental results. In addition, the uncertainty in catalytic flow reactor systems can vary in space due to kinetic events not taken into consideration by the multiscale model, such as non-uniform catalyst deactivation due to poisoning and fouling mechanisms. Failure to adequately account for model-plant mismatch can result in substantial deviations from the predicted catalytic reactor performance and significant losses in reactor efficiency. Furthermore, uncertainty propagation techniques can be computationally intensive and can further increase the computational demands of the multiscale models.

Based on the above challenges, the objective of this research is to develop and implement efficient strategies that study the effects of parametric uncertainty in key parameters on the performance of a multiscale single-pore catalytic reactor system and subsequently to implement them to perform robust and dynamic optimization on the reactor system subject to uncertainty. To this end, low-order series expansions such as Polynomial Chaos Expansion (PCE) and Power Series Expansion (PSE) were implemented in order to efficiently propagate parametric uncertainty through the multiscale reactor model. These uncertainty propagation techniques were used to perform extensive uncertainty analyses on the catalytic reactor system in order to observe the impact of parametric uncertainty in various key system parameters on the catalyst reactor performance. Subsequently, these tools were implemented into robust optimization formulations

that sought to maximize the reactor productivity and minimize the variability in the reactor performance due to uncertainty. The results highlight the significant effect of parametric uncertainty on the reactor performance and illustrate how they can be accommodated for when performing robust optimization.

In order to assess the impact of spatially-varying uncertainty due to catalyst deactivation on the catalytic reactor system, the uncertainty propagation techniques were applied to evaluate and compare the effects of spatially-constant and spatially-varying uncertainty distributions. To accommodate for the spatially-varying uncertainty, unique uncertainty descriptions were applied to each uncertain parameter at discretized points across the reactor length. The uncertainty comparison was furthermore extended through application to robust optimization. To reduce the computational cost, statistical data-driven models (DDMs) were identified to approximate the key statistical parameters (mean, variance, and probabilistic bounds) of the reactor output variability for each uncertainty distribution. The DDMs were incorporated into robust optimization formulations that aimed to maximize the reactor productivity subject to uncertainty and minimize the uncertainty-induced output variability. The results demonstrate the impact of spatially-varying parametric uncertainty on the catalytic reactor performance. They also highlight the importance of its inclusion to adequately account for phenomena such as catalyst fouling in robust optimization and process improvement studies.

The dynamic behaviour of the catalytic reactor system was similarly assessed within this work to evaluate the effects of uncertainty on the reactor performance as it evolves in time and space. For this study, uncertainty analysis was performed on a transient multiscale catalytic reactor model subject to changes in the system temperature. These results were used to formulate robust dynamic optimization studies to maximize the transient catalytic reactor behaviour. These studies aimed to determine the optimal temperature trajectories that maximize the reactor's performance under uncertainty. Dynamic optimization was also implemented to identify the optimal design and operating policies that allow the reactor, under spatially-varying uncertainty, to meet targeted performance specifications within a level of confidence. These studies illustrate the benefits of performing dynamic optimization to improve performance for multiscale process systems under uncertainty.

Acknowledgements

I would like to convey my most sincere gratitude to Dr. Luis Ricardez-Sandoval, my adviser, for his invaluable assistance in helping me complete the research for my Masters degree. His patient guidance, valuable insights, and constant support were instrumental in helping me improve my skills, overcome my fears, and reach this important milestone in my academic career. It is thanks to his encouragement that I pursued my Masters in the first place, and he is a real inspiration for me. I would also like to thank Mark Pritzker and David Simakov for reading through my thesis and for providing me with helpful suggestions.

I would also like to thank the rest of my research group, past and present, for the constant encouragement, support, and friendship. I can only hope that one day during my working career that I will be a part of a team as awesome as this one. I would like to specifically thank Grigoriy Kimaev and former group member Shabnam Rasoulian for their time and patience for helping me with my research. I would also like to thank Robert Koller, Kavitha Menon, and Ilse Cerrillo for being excellent officemates, and Huabei You for the spontaneous Pokemon Go adventures that served as well-needed breaks towards the end of my degree.

Furthermore, I would like to thank my parents, my brother, and my grandmother for their unconditional love and support throughout my entire academic career. In addition, I would like to thank Ryan Stewart, Bryce Robson, Sarah Hinnecke, Emily Boyce, Kim Smythe, Saad Naseem, and everyone else who was there for me and helped me get through one of the roughest moments of my life that occurred in the middle of my Masters. You all are an absolute blessing and I am honoured to have such amazing friends in my life. I would also like to thank Jeremy Vandenberg, Rick Lu, Aaron Van Krimpen, and all of my other friends and family who have provided me with friendship, support, and encouragement throughout my engineering degrees. Additionally, I would like to thank Lyn Chaffart and Ryan Stewart for taking the time to proofread this thesis. Your help was most invaluable to me. Finally, and most importantly, I would like to thank my Creator and Saviour, Jesus Christ, for giving me the motivation, creativity, encouragement, strength, and energy needed to get through my Masters degree.

Table of Contents

List of Figures

List of Tables

Nomenclature

$*$	singular empty site on the catalyst surface
$**$	two adjacent empty sites on the catalyst surface
A	first chemical reactant species
A^*	molecule of species A adsorbed to a single catalyst surface site
$\boldsymbol{a}_\eta$	ηth order PCE coefficients that fit $\boldsymbol{\psi}(x,y,t)$ to $\boldsymbol{\beta}_\eta$
B	second chemical reactant species
B^*	molecule of species B adsorbed to a single catalyst surface site
$\mathbf{b}_{lw}$	coefficients for the lower bound DDM
$\mathbf{b}_{up}$	coefficients for the upper bound DDM
$\mathbf{b}_{\mu}$	coefficients for the expected value DDM
$\mathbf{b}_{\sigma^2}$	coefficients for the variance DDM
C	chemical product species
$C^*_{C,out}$	targeted setpoint for the simultaneous design and on-line control study, Eq. (7-5)
$C_s(x,y,t)$	concentration of species s at (x,y,t), (mol/L)
$C_s(x,y)_{old}$	concentration of species s at (x,y) during the previous iteration of the steady-state multiscale model
$C_{s,in}$	inlet concentration of species s, (mol/L)
$C_{s,out}(t)$	outlet concentration of species s at $(x=L, y=0)$ at time t, (mol/L)
$C^{lw}_{s,out}$	lower probabilistic bound of $C_{s,out}$ subject to uncertainty, (mol/L)
$C^{up}_{s,out}$	upper probabilistic bound of $C_{s,out}$ subject to uncertainty, (mol/L)
$C^{lw}_{s,out,MC}$	lower probabilistic bound of $C_{s,out}$ determined using MC sampling, (mol/L)
$C^{up}_{s,out,MC}$	upper probabilistic bound of $C_{s,out}$ determined using MC sampling, (mol/L)
C_{site}	concentration of active sites on the catalyst surface, (sites/m^2)
D_s	diffusion coefficient of species s, (m^2/s)
$E_{d,s}$	activation energy of desorption for species s, (kJ/mol)
E_r	activation energy of reaction, (kJ/mol)
$F^{-1}\left(\Pi\middle\vert\psi_n(x,y,t)\right)$	inverse cumulative distribution function of ψ_n at (x,y,t) evaluated at a probability Π
$f_{PD,\phi_m(x,y,t)}$	probability distribution function for ϕ_m at (x,y,t)
$f_{PD,\Xi}$	probability distribution functions for $\boldsymbol{\Xi}$

$f_{PD,\psi_n(x,y,t)}$	probability distribution function for ψ_n at (x, y, t)
$He_\eta(\boldsymbol{\Xi})$	ηth-order Hermite polynomial evaluated at $\boldsymbol{\Xi}$
I	number of discretized axial points where different uncertainty distributions are applied to $\boldsymbol{\Phi}$
J	number of discretized radial points where different uncertainty distributions are applied to $\boldsymbol{\Phi}$
$\mathbf{J}(x, y, t)$	first-order (Jacobian) sensitivity matrix for ψ_n at (x, y, t); used for PSE
K	number of discretized temporal points where different uncertainty distributions are applied to $\boldsymbol{\Phi}$
$k_{a,s}$	catalyst adsorption rate constant for species s, (molecule·L/(mol·site·s))
$k_{d,s}$	catalyst desorption rate constant for species s, (molecule/(site·s))
k_r	catalyst reaction rate constant, (molecule/(site·s))
L	reactor axial length, (μm)
L_{max}	maximum (upper) reactor length bound for robust optimization, (μm)
L_{min}	minimum (lower) reactor length bound for robust optimization, (μm)
M	number of uncertain parameters $\boldsymbol{\Phi}$
$\mathbf{M}(x, y, t)$	second-order (Hessian) sensitivity matrix for ψ_n at (x, y, t); used for PSE
$M_{C,prod}(x, \rho, t)$	number of molecules of species C produced directly into the fluid phase from a kMC lattice at (x, ρ) and time t over n_τ kinetic events
N	number of system outputs $\boldsymbol{\psi}$
N_{Av}	Avogadro's number (molecules/mol)
$N_e(x, \rho, t)$	local number of empty catalyst sites for a kMC lattice at (x, ρ) and at time t
$N_r(x, \rho, t)$	local number of surface reactant ensembles on the catalyst surface on a kMC lattice at (x, ρ) and at time t
$N_s(x, \rho, t)$	local number of molecules of species s adsorbed to the catalyst surface on a kMC lattice at (x, ρ) and at time t
N_{site}	total number of catalyst sites on a kMC lattice
N_T	number of temperature changes for the dynamic optimization case studies
N_{total}	total number of catalyst sites on a kMC lattice
$\mathcal{N}_q$	number of discretized points for $\boldsymbol{\chi}_q$
$\mathcal{N}_T$	number of discretized temperature points
$\mathcal{N}_v$	number of discretized fluid velocity points
$\mathcal{N}_\rho$	number of discretized pore radius points

n_s	number of chemical species considered in the reactor system
n_{teeth}	number of teeth in the gap-tooth method
$n_\tau(x,\rho,t)$	number of kinetic events occurring at (x,ρ,t) over one cycle of the kMC model
P	number of sample points in a PDF histogram generated by MC sampling
$P(\boldsymbol{\Xi})$	joint density of $\boldsymbol{\Xi}$
Q	number of input design and operational parameters for the DDMs
R	ideal gas constant, (kJ/(mol·K))
T	system temperature, (K)
$\mathbf{T}$	vector of system temperatures at different time points, (K)
T_{max}	maximum (upper) temperature bound for optimization, (K)
T_{min}	minimum (lower) temperature bound for optimization, (K)
T_{n_T}	n_Tth value of the temperature for the DDMs, (K)
t_{final}	final simulation time for the transient multiscale model.
$t_{ov,w}$	discretized temporal points at which the reactor system output variation in $\boldsymbol{\psi}$ is assessed, (s)
t_{SS}	steady state batch time intervals for the transient reactor model
$t_{ud,k}$	discretized temporal points where different uncertainty descriptions are applied to $\boldsymbol{\Phi}$, (s)
U	number of discretized axial points where $\boldsymbol{\psi}$ is assessed
V	number of discretized radial points where $\boldsymbol{\psi}$ is assessed
W	number of discretized temporal points where $\boldsymbol{\psi}$ is assessed
$W_{a,s}(x,\rho,t)$	rate of adsorption for species s at (x,ρ) and at time t, (molecule/(site·s))
$W_{d,s}(x,\rho,t)$	rate of desorption for species s at (x,ρ) and at time t, (molecule/(site·s))
$W_r(x,\rho,t)$	rate of reaction at (x,ρ) and at time t, (molecule/(site·s))
$X_{Expansion}(L,0,t)$	a statistical parameter for $C_{C,out}$ at time t determined by PSE or PCE
$X_{MC}(L,0,t)$	a statistical parameter for $C_{C,out}$ at time t determined by MC sampling
$x_{ov,u}$	discretized points along the reactor axial length at which the system output variation in $\boldsymbol{\psi}$ is assessed, (μm)
x_{tooth}	axial location of a tooth along the catalyst surface in the gap-tooth model, (μm)
$x_{ud,i}$	discretized points along the reactor axial length where different uncertainty descriptions are applied to $\boldsymbol{\Phi}$, (μm)

$y_{ov,v}$	discretized points along the reactor radial length at which the system output variation in $\boldsymbol{\psi}$ is assessed, (nm)
$y_{ud,j}$	discretized points along the reactor radial length at which different uncertainty descriptions are applied to $\boldsymbol{\Phi}$, (nm)
$Z(C_{C,out})$	key statistical parameter of the variability in $C_{C,out}$

Greek Symbols

α	confidence level for determining probabilistic bounds
$\boldsymbol{\beta}(\boldsymbol{\Xi})$	multidimensional orthogonal polynomial function, based on $f_{PD,\boldsymbol{\Xi}}$
$\boldsymbol{\beta}_{\eta}(\boldsymbol{\Xi})$	ηth term of $\boldsymbol{\beta}(\boldsymbol{\Xi})$
Δt_{FD}	temporal step size used in the finite difference solver of the transient fluid phase model, (s)
Δt_{MST}	multiscale trade-off time, (s)
Δt_{T}	time interval between temperature changes for the dynamic optimization case studies, (s)
$\Delta \chi_q$	interval between two values of χ_{q,n_q}
$\Delta\boldsymbol{\psi}(x,y,t)$	distance between $\widehat{\boldsymbol{\psi}}$ and $\boldsymbol{\psi}$ at (x,y) and at time t
$\delta_{i,j}$	Kronecker delta
ε_{kMC}	tolerance criterion for the steady-state kMC model, (%)
ε_{MS}	tolerance criterion for the steady-state multiscale model, (%)
ζ_1	random number generated from a standard uniform distribution for selecting a kMC event
ζ_2	random number generated from a standard uniform distribution for selecting a site on the kMC lattice to execute a kMC event
ζ_3	random number generated from a standard uniform distribution for incrementing the time for kMC
η	order of the series expansions used for PSE and PCE
$\theta_e(x,\rho,t)$	local fractional coverage of empty sites at time t and at a discrete point (x,ρ) on the catalyst surface
$\theta_s(x,\rho,t)$	local fractional coverage of species *s* at time t and at a discrete point (x,ρ) on the catalyst surface
κ	unit conversion factor, (m^3/L)

λ	unit conversion constant between the microscale and macroscale models, (sites·m·mol/(L·molecule))
Λ	weight term used to formulate robust optimization problems
$\mu^*(C_{C,out})$	minimum acceptable mean value of $C_{C,out}$ in optimization problems (5-6) and (6-8)
$\mu(C_{s,out})$	mean value of $C_{s,out}$
$\mu(\phi_m(x,y,t))$	mean value of $\phi_m(x,y,t)$, used to define $f_{PD,\phi_m(x,y,t)}$
$\mu(\psi_n(x,y,t))$	mean values of ψ_n at (x,y) and at time t subject to $f_{PD,\psi_n(x,y,t)}$
v	fluid velocity from convection, (mm/s)
v_{max}	maximum (upper) fluid velocity bound for robust optimization, (mm/s)
v_{min}	minimum (lower) fluid velocity bound for robust optimization, (mm/s)
v_{n_v}	n_vth value of the fluid velocity for the DDMs, (mm/s)
$\boldsymbol{\Xi}$	matrix-block of random realizations with standard properties dependent upon $\boldsymbol{\Phi}$
$\boldsymbol{\xi}_m$	random realization m with standardized properties dependent upon $\boldsymbol{\phi}_m$ at each point $(x_{ud,i}, y_{ud,j}, t_{ud,k})$
$\xi_m(x,y,t)$	value of random realization m dependent upon ϕ_m at (x,y,t)
Π	probability at which $F^{-1}(\Pi\|\psi_n(x,y,t))$ is evaluated
ρ	reactor pore radius, (nm)
ρ_{max}	maximum (upper) reactor pore radius bound for robust optimization, (nm)
ρ_{min}	minimum (lower) reactor pore radius bound for robust optimization, (nm)
ρ_{n_ρ}	n_ρth value of the reactor pore radius for the DDMs, (nm)
$\sigma^2(C_{s,out})$	variance of $C_{s,out}$
$\sigma^2(\phi_m(x,y,t))$	variance of $\phi_m(x,y,t)$, used to define $f_{PD,\phi_m(x,y,t)}$
$\sigma^2(\psi_n(x,y,t))$	variance of ψ_n at (x,y) and at time t subject to $f_{PD,\psi_n(x,y,t)}$
$\tau_\iota(x,\rho)$	time to perform the ιth kMC event on a kMC lattice at (x,ρ), (s)
$\widehat{\boldsymbol{\Phi}}$	3D matrix of nominal values of the uncertain parameters at each point $(x_{ud,i}, y_{ud,j}, t_{ud,k})$
$\boldsymbol{\Phi}$	matrix-block of uncertain parameters at each point $(x_{ud,i}, y_{ud,j}, t_{ud,k})$
$\widehat{\boldsymbol{\phi}}_m$	matrix of nominal values of uncertain parameter m at each point $(x_{ud,i}, y_{ud,j}, t_{ud,k})$
$\boldsymbol{\phi}_m$	matrix of uncertain parameter m at each point $(x_{ud,i}, y_{ud,j}, t_{ud,k})$
$\phi_m(x,y,t)$	value of uncertain parameter m at (x,y,t)

$\mathbf{X}$	vector of input design and operational parameters for the DDMs
$\boldsymbol{\chi}_q$	values of the qth input parameter for the DDMs
χ_{q,n_q}	n_qth value of the qth input parameter for the DDMs
$\widehat{\boldsymbol{\psi}}(x,y,t)$	vector of nominal system outputs at (x,y) and at time t
$\boldsymbol{\psi}(x,y,t)$	vector of system outputs at (x,y) and at time t
$\hat{\psi}_n(x,y,t)$	value of nominal system output n at (x,y) and at time t
$\psi_n(x,y,t)$	value of system output n at (x,y) and at time t
$\psi_n^{lw/up}(x,y,t)$	lower(lw)/upper(up) probabilistic bound of ψ_n at (x,y,t)
$\omega_{s,ads}(x,\rho,t)$	rate of adsorption for species s at (x,ρ,t), (mol·m/(L·s))
$\omega_{s,cons}(x,\rho,t)$	rate of gas phase consumption for species s at (x,ρ,t), (mol·m/(L·s))
$\omega_{s,des}(x,\rho,t)$	rate of desorption for species s at (x,ρ,t), (mol·m/(L·s))
$\omega_{s,prod}(x,\rho,t)$	rate of gas phase production of species s at (x,ρ,t), (mol·m/(L·s))

Abbreviations

CFD	Computational fluid dynamics
CSTR	Continuous stirred-tank reactor
DDM	Data-driven model
DFT	Density functional theory
FD	Finite difference
FEA	Finite element analysis
kMC	Kinetic Monte Carlo
MC	Monte Carlo
MD	Molecular dynamics
MF	Mean-field
NISP	Non-intrusive spectral projection
ODE	Ordinary differential equation
PCE	Polynomial chaos expansion
PDE	Partial differential equation
PDF	Probability distribution function
PFR	Plug flow reactor
PSE	Power series expansion
SDE	Stochastic differential equation

Chapter 1
Introduction

Catalysis is a crucial process in the production of chemicals and materials, and consequently it plays a key role in a wide array of industrial applications for a number of key economic sectors such as energy production, chemical manufacturing, and environmental engineering.[1] It is predicted that catalysts are used, to some extent, in over 90% of all chemical production processes worldwide.[2] The world market for catalysts was $16.3 billion in 2013, and this figure is expected to grow at a rate of 4.8% per year, with expectations that over $20.6 billion will be invested in catalysis by 2018.[3] This rapid growth in the catalysis industry has motivated substantial research into the development of new catalyst materials and the optimization of existing catalytic reactor processes to improve the efficiency and lower the costs of catalyst-driven applications.[4,5] In particular, reactor modeling approaches have emerged as a low-cost and efficient means of performing design and optimization studies on catalytic reactors.[6]

Catalytic reactor systems are multiscale in nature and depend on a number of physical and chemical phenomena that occur on differing length and time scales. The catalytic reactor behaviour is primarily dictated by fine-scale catalyst events that evolve at a molecular level. These catalytic events are impacted by bulk process parameters such as the system temperature and reactant concentrations, and thus they can be controlled by direct manipulation of these key system parameters.[7,8] Consequently, the diverse mechanisms of catalytic reactor systems are most readily captured using multiscale modeling approaches that simulate the various reactor events on the scales in which they occur.[9–11] These multiscale models typically consist of continuum models that capture the bulk behaviour of the reactor fluid species combined with kinetic modeling approaches such as kinetic Monte Carlo (kMC) that describe the catalyst kinetic behaviour.[8] Multiscale modeling has paved the way for high-accuracy reactor models that to not require additional model-fitting parameters as is often necessitated for empirical model-based approaches. Sufficiently-designed multiscale models can therefore provide exceptionally accurate results for optimization and process improvement studies as compared to traditional modeling methods.[12] However, there still lie numerous challenges that impede the advancement of multiscale model-based optimization and design in catalytic reactor systems. These challenges include the trade-off between accuracy and efficiency, and model-plant mismatch due to uncertainty.

In order to perform efficient model-based optimization and process improvement studies on a catalytic reactor system, it is essential to develop reactor models with high accuracy and low computational cost. Although multiscale models have the capability to provide exceptional accuracy for modeling catalytic systems, they are typically computationally demanding and thus prohibitive to implement for robust optimization applications. These models typically implement molecular modeling techniques such as kMC

to accurately simulate the catalytic reactions taking place, which lack a closed form and can be computationally intensive. In addition, kMC and other Monte Carlo-based approaches are inherently stochastic, and therefore require sufficiently large simulation spaces and high computational costs in order to minimize the random fluctuations and achieve sufficient accuracy.[13] Alternatively, the catalytic behaviour can be simulated using closed-form models such as the mean-field (MF) approach to reduce the computational burden of the multiscale model. However, these approaches rely on assumptions that are not representative of practical catalytic reactor systems, and consequently their results can deviate substantially from the actual system response.[14] Consequently, there exists a trade-off between the accuracy and efficiency of the multiscale modeling approach that must be addressed in order to perform efficient optimization while maintaining sufficient model accuracy.

Although multiscale models have the capability to accurately simulate the behaviour of catalytic reactor systems, these models are restricted by model-plant mismatch and uncertainty.[10] This mismatch can stem from a number of sources, including lack of knowledge about the system phenomena, as well as uncertainties in the system parameters.[15] There are often multiple potential reaction pathways capable of describing a particular reaction, and therefore exact reaction mechanisms that take place in a catalyzed system are not often known with complete certainty.[16] Furthermore, the values of the system parameters are subject to uncertainty due to experimental and measurement errors when estimating the values of the system parameters from experimental results.[17] In addition, any kinetic phenomena not taken into account in the primary multiscale model (i.e. catalyst poisoning and fouling) can alter the catalyst kinetic behaviour and can invoke further degrees of uncertainty in the catalyst parameters.[18–20] These mechanisms can result in spatially-varying uncertainties in catalytic flow reactor systems where the catalyst is subject to concentration gradients in the reactant and product species. Failure to incorporate uncertainty and model-plant mismatch into the optimization and design of catalytic reactor systems can result in significant loss of reactor performance and can prevent the realization of desired system objectives.[21–23] Uncertainty propagation techniques can unfortunately be computationally intensive to implement in multiscale systems.[24] Consequently, uncertainty is seldom taken into account when performing optimization and process improvement studies on multiscale catalytic reactor systems.

1.1 Motivation, Objectives, and Contributions

The advent of multiscale modeling has reignited an interest in model-based design and optimization of catalytic reactor systems, since this modeling method enables the direct control of molecular-scale catalytic events through manipulation of the bulk system parameters.[7,8] However, there are still a substantial number of gaps in this field that impede on the convergence between the multiscale model-based methodologies

and real catalytic reactor systems. Model-plant mismatch and uncertainty in the parameters and reaction mechanisms are significant hindrances to the accurate performance of multiscale models, yet only a handful of studies have considered the effect of uncertainty in multiscale catalytic reactor models. Furthermore, there has been very little research into spatially-varying parametric uncertainty or its effects on the performance and optimization of multiscale catalytic flow reactor systems. As a result, the development of low-cost uncertainty propagation techniques for efficient optimization of multiscale catalytic reactor systems subject to uncertainty has been severely lacking.

Motivated by this, the overall objective of this research is to efficiently address the issue of model-plant mismatch in the design and optimization of multiscale catalytic reactor systems. In this work, low-order uncertainty propagation techniques are implemented to perform uncertainty analysis on a multiscale multiscale single-pore catalytic flow reactor model in order to assess the impact of uncertainty on the system performance. These techniques are subsequently applied to perform efficient robust and dynamic optimization studies on the catalytic reaction system. Note that the reactor system considered in this work consists of a virtual environment simulation whose reaction mechanisms are assumed to be concretely known. Consequently, it is assumed that reaction mechanism uncertainty can be neglected, and therefore uncertainty is only considered in the reactor model's kinetic and design parameters within this research. The specific objectives of this research are as follows:

- To perform uncertainty analysis on a multiscale single-pore catalytic flow reactor system with the purpose of evaluating the impact of parametric uncertainty on the catalytic reaction system. The uncertainty analysis is performed using low-order power series expansions (PSEs) and polynomial chaos expansions (PCEs) to approximate the variability in the reactor model outputs as a function of the uncertain parameters. The effects of uncertainty are studied as they propagate in space and in time through the catalytic reaction system. These measurements are used to evaluate the deviation in the expected reactor performance due to uncertainty in key system parameters.
- To assess the impact of spatially-varying uncertainty due to the exclusion of kinetic events such as catalyst poisoning and fouling on the performance of the single-pore catalytic flow reactor model. PCE is used to propagate unique uncertainty realizations in the uncertain parameters at various points in space along the length of the multiscale reactor model. The response of the catalytic reaction system to spatially-varying uncertainty is compared and contrasted to the system response under spatially-constant uncertainty descriptions.
- To implement the proposed uncertainty propagation techniques into robust optimization formulations in order to maximize the reactor performance under uncertainty. The catalytic

reactor performance is optimized by maximizing the concentration of the desired products and by minimizing the variation in the output product concentrations due to parametric uncertainty.

- To develop efficient closed-form data-driven models (DDMs) that perform rapid and accurate optimization of the catalytic reaction system subject to a large number of uncertainty realizations. These models are developed using gathered statistical data on the catalytic reactor performance subject to parametric uncertainty.
- To implement the uncertainty propagation techniques into dynamic optimization formulations on a transient multiscale single-pore catalytic reactor model that is subject to uncertainty. These dynamic optimization studies are used to determine the operation and design policies that maximize the reactor performance and minimize the impact of uncertainty on the multiscale catalytic reactor system.

In order to perform meaningful and accurate model-based optimization studies in catalytic reaction systems, it is essential to implement techniques that mitigate model-plant mismatch in the reactor model. However, the development of computationally-efficient uncertainty methods for multiscale catalytic reactors is sorely lacking. This study aims to fill this gap through the implementation of advanced uncertainty propagation techniques such as PSE and PCE, as well as practical modeling approaches such as statistical DDMs, in order to perform efficient optimization on the multiscale single-pore catalytic reactor model subject to uncertainty. This research will, therefore, contribute towards the development of efficient robust and dynamic optimization policies for catalytic reactor improvement. Additionally, the uncertainty analyses performed in this work grant insight onto the effects of parameter uncertainty on the behaviour of heterogeneous catalytic reactor systems.

1.2 Thesis Outline

The remainder of the thesis is organized into seven chapters as follows:

- Chapter 2 presents a review of the literature and discusses the relevant background information for the research presented in this work. This chapter provides an overview of catalysis with a key focus on the mechanisms of heterogeneous catalytic reactor systems. This chapter additionally discusses the application of multiscale modeling to catalytic reactor systems and the challenges associated with this method. The end of this chapter subsequently provides an overview of model-plant mismatch, its impact on multiscale catalytic reactor systems, and the uncertainty propagation methodologies that can be used to accommodate for parametric uncertainty.

- Chapter 3 introduces the multiscale single-pore catalytic flow reactor system considered in this work and the multiscale modeling approaches that were used to capture the reactor performance. The modeling approaches detailing the continuum flow of the chemical species through the reactor and the kinetic catalyst surface events are described. Techniques are also discussed for coupling the different models and for minimizing the impact of random noise when a stochastic model is used in the multiscale formulation.
- Chapter 4 provides an overview of the low-order series expansions (PSE and PCE) that can be used to approximate the effects of parametric uncertainty on the multiscale single-pore catalytic reactor performance. The accuracy of these uncertainty propagation models is verified via comparison to the traditional Monte Carlo sampling method. In addition, this chapter provides a brief comparison between the accuracy and efficiency of these two methods.
- Chapter 5 performs uncertainty analysis on the steady-state multiscale catalytic reactor model in order to evaluate the effects of parametric uncertainty in numerous key system parameters on the single-pore catalytic flow reactor system. PSE is used to propagate parametric uncertainty through the multiscale model and assess its impact at various spatial locations along the catalytic reactor length. The PSE-based propagation framework is subsequently used to perform robust optimization on the catalytic reaction system. This work has been previously published in the *AIChE Journal*.[25]
- Chapter 6 investigates the impact of spatially-varying parametric uncertainty on the behaviour of the steady-state multiscale catalytic reactor system. Catalytic deactivation due to poisoning and fouling (i.e. mechanisms that were not included in the multiscale model) is considered to be the source of the spatially-varying uncertainty descriptions. PCE is used to compare the effects of spatially-constant and spatially-varying uncertainty descriptions on the multiscale reactor performance. Subsequently, closed-form DDMs are developed to approximate key statistics of the catalytic reactor performance subject to the spatially-constant and spatially-varying uncertainty descriptions. These DDMs are used to perform efficient robust optimization on the uncertain multiscale single-pore catalytic reactor system. This work has been accepted for publication by the *Canadian Journal of Chemical Engineering.*[26]
- Chapter 7 investigates the effects of parametric uncertainty on the dynamic behaviour of a transient multiscale single-pore catalytic reactor system. PSE is used to propagate uncertainty through the reactor model and to evaluate its effects on the reactor performance as it propagates in time. The effects of uncertainty are also investigated on the behaviour of a multiscale catalytic reactor system subject to transient changes in the system temperature. This work was previously published in the 11th IFAC Symposium on Dynamics and Control of Process Systems including

Biosystems (DYCOPS).[27] This study was further expanded through application to dynamic optimization studies that seek to determine the optimal design and operational conditions of the multiscale catalytic reactor model subject to spatially-varying uncertainty. PCE is used in these studies to propagate the uncertainty in order to determine the optimal temperature profile and the optimal design and operating policies that maximize the productivity of the catalytic reaction system. This work has been accepted for publication by the *Journal of Process Control*.[28]

- Chapter 8 presents the conclusions of this study and provides recommendations for future research.

Chapter 2
Background and Literature Review

The importance of heterogeneous catalytic reactors in chemical processes has inspired a significant amount of research directed towards identifying new catalysts and optimizing existing catalytic processes.[5,29,30] The behaviour of a heterogeneous catalytic reactor system depends on fine-scale (molecular) events that occur along the catalyst surface, which are in turn strongly influenced by the bulk reactor behaviour. Accordingly, the catalytic reaction process can be enhanced if control of the fine-scale events can be performed through direct manipulation of the system's process parameters.[7,8]

This behaviour is most prominently explored through the use of model-based approaches, which enables easy implementation of optimization and process improvement techniques.[6,31] To accurately capture the full behaviour of a catalytic reaction process, these models must encompass the wide range of physical and chemical phenomena that evolve over differing length and time scales, and as a result, multiscale modelling has emerged as a prominent approach for modeling catalytic reactor systems.[9,10] However, the multiscale modeling approach still presents a number of challenges that need to be addressed. In addition to the large computational costs, multiscale systems are particularly susceptible to uncertainty and model-plant mismatch, which can significantly hinder the performance of the system.[11,15] Neglecting model-plant mismatch in model-based optimization and control schemes can cause substantial deviations from the predicted reactor behaviour, which can lead to considerable losses in reactor efficiency.[21–23] Therefore, parametric uncertainty must be taken into account in order to accurately achieve process improvement.

The objective of this chapter is two-fold: To provide relevant background knowledge, and to present a review of the literature on catalytic reactor systems, multiscale modeling, and model-plant mismatch. To that end, Section 2.1 presents a brief overview on catalysis, with particular focus on heterogeneous catalysts and their applications in chemical reactor systems. Subsequently, Section 2.2 details the multiscale modeling approach and its uses in the literature with specific applications to heterogeneous catalysis. This section additionally discusses the challenges associated with multiscale modeling and the techniques that can be used to overcome them. Section 2.3 then provides an overview of model-plant mismatch and parametric uncertainty, their effects on multiscale modeling approaches, and the various methods of uncertainty propagation. The catalytic reactor system considered in this work consists of a heterogeneous solid-fluid catalyst consisting of a single pore in a continuous flow reactor system; thus this chapter will primarily focus on these types of catalytic reactor systems due to their relevance to this work.

2.1 Catalysis and Catalytic Reactor Optimization

Catalysts are materials that accelerate the rate of a chemical reaction through the provision of energetically-favourable reaction pathways. Catalysts are not consumed during the reaction process, and consequently a small amount of catalyst can be utilized to catalyze many reactions over long periods of time. As a result, catalysts are extremely important to the efficient manufacture of chemical products in a variety of industrial applications.[1,2] It is important to note that catalysts do not affect the thermodynamics of a reaction; rather they affect the kinetics of both the forward and the reverse reactions taking place, and as such, a catalyst will only affect the speed of the reactions and not the species concentrations at equilibrium.

Catalyst materials can be sub-divided into homogeneous and heterogeneous catalysts depending on the phase of the catalyst relative to the reactants. In homogeneous catalysis, the catalyst is dispersed within the same phase as the reactant species. Homogeneous catalysts typically consist of transition metal complexes that bind to the reactant materials and weaken their chemical bonds to promote kinetically-unfavourable reactions and to stabilize the reaction intermediates.[32] They have high selectivity and are easy to modify to catalyze specific reactions. However, due to the homogeneous nature of the system, it can be difficult to separate the catalyst from the products, limiting the use of homogeneous catalysts in continuous reaction systems.[33] In heterogeneous catalysis, on the other hand, the catalyst is in a different phase than the reactants. Heterogeneous catalyst systems typically consist of solid catalysts interacting with liquid or gaseous reactant species. These catalysts provide a solid surface on which reactants can adsorb and interact with other reactant species. Solid heterogeneous catalysts additionally have a large number of low energy surface electronic states, which enable lower activation energies of reaction than would be observed in an un-catalyzed fluid-phase reaction.[2,34] Heterogeneous catalysts have high catalytic activity and can be readily separated from the reactants and products. In addition, heterogeneous catalysts can be readily incorporated into a number of key chemical reactor systems, including batch reactors, continuous stirred-tank reactors (CSTRs), plug flow reactors (PFRs), and fluidized beds.[1] Heterogeneous catalytic reactors, however, typically require high system temperatures and reactant concentrations, and most heterogeneous catalysts have low selectivity. To help overcome this, the selectivity of a heterogeneous catalyst can be improved through the use of zeolites and other catalytic materials with adjustable pore sizes.[2,35]

One of the key challenges in catalytic systems is that the catalysts are susceptible to deactivation through a variety of different mechanisms.[18,19] Heterogeneous catalysts can be deactivated by fouling, which details the physisorption of unwanted chemical species to the catalyst surface, effectively blocking the catalyst sites from interacting with the reactant species. A key example of catalytic deactivation due to fouling is catalyst coking, which details the deposition of coke and other carbon-based compounds on the catalyst

surface. Coke deposits on the catalyst surface can grow due to multilayer physisorption of carbon and coke, which can restrict or block the flow of reactants through porous catalysts. Catalysts can similarly be deactivated through poisoning mechanisms, which detail the strong chemisorption of undesired chemical species on the catalyst surface. These adsorbates can physically block a number of catalyst sites, preventing them from adsorbing or interacting with any further reactant species. In addition, strongly-adsorbed poisons can alter the electronic properties and the geometric structure activity of a catalyst, resulting in changes in the kinetic and structural catalyst parameters.[36] Catalyst deactivation is also possible due to thermal or mechanical degradation of the catalyst, which are a result of the extreme reactor conditions. These effects include the loss of catalyst surface area at high temperatures (sintering) and the physical erosion of the catalyst materials due to high pressures. Catalyst deactivation presents a significant hurdle in catalytic reactor engineering as it adversely affects the catalyst performance and alters the values of the catalytic parameters.[18–20] As a result, there is substantial interest both in developing techniques to prevent catalyst deactivation and to regenerate the catalyst once it becomes suitably deactivated. The ability to regenerate a catalyst depends on the deactivation mechanisms, as not all catalysts can be re-activated. Coke formations can be readily removed via gasification techniques.[37] In addition, some poisoned and fouled catalysts can be regenerated by heating, oxidation, and washing processes.[38] However, many deactivated catalyst systems cannot be regenerated without resulting in further damage to the catalyst. As a result, it would be more desirable to modify the design and operating conditions of the catalytic reactor system in order to impede catalyst deactivation, and thus, prolong the catalyst life.[39,40]

In the chemical manufacturing industry, it is highly desirable to optimize the performance of catalytic systems so as to increase the yield of the desired products while minimizing the reaction costs. This can be achieved by adjusting the process and design parameters of a catalytic reaction system in order to maximize the desired catalyst behaviour.[4,6] In heterogeneous catalysis it is essential to maximize the surface area of the catalyst in order to increase the number of interactions between the reactants and the catalyst. This can be achieved by fabricating highly-porous catalyst materials with high surface area. Ideal solid catalysts can also be achieved by affixing high surface area catalyst nanoparticles to the surface of a highly-porous support material. Within these highly-porous catalytic reactor systems, the pore size also has a significant effect on the reactor performance. Reducing the pore radius increases the surface-to-volume ratio in the catalytic reactor, which results in an improvement in catalyst performance. In addition, pores with smaller radii require lower diffusion times in order for reactants to reach active catalyst sites. In contrast, longer reactor pores increase the internal catalyst surface area, resulting in a larger number of catalyst surface sites.[2] The catalyst performance can also be increased by the addition of chemical promoters, such as alkali or alkaline earth metals, that can enhance the activity or the selectivity of the catalyst material.[41,42] The catalytic reactor behaviour may also be controlled by manipulating the reactor operating parameters such

as the system temperature, fluid velocity, and the concentration of the reactants. The system temperature directly affects the kinetics of the catalytic reaction wherein changing the system temperature impacts the amount of adsorption, desorption, and reaction that occur on the surface of a heterogeneous catalyst. Similarly, the initial concentrations of reactants also directly affect the catalyst kinetics, promoting higher rates of adsorption and reaction. The system temperature and initial reactant concentrations additionally affects other processes in the reactor system, such as the transport phenomena and the thermodynamics of the reaction. Conversely, the fluid velocity controls the amount of time that the reactants remain within the reactor system in a PFR and other flow-type reactors. Slower fluid velocities increase the probability that a reactant molecule will diffuse to the catalyst surface and result in increased residence times. By adjusting these parameters, it is therefore possible to control the reactor behaviour and optimize its performance.[1,4]

2.2 Multiscale Modeling of Catalytic Reactor Systems

Catalytic flow reactors are crucial to a number of industrial-scale chemical production processes, and the widespread integration of these reactor systems has promoted significant interest in optimal design and operation methodologies to boost reactor productivity and minimize production costs.[43,44] This can be accomplished experimentally by testing various operating conditions to determine which methods are the most optimal.[45,46] However, these approaches can require substantial amounts of time, materials, and financing in order to determine the optimum design and operating conditions. Alternatively, model-based approaches can be used to optimize the catalytic reactor behaviour at significantly reduced costs.[6]

The behaviour of catalytic reactor systems is complex and involves a number of phenomena that evolve on differing length and timescales. These phenomena can be partitioned into two different domains: A macroscopic domain, which accounts for the transport of momentum, mass, and energy through the reactor system; and a microscopic domain, which details the kinetic interactions between the individual chemical species and the catalyst surface.[8] Note that although these domains capture the microscopic and atomistic behaviour of the catalytic reactor system respectively, they are standardly referenced in multiscale modeling approaches as the macroscopic and microscopic domains. Consequently, this terminology will be used throughout the remainder of this thesis.

Catalytic reactor systems are typically modeled using continuum-based approaches that can be solved through techniques such as finite difference and finite element analysis.[47–49] These models typically assume surface uniformity, and therefore the state of the catalyst surface can be determined through simple mathematical expressions. They are thus incapable of accounting for catalyst heterogeneities such as surface defects and lateral interactions between adsorbates, and therefore do not provide an adequate description of the microscopic behaviour of a catalytic reactor system. Alternatively, the disparate scales

of the catalytic reactor system can be captured using multiscale integration hybrid algorithms that can capture each of the reactor events on the spatial and temporal scales in which they occur. These multiscale modeling algorithms typically consist of kinetic modeling approaches such as kMC or MF to capture the catalyst surface behaviour, coupled with continuum modeling approaches to describe the macroscopic behaviour of the reactor system. The aim of this section is to provide a description of the multiscale modeling approach and the challenges associated with it, with a particular focus on modeling catalytic reactor systems.

2.2.1 Multiscale Modeling Approaches

Most chemical processes involve numerous phenomena that evolve over various spatial and temporal scales. These events generally cannot be adequately captured using a single modeling approach and require unique models to simulate the relevant phenomena on the scales in which they occur. Developing an empirical single-scale model to approximate the behaviour of these processes involves making numerous assumptions and simplifications, and typically require model fitting parameters to adequately simulate the experimental results.[12] Alternatively, these systems can be modeled using multiscale integration hybrid approaches, which connect and combine different modeling approaches in order to simulate all of the relevant system phenomena on the appropriate scales. These multiscale methods are capable of achieving high accuracy by simulating each of the system events on the relevant scales in which they occur, and consequently, they are a significant improvement over singular model-based approaches.[9,10] Multiscale models allow for intercommunication between each of the modeling methods, which enables optimization and control of the microscale processes through manipulation of the macroscopic variables.[8] They additionally facilitate the implementation of top-down optimization approaches, where the system design and materials are determined in order to satisfy pre-specified optimization targets.[12,17,31] As a result, multiscale modeling has been instrumental for a number of key chemical processes such as polymer chain growth,[50,51] thin film deposition,[52,53] batch crystallization,[54,55] and catalytic reaction mechanisms.[14,56,57]

The multiscale modeling approach combines numerous modeling approaches in order to simulate phenomena occurring over a wide range of length and timescales that span from the electronic scale to the macroscopic scale,[9,10] as illustrated in Figure 2-1. On the lower end of the spectrum, the electronic scale details the electronic interactions between atoms and can be used to estimate electronic system properties such as the entropy and activation energy in a catalytic reaction system. These methods are typically modelled using quantum simulations such as Density Functional Theory (DFT) and *ab initio* calculations. The microscale (molecular) level describes the behaviour and interaction of individual atoms and molecules, and it can be modeled using atomistic-based approaches such as Molecular Dynamics (MD) and

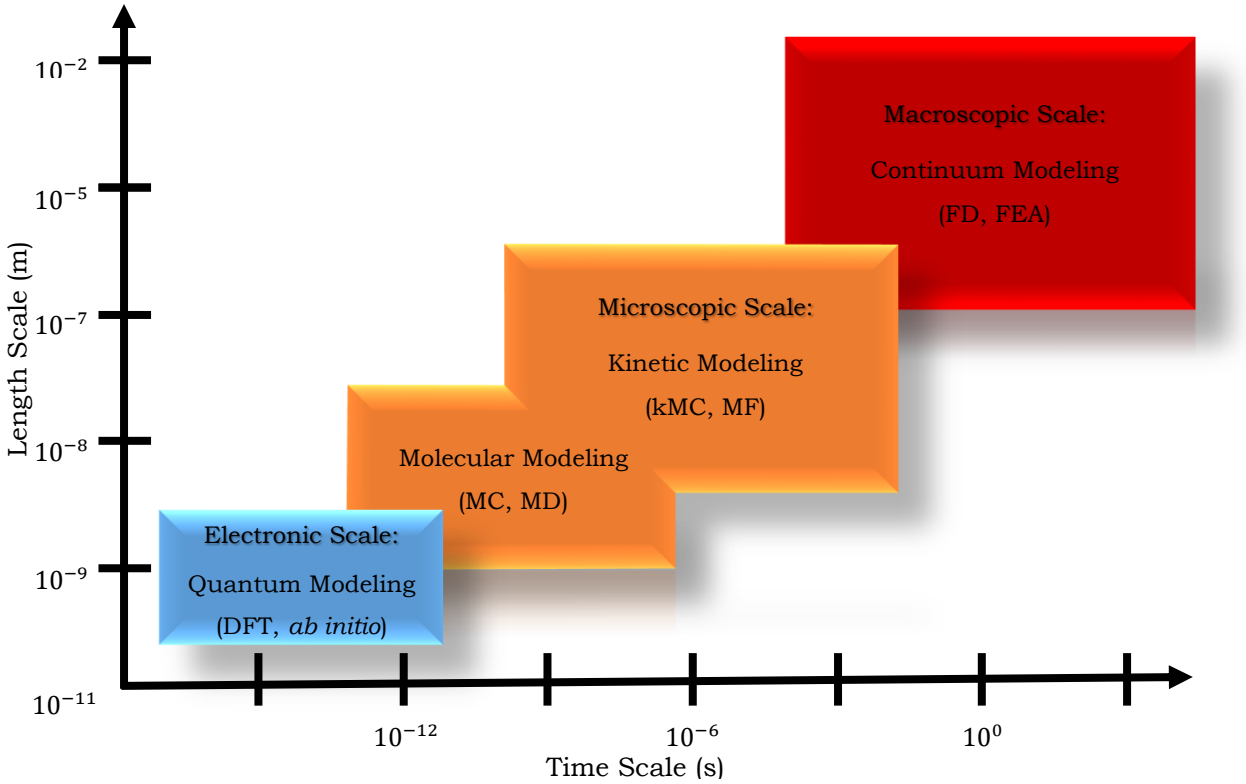

Figure 2-1. Diagram of the modeling techniques relevant to the multiscale modeling approach and their representative length and timescales.[10]

Monte Carlo (MC). In catalytic reaction processes, microscale simulations can be used to determine the kinetic interactions between the catalyst surface, the reactant molecules, and the product molecules. These processes can be modeled using kinetic approaches such as MF and lattice-based kMC. On the upper end of the length and time scales, the macroscale level details the bulk properties such as the mass, momentum, and heat transport within a catalytic reactor. This scale is traditionally modeled using continuum equations and computational fluid dynamics (CFD) approaches.

Although multiscale modeling is capable of coupling phenomena that evolve on each of these differing scales, the interaction between multiple scales can be computationally intensive. Consequently most multiscale modeling approaches consider the interactions between two different models.[10] The disparate scales of a catalytic reaction system are most readily captured using a bi-model multiscale algorithm, which couples continuum transport modeling that simulate the macroscopic fluid phase behaviour with kinetic modeling approaches such as MF or kMC that simulate the microscopic catalyst surface behaviour.[8,14] Each of these modeling methods will be subsequently detailed in the following subsections.

2.2.1.1 Macroscale Continuum Modeling

The macroscopic behaviour of a chemical system is dependent on the positions and interactions of the individual molecules that compose the system. Each of these molecules have their own energy, momentum, and other properties that dictate their individual behaviour in addition to the properties of the overall system. Subsequently, atomistic modeling approaches such as MC and MD can be implemented in order to determine the properties of each molecule in the system. This will ascertain the macroscopic system properties such as temperature and species concentrations at every point in the system. These approaches are computationally-intensive, however, which limits their applications to large-scale systems.[58]

Alternatively, sufficiently-large macroscopic systems can be treated by applying the continuum principle, such that the desired macroscopic properties can be determined at low computational costs using continuum modeling methods. The continuum hypothesis treats the bulk system as continuous, despite it being discontinuous on the molecular level. Macroscopic properties such as temperature, pressure, bulk velocity, and viscosity are assumed to vary continuously throughout the system. Consequently, these properties can be determined at any point in space and time using mathematical functions derived from classical physical laws such as Newton's laws of motion, thermodynamics, and Maxwell's equations.[59]

In catalytic reactor systems, desirable continuum properties such as temperature, bulk velocity, and bulk species concentrations can be captured using energy, momentum, and mass conservation laws that express the property variation in time and in space using partial differential equations (PDEs). These PDEs can be solved using CFD approaches such as finite differences (FD) or finite element analysis (FEA).[60,61] These continuum modeling approaches are well-established such that a number of software packages can be used to implement these techniques for modeling in a variety of systems. In this work, the macroscopic system behaviour of the catalytic flow reactor is modeled using conservation laws. These PDEs were solved using intrinsic FD approaches to approximate the bulk properties at discrete points in space and time.

2.2.1.2 Microscale Kinetic Modeling

The microscopic behaviour of a system depends on a number of fine-scale events that evolve on a molecular level. In a heterogeneous catalytic reactor system, these events detail the kinetic interaction between the reactants, products, and the catalyst surface. Depending on the reaction mechanisms taking place, these events can include the adsorption of the fluid species onto the catalyst surface, the desorption of adsorbates back into the fluid phase, the diffusion of adsorbates across the catalyst surface, and the reaction of adsorbed and/or fluid-phase species on the catalyst surface. The microscopic behaviour of the catalyst surface domain can be modeled using any number of kinetic solvers such as MF and lattice-based

kMC,[8,14] in addition to molecular-level solvers such as configurational-bias MC and MD.[62,63] This section will primarily focus on the MF and kMC kinetic modeling approaches due to their relevance to this work.

The MF approximation is a closed-form kinetic modeling approach that assumes uniform distribution of the molecules that are adsorbed onto the catalyst surface. The adsorbates are allowed to freely move along the catalyst surface using an infinite diffusion assumption, and each of the adsorbates are assumed to share the same types of neighbours.[64] Consequently, the coverage of each adsorbate species on the catalyst surface can be approximated using a series of kinetic ordinary differential equations (ODEs) in transient systems, or a series of algebraic expressions in steady-state systems. These coverage expressions can be solved using traditional ODE solvers and root finding methods. Therefore, the MF approach is computationally efficient and can be readily implemented into multiscale modeling applications. However, due to the infinite diffusion assumption, the MF approach is incapable of incorporating the lateral adsorbate interactions that are crucial for many catalytic reaction mechanisms into the kinetic model.[14,65,66]

On the other hand, kMC simulations apply MC sampling techniques in order to randomly select and execute kinetic events in a microscopic system. Given a system in a particular state, the kMC approach evaluates all of the states that are currently accessible and transitions the system into a new state at random based on the state transition probabilities. As a result, kMC can be seen as a stochastic realization of the chemical master equation, which determines the probability that a system is in a certain state at any point in space and time.[67] The transition probabilities of the kMC approach are determined by the chemical kinetics and reaction rates that govern the interaction between the relevant molecules in a system. Consequently, kMC is not focused on determining the exact position and momentum of each atom, but rather on evaluating the dynamic evolution of a microscale system.[68] The end result is a snapshot of the possible configuration of molecules in a system and their potential kinetic interactions with each other.

The kMC algorithm can be expressed as follows. The kinetic rates are determined for all possible microscopic events, such as adsorption, desorption, and reaction. An event is randomly selected based on their kinetic rates and executed within the system. The system time is subsequently incremented by a random interval generated from an exponential distribution, and the kinetic rates are updated based on the new system configuration. This cycle repeats until either the final integration time has been met in transient models or the system has reached steady state in static models.[53,68] Further details concerning the kMC algorithm implemented in this work can be found in Chapter 3.

Lattice-based kMC is a specific sub-set of kMC that is useful for describing the microscopic evolution of a surface. In a heterogeneous catalytic reactor system, lattice-based kMC implements a 2D lattice in order to approximate the positions and interactions of adsorbates on the catalyst surface. In this approach, the catalyst surface is denoted using a finite-sized lattice that updates to reflect the identity, positions, and

interactions of adsorbates on the surface. Changes made to the system are reflected by updates in the lattice, and important microscopic properties such as the surface coverages can be determined from the lattice information. The algorithm for lattice-based kMC is the same as that of general kMC, except that the system is restricted to the 2D surface lattice and the configuration of adsorbates within the lattice.

The kMC approach is a stochastic process that requires careful assembly to reduce random fluctuations in the response variables, and as a result, its computational costs are higher than those required for the MF approximation. In addition, a complete description of the system kinetics is often unknown, and therefore assumptions must be made regarding the microscopic events that can take place.[68] Despite these flaws, however, kMC is capable of providing excellent approximations of the true state of a microscopic kinetic system. In catalytic reactor systems, kMC is able to directly account for lateral interactions and other spatially-dependent interactions on the catalyst surface, and therefore it is able to accurately predict the catalyst surface behaviour.[66,69,70] As a result, kMC has emerged as an excellent tool for modeling the microkinetic behaviour of the catalyst surface.

2.2.2 Challenges in Multiscale Modeling

The multiscale modeling approach is capable of providing high-fidelity system models by combining and interconnecting different modeling techniques in order to capture the relevant system phenomena on the scales in which they evolve. However, multiscale modeling techniques still present a number of different challenges that need to be addressed. The objective of this section is to present some of the issues encountered in multiscale modeling as well as techniques that have been used in the literature to overcome these shortcomings.

The accuracy of multiscale models is generally proportional to their computational cost and subsequently a trade-off must be made in order to achieve low-cost results with sufficient accuracy. In general, the accuracy-efficiency trade-off is a practical challenge associated with most computational modeling processes, as frequently the methods that produce higher model accuracy require larger computational costs.[12] The computational burdens in multiscale modeling approaches are typically associated with the fine-scale phenomena. These events typically cannot be adequately described using closed-form models, and therefore require the use of more intensive modeling approaches such as kMC. Although closed-form models can be developed to supplement for kMC in microscopic systems, these models typically cannot achieve suitable accuracy due to the assumptions that must be made. For example, as discussed previously, the catalyst surface behaviour in a heterogeneous catalytic reactor system can be approximated using the closed-form MF approach, which cannot explicitly take into account the lateral interactions that are relevant for most catalytic reactions.[14] In order to derive accurate yet efficient

multiscale models for a heterogeneous catalytic reaction, it is necessary to assess the impact of lateral interactions and spatial heterogeneities on the reaction mechanism to determine whether MF would provide sufficient accuracy or if kMC should be implemented.

The kMC modeling approach itself can be computationally demanding since only one kinetic event is executed at a time and a large number of events are required in order to reach the kMC end conditions.[71] This has motivated efforts to derive new, computationally-efficient kMC algorithms that seek to reduce the model complexity without significant decrease in the model accuracy.[72,73] For example, the computational time can be reduced without significant loss of accuracy by decoupling the predominant kinetic events in the kMC simulations and treating them deterministically.[74,75] This approach is most practical for fast kinetic events, e.g. surface diffusion, which may consume the majority of the kMC computational time. Coarse-graining techniques can additionally be applied to further reduce the model complexity. In the spatial coarse-graining technique, the kMC lattice is subdivided into coarse cells, each consisting of an equal number of individual lattice sites, or 'microcells'. Each of these coarse cells is subsequently treated as an individual 'site' for the adsorption, desorption, and reaction of coarse-grained packets of similar molecules, called 'mesoparticles'. Thus, improved computational speeds are achieved by considering the actions and interactions of multiple molecules within the mesoparticles on the coarse cells instead of the actions and interactions of individual molecules.[76,77] Similarly, temporal coarse-graining techniques such as the τ-leap algorithm can be used to simulate multiple kMC events simultaneously over a coarse time interval, τ.[67,78] This algorithm must be confined by a leap condition that requires τ to be suitably small, such that the system experiences only slight change over that time interval.[79] Similar techniques, such as the coarse time-stepper methodologies, can also be used to coarsely evaluate the reactor dynamics. This is of particular use in multiscale systems where there exists no closed-form models to express the macroscopic system behaviour, as it allows for the construction of 'equation-free' systems that rely only on the performance of microscale models.[72,80,81]

Further complications arise in multiscale models that incorporate stochastic modeling techniques to solve a particular system domain. When coupling the kMC model with macroscopic system models, they become subject to random fluctuations that can cause instabilities. In a lattice-based kMC model, larger lattice sizes can be implemented in order to minimize the stochastic noise and improve accuracy in the responses. However, employing large lattices is computationally intensive due to the large number of events required to meet the kMC end conditions, thus making it inefficient for optimization applications. In order to circumvent this issue, smaller kMC lattices can be implemented with periodic boundary conditions to determine the evolution of the surface behaviour.[82] The stochastic noise can be further reduced by running multiple independent kMC simulations using the smaller lattices and taking the average of the results.[13,83] These independent kMC simulations can be run in parallel using parallel computation techniques such as

the decomposition-assignment-orchestration parallel computation program.[84] Alternatively, filtering techniques can be applied to filter the outputs of a reduced-order kMC lattice and eliminate the stochastic noise. In previous works, second-order linear filters have been applied to handle the stochastic fluctuations of kMC models for application in thin film growth[85] and catalytic reactor systems.[14] Filtering approaches can also be used to eliminate numerical instability when coupling kMC and continuum modeling approaches that arise due to temporal mismatch between the modeling methods.[86,87] Similarly, feedforward-feedback controllers implemented with gain-scheduled filters can be used to bound the stochastic kMC noise in noisy kMC systems.[88]

Multiscale models experience additional challenges in spatially-heterogeneous systems, where the coarse-scale inputs to the fine-scale models vary with position. For instance, in catalytic flow reactor systems such as the single-pore catalytic reactor studied in this work, the transport of the chemical species coupled with the reactions on the catalyst surface produce concentration gradients that cannot be neglected. These gradients lead to variation in the rates of microscopic surface events, which depend on the local fluid concentrations at the catalyst surface. In these spatially-varying systems, special attention must be paid that the appropriate gradients are reflected in the kMC lattice,[14] and oftentimes the microscopic system behaviour cannot be modeled using a single kMC model.[10,89] Consequently, multiple kMC lattices must be used to handle variation in the microscopic surface events over the full macroscopic spatial domain.[90] This can be accomplished efficiently through the adoption of patch dynamics techniques such as the gap-tooth model, where the spatial domain of the macroscopic model is evaluated coarsely using a minimal number of kMC lattices.[14,57] In the gap-tooth method, the entire spatial domain of the macroscopic model is subdivided into periodically-spaced patches (teeth), separated by spaces (gaps).[91–95] Figure 2-2 provides a graphical overview of how the gap-tooth method can be implemented for a kMC-continuum multiscale system. Each tooth is simulated with an independent kMC lattice that is employed to determine the specific microscopic behaviour at its location within the system. The teeth are considered to be infinitesimal, such that the effects of the macroscopic gradients on a single tooth can be assumed to be negligible. On the other hand, the gaps are treated coarsely, and the microscopic system behaviour across each gap is approximated using interpolation. More details about the gap-tooth method are presented in Chapter 3.

2.3 Parametric Uncertainty in Multiscale Catalytic Reactors

Model-based optimization and process improvement studies are limited by the accuracy of the system model. As a result, multiscale modeling approaches are ideal for simulating catalytic reactor systems for robust optimization applications due to the high accuracy achieved by modeling each of the relevant phenomena on the scales in which they occur. Like any other modeling approach, however, multiscale

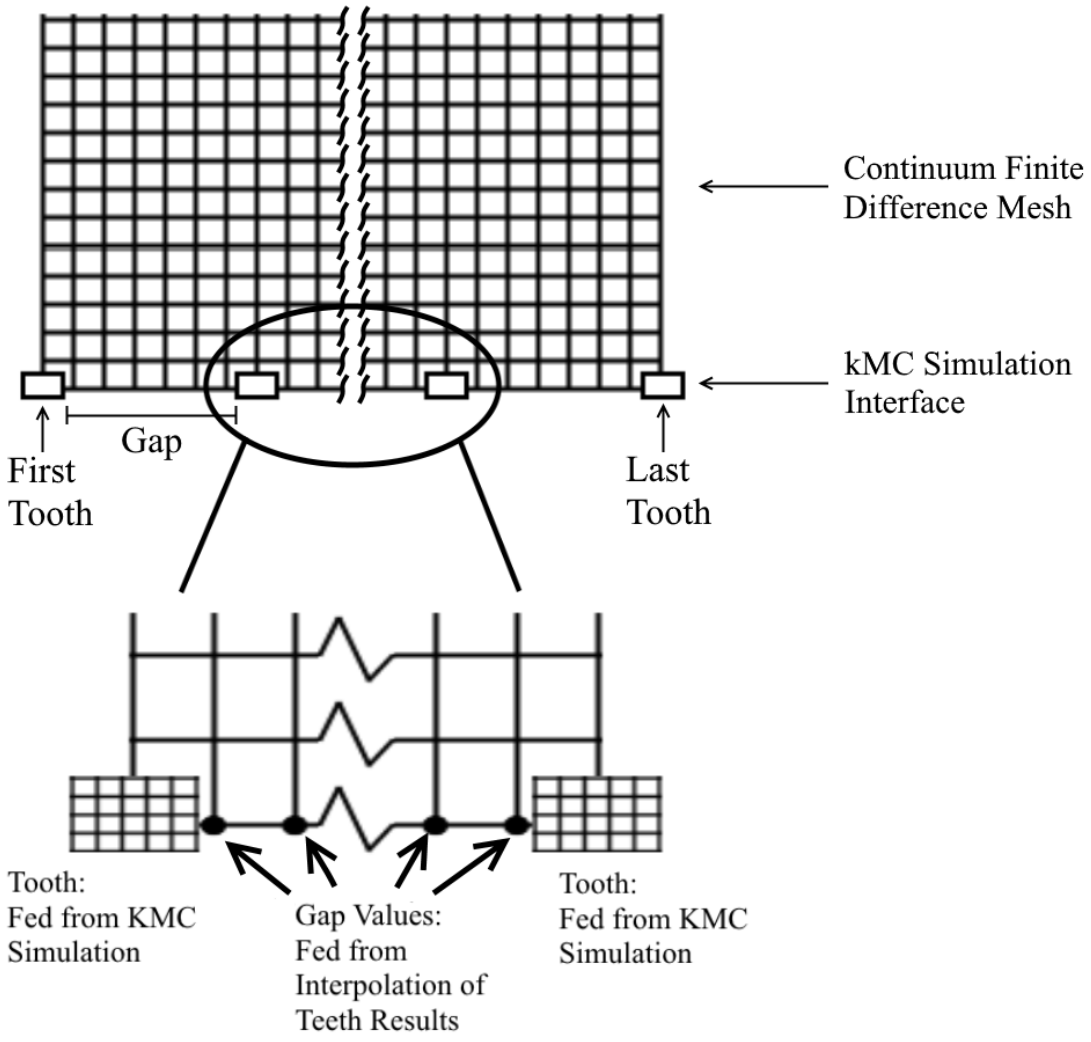

Figure 2-2. The gap-tooth scheme for a kMC-continuum multiscale system.

models are susceptible to uncertainty and model-plant mismatch, which can significantly hinder their ability to capture the system performance.[11,15] Failure to adequately account for uncertainty can result in substantial increases in the productivity costs as well as significant reactor performance losses.[21–23,96] In addition, the optimal operating conditions for many reactor systems are often close to the reactor's safety limits, and failure to incorporate model-plant mismatch can risk the unnecessary danger of exceeding the reactor safety thresholds.[97] Consequently, it is a necessity to factor in the uncertainty impact on the catalytic reactor performance when performing robust optimization or control. The objective of this section is to provide an overview of the potential sources for model-plant mismatch, and to discuss the various methods that can account for uncertainty in multiscale system models.

2.3.1 Sources of Model-Plant Mismatch in Catalytic Reactor Systems

The performance of a multiscale catalytic reactor model is significantly hindered by model-plant mismatch stemming from uncertainty in both the model structure and the system parameters. The reaction pathways that occur in the reactor are seldom completely known, with potentially undiscovered intermediate steps not taken into consideration. Multiple microkinetic pathways are often proposed that are capable of describing a particular reaction mechanism,[16] and therefore the exact pathway is often unknown. Consequently, many catalytic reactor models are subject to model structure and reaction mechanism uncertainties that inhibit them from accurately predicting the behaviour of the actual reaction system.

One of the most common and significant sources of model-plant mismatch in multiscale catalytic reactor processes stems from uncertainty in the system parameters.[10,12] True values for most design and kinetic parameters cannot be precisely measured or predicted from experimental data as they are limited by measurement and experimental errors.[98] In addition, large kinetic models often contain a sizeable number of kinetic parameters that cannot be accurately determined from gathered experimental data. This has motivated the development of novel methods to assess which kinetic parameters can be estimated from collected experimental results.[99] Alternative approaches such as DFT and other quantum simulations can be used to improve the estimates of the parameter values;[100,101] however, these approaches are limited by high computational costs and truncation errors.[12,102]

Parametric uncertainty is also present in catalytic reactor systems due to kinetic events not taken into consideration, such as catalyst deactivation. Specifically, catalyst poisoning and fouling mechanisms have been documented to alter the catalyst properties.[18,19] As a result, the catalyst kinetics cannot be known with certainty unless additional tests are performed to assess the how various degrees of catalytic deactivation affect the behaviour of the catalyst. Catalyst coking is known to affect the radius of porous catalyst materials,[103,104] whereas catalyst poisoning has been shown to affect several key catalyst parameters, including the number of available catalyst sites,[18,19,103] the activation energies,[18,19,105,106] and the kinetic rate constants.[19,106,107] Further complications arise in catalytic flow reactors in which the chemical species concentrations vary spatially, promoting non-uniform catalyst poisoning and fouling across the spatial domain.[20,108,109] The parametric uncertainty applied to these systems cannot be assumed spatially-constant, and therefore reactor studies would require multiple independent uncertainty distributions to describe the spatial variance in the uncertainty.

2.3.2 Uncertainty Propagation Techniques for Multiscale Systems

Model-plant mismatch can cause substantial deviations from the predicted performance of a multiscale-based catalytic reactor, which can lead to considerable losses in reactor efficiency.[21–23,96] It is therefore necessary to develop tools that can efficiently account for uncertainty in multiscale system models. One approach to improve the performance of batch processes in the presence of model-plant mismatch is run-to-run control, where data from previous batches is used to update the parameters and reduce the uncertainty.[54,110] This approach, however, requires previous model simulations and data from actual process runs, which is not always available or desirable.

Alternatively, uncertainty can be directly transmitted through multiscale systems using uncertainty propagation techniques. There are a number of different methodologies that can be used to propagate parametric uncertainty, and therefore the selection of an appropriate uncertainty propagation method for a particular application must be performed by assessing the trade-off between the accuracy and the efficiency of the technique. Typically, the uncertainty propagation techniques with higher accuracy require significantly increased computational costs, and consequently it is critical to select a suitable approach that can produce models with suitable accuracy for the analysis.[12] In each of the uncertainty propagation approaches, the probability distribution function (PDF) of the uncertain parameters is determined and subsequently propagated through the multiscale model in order to determine the variability in the system outputs due to uncertainty. The PDFs for the uncertain parameters can be determined using data from experimental results or DFT simulations,[111–113] however if no data is available, the uncertain parameter descriptions can be alternatively approximated by making assumptions about the uncertainty distribution. A multivariate normal PDF is often regarded as a practical approximation to describe the parametric uncertainty in most engineering applications, and the uncertainty distributions are assumed to be known ahead of time.[114,115]

One way of propagating uncertainty through the system is by developing stochastic differential equations (SDEs) to describe the system behaviour, where the input uncertainties are expressed as stochastic terms bounded by the uncertainty PDFs. Galerkin projection can be used in these systems to directly compute the variation in the model outputs based on the statistical moments of the uncertain parameter distributions. These methods are typically limited by complications with parameter determination, which has stimulated much interest in the development of accurate and efficient parameter estimation algorithms.[116–118] In addition, these methods require the use of closed-form differential equations, which are often unable to accurately approximate the complete behaviour of a multiscale system.

The effects of model-plant mismatch are most readily propagated through system models using direct computational techniques such as MC sampling. In this approach, numerous random realizations in the

parameter uncertainty descriptions are propagated through the system model in order to determine PDFs that describe the variability in the system outputs. This method has been previously employed in the literature to propagate uncertainty through a multiscale catalytic plug flow reaction system in order to determine the optimal catalyst for the decomposition of ammonia.[17] Although MC sampling accurately captures process variability, it requires large numbers of sample points to achieve the necessary accuracy, and can thence involve prohibitive computational costs.[10]

Alternatively, low-order mathematical models such as PSE and PCE can be formulated to efficiently approximate the behaviour of the primary model under uncertainty and represent the output variability using PDFs.[119,120] In the PSE approach, the relationship between the uncertain parameters and the system outputs is approximated using a Taylor series expansion, where the expansion derivative values are calculated using sensitivity methods. In contrast, the PCE approach uses orthogonal basis functions to approximate the relationship between the system outputs and the uncertain parameters. The coefficients to the PCE polynomials can be determined through intrusive methods such as Galerkin projection,[121] or non-intrusive methods such as non-intrusive spectral projection (NISP) and least-squares approximations.[122,123] A formal mathematical introduction to both series expansions will be provided in Chapter 4.

Both PSE and PCE have been incorporated into a number of optimal design and robust optimization studies for a variety of different system models.[124–126] In particular, the PSE approach has been previously implemented to propagate uncertainty through a multiscale thin film deposition model for robust optimization and online control applications.[83,127–130] PSE has additionally been implemented into back-off approaches for simultaneous design and control of dynamic systems subject to uncertainty,[131] in addition to optimal design processes, for applications in post-combustion CO_2 capture and reactor-heat exchanger systems.[132,133] Both PSE and PCE have been shown to accurately capture the variability of the system output due to parametric uncertainty.[119,120] The accuracy of each method depends on the system behaviour, the number of uncertain parameters, and the distribution of the uncertain parameters. Consequently, the optimal choice of series expansion varies from problem to problem. Previous comparisons for a multiscale thin film deposition system have demonstrated that PSE is the most attractive option when considering uncertainty in a single parameter, whereas PCE provides higher accuracy and efficiency for multivariate uncertainty analysis.[134]

Notwithstanding the existence of the aforementioned tools, uncertainty analysis in multiscale process systems remains a challenging and intensive task. Since multiscale models are not available in closed-form, employing methods such as PSE and PCE requires extensive numerical analyses. Due to the stochastic behavior of kMC simulations, it can be challenging to accurately determine the sensitivities for PSE-based uncertainty analysis in kMC-based multiscale models. In order to achieve reasonable accuracy, the sensitivities can be determined, at the cost of increased computational time, by taking the average over

multiple model simulations.[135,136] In addition, both PSE and PCE are subject to the trade-off between model accuracy and model efficiency. The accuracy of the PSE and PCE approximations improves with the addition of supplementary terms to the series expansion.[120,137,138] However, higher-order PSE expansions require the calculation of additional higher-order sensitivities that result in longer computational times. Similarly, higher-order PCE expressions require the calculation of additional PCE coefficients, thus requiring additional computational burdens. It is therefore desirable to determine the lowest expansion order that will provide acceptable accuracy in the results *a priori* in order to reduce the overall computational cost.

However, the implementation of even the lowest-order PSE and PCE expansions is limited in models that lack a closed-form representation, such as the aforementioned kMC-based multiscale processes. Although uncertainty propagation using PSE and PCE is more efficient than using the standard MC sampling, these propagation methods still demand significant numerical analysis and computational power. Consequently, these expansion-based approaches may become computationally-prohibitive to implement into robust optimization studies, where a unique PSE or PCE model is required for each operating point considered in the optimization process. This results in the need to simulate the multiscale model at each operating condition tested by the optimization algorithm.

Statistical DDMs are a commonly-used approach that provide a practical alternative to the PSE and PCE methods for performing computationally-efficient robust optimization of multiscale systems.[129,130,139] This modeling approach involves the identification of unique closed-form DDMs, which approximate the behaviour of key statistical properties in the reactor output variability (i.e. the mean, variance, and probabilistic bounds), using data collected from the system performance. However, the application of DDMs to industrial problems is practically limited. DDMs are developed over a finite range of the desired optimization parameters, and consequently, they cannot be used to accurately determine the system behaviour outside of these ranges. As a result, new DDMs would need to be constructed in order to evaluate the system performance outside of the defined optimization parameter range. In addition, DDMs can be computationally intensive to develop, as a significant number of data points are required in order to achieve sufficient accuracy. Despite these disadvantages, DDMs provide a practical and efficient means to perform optimization schemes for computationally-intensive systems such as the multiscale single-pore catalytic reactor system subject to parametric uncertainty that is considered in this work.

2.4 Summary

This chapter provided an overview of the literature and the methods employed in multiscale modeling with specific application to catalytic reactor systems. Relevant background knowledge was provided for

catalysis, catalytic reactors, and the multiscale methodology. Furthermore, the challenges encountered with the multiscale modeling of catalytic reactor systems and their potential solutions were discussed. In particular, the effects of model-plant mismatch and parametric uncertainty on the multiscale model performance were discussed. Despite the wide amount of solutions available for uncertainty propagation, there has been little research devoted to addressing model-plant mismatch in multiscale catalytic reactor systems. In addition, the effects of spatially-varying uncertainty due to catalyst deactivation on the multiscale reactor performance has not been studied. This provides motivation to perform uncertainty analysis on a catalytic reactor system and to investigate techniques to efficiently propagate uncertainty through the multiscale catalytic reactor for applications in optimization and process improvement studies.

Chapter 3
Catalytic Flow Reactor Multiscale Model Development

Catalytic reactor systems consist of a number of different events that occur on differing scales. The catalytic reactions that take place are molecular-level phenomena that describe the interactions between the various catalyst, reactant, and product species. In a heterogeneous catalyst system, these interactions often detail the adsorption, desorption, and reaction of the chemical species on the catalyst surface. Catalytic reactors also consist of a macroscopic phase, which details the flow of the reactant and the product species within the reactor. In order to accurately depict the diverse phenomena that occur in a catalytic system, multiscale modeling approaches are needed to simulate each of the events on their corresponding spatial and temporal lengths.

The objective of this chapter is to present the multiscale modeling approach employed within this work to model a multiscale single-pore catalytic flow reactor system. The multiscale single-pore catalytic reactor model was originally proposed by Majumder and Broadbelt,[14] and it has been extended for the applications considered in this work. Section 3.1 describes the catalytic reactor considered in this work and the reaction mechanisms that take place. Subsequently, Section 3.2 discusses the various modeling approaches (continuum modeling, kMC, and MF) used to simulate the different reactor scales. Further discussions are provided in Section 3.3 concerning the multiscale model assembly and the techniques implemented to ensure a solution approach. This section also compares the behaviour of the kMC-based and MF-based multiscale models to determine which kinetic modeling approach would be the most appropriate to consider for this work.

3.1 Reactor Design and Reaction Mechanism

The catalytic reactor system implemented in this work consists of a single pore in a porous catalytic membrane of length L and with pores of radius ρ, as presented in Figure 3-1a. The reactor consists of a thin film of catalytic material adhered to the interior of an inert porous support. The catalyst is assumed to be uniformly distributed along the inner support surface. Reactant molecules enter the reactor pore as a fluid and traverse axially along the pore length through convection. The fluid molecules are also subject to diffusion, which promotes radial molecular transport within the pore. Molecules at the solid-fluid interface can interact with the catalyst through adsorption and react to form products.

The reaction mechanism considered in this work consists of a spatially-dependent bimolecular reaction mechanism with two reactant species, A and B. This reaction mechanism has been previously implemented in the literature for multiscale catalytic reactor systems,[14,66] and it is the basis for many different bimolecular

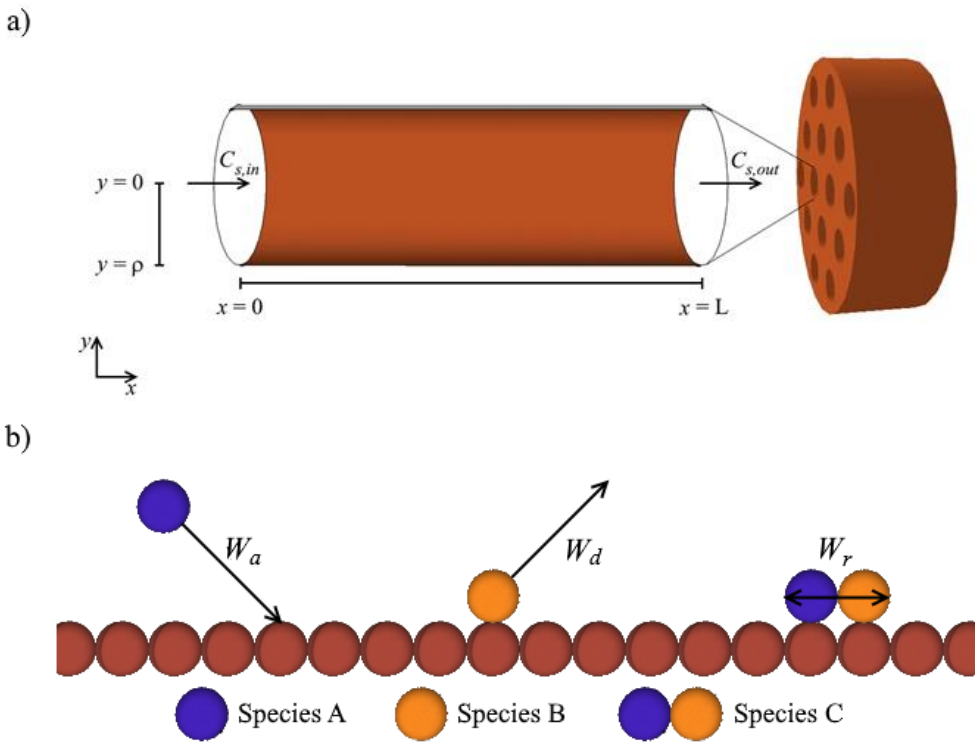

Figure 3-1. Schematic of a) the porous catalytic membrane; b) the kinetic reaction events, depicting molecules of species A (blue spheres), molecules of species B (orange spheres), molecules of species C (joint blue and orange spheres), and catalyst surface sites (brown spheres)

catalytic reaction systems such as the oxidation of carbon monoxide or the hydrogenation of olefins. The reactants chemisorb to the catalyst surface, where they can react to form a single gas-phase product, C, or desorb back into the gas phase, as depicted in Figure 3-1b. These reaction events can be represented according to the following equations:

$$A + * \rightleftharpoons A^* \tag{3-1}$$

$$B + * \rightleftharpoons B^* \tag{3-2}$$

$$A^* + B^* \rightarrow C + ** \tag{3-3}$$

In the equations above, $*$ and $**$ represent a single site and double empty sites on the catalyst surface respectively, while A^* and B^* represent the adsorbed forms of species A and B. Note that the adsorbed molecules are also capable of undergoing surface diffusion. However, for the reaction mechanism considered in this work, the rates of surface diffusion are assumed to be significantly slower than the rates of desorption and reaction, such that surface diffusion can be neglected.

3.2 Multiscale Modeling of the Catalytic Reactor System

The catalytic reactor behaviour is simulated using a multiscale modeling approach that discretizes the single-pore reactor into two subdomains. These domains consist of the macroscopic fluid phase domain, which is simulated by continuum modeling; and the microscopic catalyst surface domain, which is simulated using kinetic modeling approaches such as MF and kMC. The behaviour of each domain cannot be simulated without information from the other, and consequently information is passed between the two models through an overlapping 'handshake' region.[10] The following sections summarize the models used to approximate both the fluid phase and the catalyst surface domains of the multiscale model, while subsequent sections discuss the handshake region and the model coupling. The modeling approaches described below have been implemented to capture the transient behaviour of the catalytic reactor system. However, catalytic flow reactors are typically operated under continuous operating conditions,[1,4] and therefore the catalytic reactor models are typically developed to operate at steady-state. In this work, the single-pore catalytic reactor behaviour is evaluated under both transient and steady state conditions, and therefore the following sections will provide additional commentary on how the transient models can be adapted for steady-state operation.

3.2.1 Macroscopic Fluid Phase Domain

The macroscopic fluid phase model depicts the flow of the reactant and product species through the reactor pore using the continuum approach. Note that the present system is assumed to have a reasonably small Knudsen number, i.e. the fluid species are assumed to have sufficiently small mean free paths such that the continuum assumption is reasonable. The catalytic reaction is assumed to be isothermal, and the fluid flow within the reactor pore is assumed to be plug flow with a constant axial velocity across the reactor length. Additionally, the fluid phase is assumed to be dilute, such that the system temperature and pressure would not be significantly affected by the kinetic catalyst surface events. Thus, the momentum and heat transport equations can be assumed negligible and only the mass transport equation is used to determine the macroscopic reactor behaviour. The reactor pore is treated as perfect cylinders and therefore the angular terms of the continuum models can be neglected. In addition, the fluid velocity is assumed to be sufficiently large such that axial diffusion can be neglected. As a result, the fluid phase behaviour can be described by the following 2D Cartesian mass transport PDE:

$$\frac{\delta C_s(x,y,t)}{\delta t} = D_s \frac{\delta^2 C_s(x,y,t)}{\delta y^2} - \nu \frac{\delta C_s(x,y,t)}{\delta x} \tag{3-4}$$

where $C_s(x, y, t)$ denotes the molar concentration of chemical species s at an axial distance x from the reactor inlet and a radial distance y from the pore center at time t; D_s represents the diffusion coefficient for species s; and v represents the fluid velocity. Eq. (3-4) has the following boundary conditions:

$$C_s(0, y, t) = C_{s,in} \tag{3-5}$$

$$\frac{\delta C_s(x,0,t)}{\delta y} = 0 \tag{3-6}$$

$$D_s \frac{\delta C_s(x,\rho,t)}{\delta y} = -\omega_{s,ads}(x, \rho, t) + \omega_{s,des}(x, \rho, t) + \omega_{s,prod}(x, \rho, t) - \omega_{s,cons}(x, \rho, t) \tag{3-7}$$

$$C_s(x, \rho, t) = C_{s,in} \tag{3-8}$$

where $C_{s,in}$ denotes the inlet concentration of species s, whereas $C_{s,out}(t)$ denotes the outlet concentration of species s at the center of the pore outlet $(x = L, y = 0)$ at time t. Furthermore, $\omega_{s,ads}(x, \rho, t)$ and $\omega_{s,des}(x, \rho, t)$ denote the rates of adsorption and desorption respectively for species s along the catalyst surface $(y = \rho)$ at an axial length x and time t, while $\omega_{s,cons}(x, \rho, t)$ denotes the rate of consumption of a fluid phase species s through reaction with adsorbed molecules at a location (x, ρ) and time t, and $\omega_{s,prod}(x, \rho, t)$ denotes the rate of production species s directly into the gas phase at (x, ρ) and time t following the reaction. Note that the parameters $\omega_{s,ads}$, $\omega_{s,des}$, $\omega_{s,prod}$, and $\omega_{s,cons}$ in Eq. (3-7) need to be estimated from the microscopic catalyst surface model. Additionally, the transient fluid phase continuum model depicted above can be readily adapted to operate at steady state. This can be accomplished by setting the time derivative in Eq. (3-4) to zero and ignoring the initial condition presented in Eq. (3-8).

3.2.2 Microscopic Catalyst Surface Domain

The behaviour of the catalyst surface domain depends exclusively upon the rates of the microkinetic events taking place. The events considered in this work include the adsorption of the chemical species to the catalyst surface, the desorption of the species from the catalyst surface, and the reaction between adsorbed reactants to form products. The catalyst surface behaviour can be simulated using kinetic modeling approaches such as the MF approximation and lattice-based kMC.

Although it is preferable to use the MF approximation due to its lower computational costs, it can only be implemented in catalytic reaction applications where lateral interactions and spatial heterogeneities have a negligible effect on the results. The reaction mechanism considered in this work requires lateral interactions between adsorbed molecules of species A and B, as denoted in Eq. (3-3). Therefore, it is

necessary to assess the accuracy of the MF approximation against the catalyst surface behaviour determined through kMC in order to establish which kinetic modeling approach should be used in this work. The following sections detail each of the kinetic modeling methods and their incorporation into the multiscale model. The MF approximation and the lattice-based kMC approach will be compared in a later section (Section 3.3.2) to determine which modeling approach will be implemented throughout the remainder of this work.

3.2.2.1 Mean-Field Approximation

The objective of the MF approximation is to determine the fractional coverage of each adsorbed species on the catalyst surface as a function of time. Each of the adsorbed molecules is assumed to be homogeneously distributed,[14] and as a result the surface coverages for the reaction mechanism considered in this work (Eqs. (3-1)-(3-3)) can be determined using the following ODEs:

$$\frac{\delta\theta_A(x,\rho,t)}{\delta t} = k_{a,A}C_A(x,\rho,t)\theta_e(x,\rho,t) - k_{d,A}\mathrm{e}^{-\frac{E_{d,A}}{RT}}\theta_A(x,\rho,t) - k_r\mathrm{e}^{-\frac{E_r}{RT}}\theta_A(x,\rho,t)\theta_B(x,\rho,t) \quad (3\text{-}9)$$

$$\frac{\delta\theta_B(x,\rho,t)}{\delta t} = k_{a,B}C_B(x,\rho,t)\theta_e(x,\rho,t) - k_{d,B}\mathrm{e}^{-\frac{E_{d,B}}{RT}}\theta_B(x,\rho,t) - k_r\mathrm{e}^{-\frac{E_r}{RT}}\theta_A(x,\rho,t)\theta_B(x,\rho,t) \quad (3\text{-}10)$$

where $\theta_A(x,\rho,t)$, $\theta_B(x,\rho,t)$, and $\theta_e(x,\rho,t)$ denote the local fractional coverages of species A, species B, and empty catalyst sites respectively at an axial length x along the catalyst surface ($y = \rho$) and at time t; $k_{a,A}$ and $k_{a,B}$ denote the adsorption rate constant for species A and B respectively; $k_{d,A}$ and $k_{d,B}$ denote the desorption rate constant for species A and B respectively; $E_{d,A}$ and $E_{d,B}$ denote the activation energy of desorption for species A and B respectively; R is the ideal gas constant; T represents the temperature of the reactor; k_r denotes the reaction rate constant; and E_r denotes the activation energy of reaction. These ODEs are subject to the following initial condition:

$$\theta_s(x,\rho,0) = 0 \quad (3\text{-}11)$$

Note that the MF models are built under an infinite diffusion assumption, (i.e. adsorbates are assumed to diffuse freely across the catalyst surface) and as a result any two adsorbed molecules of species *A* and *B* can react with each other, regardless of their location on the catalyst surface. Similar to the macroscopic fluid phase continuum model, the MF ODEs can be readily modified to determine the steady state catalyst surface coverages. This can be achieved by setting the time derivatives to zero and ignoring the initial

conditions, which simplifies the MF equations into a series of algebraic expressions that can be solved using root-finding methods. Further details concerning the MF approximation can be found in the literature.[14,64]

3.2.2.2 Lattice-based Kinetic Monte Carlo

The lattice-based kMC model is a MC-based stochastic approach that determines the catalyst surface behaviour by executing catalytic events based on their kinetic rates. These catalytic surface events are simulated using a kMC algorithm implemented with a finite square lattice and assuming periodic boundary conditions. In the present model, it is assumed that each catalyst surface site can be occupied by a single adsorbate molecule, and additionally all surface reactions are limited to interactions between first nearest neighbours for simplicity.

The rate of adsorption is derived from the kinetic theory of ideal gases,[140] and depends upon the concentration of chemical species within the fluid phase. Consequently, it cannot be determined without prior assessment of the macroscopic fluid flow behaviour. The rate of adsorption can be expressed according to the following formulation:

$$W_{a,s}(x,\rho,t) = C_s(x,\rho,t)N_e(x,\rho,t)k_{a,s} \tag{3-12}$$

Here, $W_{a,s}(x,\rho,t)$ represents the total rate of adsorption of the s^{th} species on the catalyst surface ($y = \rho$) located at an axial distance x from the pore entrance and at time t, while $N_e(x,\rho,t)$ denotes the local number of empty sites on a kMC lattice at (x,ρ,t).

The rate of desorption can be determined using an Arrhenius type expression as follows:

$$W_{d,s}(x,\rho,t) = N_s(x,\rho,t)k_{d,s}\mathrm{e}^{-\frac{E_{d,s}}{RT}} \tag{3-13}$$

In this equation, $W_{d,s}(x,\rho,t)$ represents the total rate of desorption of the s^{th} species on the catalyst surface ($y = \rho$) located at an axial distance x from the pore entrance and at time t, and N_s is the total number of sites occupied by species s on the lattice at (x,ρ,t).

The rate of reaction is dependent on the number of relevant reactant species present on the catalyst surface and their proximity to each other. In order for the reaction to occur, the necessary reactants must be adsorbed adjacent to each other on the catalyst surface due to the first nearest neighbour interaction approximation. These groupings of close-proximity adsorbates capable of reacting are defined as a surface

reactant ensemble.[66] The surface reactant ensemble for the reaction mechanism considered in this work (Eqs. (3-1)-(3-3)) consists of two adjoined molecules of species A and B adsorbed on the catalyst surface. The rate of reaction is as follows:

$$W_r(x,\rho,t) = \frac{N_r(x,\rho,t)}{8} k_r \mathrm{e}^{-\frac{E_r}{RT}} \tag{3-14}$$

where $W_r(x,\rho,t)$ denotes the total rate of reaction at (x,ρ) and time t, while $N_r(x,\rho,t)$ denotes the total number of surface reactant ensembles on the surface lattice at (x,ρ,t). Since the surface reactant ensembles are allowed to form in any four directions on the lattice surface, as depicted in Figure 3-2, N_r in Equation (3-14) accounts for all these ensembles.

The lattice-based kMC algorithm used in this work can be outlined as follows. The kinetic rates are first determined for every possible kinetic event using Eqs. (3-12)-(3-14). Note that the kinetic parameters in these equations are derived from experimental data or from DFT simulations. Once the kinetic rates have been determined, a random number ζ_1 is generated from the standard uniform distribution (i.e. $0 < \zeta_1 < 1$), and is used to select a kinetic event to execute on the kMC lattice. The kinetic event is chosen by mapping each of the possible events along the interval between 0 and 1 based on their kinetic rates, and selecting an event within this range using ζ_1. For the reaction mechanism considered in this work, this selection process can be described using the following set of rules:

- If $0 < \zeta_1 \leq \frac{W_{a,A}}{\sum_s^{n_s}(W_{a,s}+W_{d,s})+W_r}$, then adsorption of species A is selected.
- If $\frac{W_{a,A}}{\sum_s^{n_s}(W_{a,s}+W_{d,s})+W_r} < \zeta_1 \leq \frac{W_{a,A}+W_{a,B}}{\sum_s^{n_s}(W_{a,s}+W_{d,s})+W_r}$, then adsorption of species B is selected.
- If $\frac{\sum_s^{n_s}(W_{a,s})}{\sum_s^{n_s}(W_{a,s}+W_{d,s})+W_r} < \zeta_1 \leq \frac{\sum_s^{n_s}(W_{a,s})+W_{d,A}}{\sum_s^{n_s}(W_{a,s}+W_{d,s})+W_r}$, then desorption of species A is selected.
- If $\frac{\sum_s^{n_s}(W_{a,s})+W_{d,A}}{\sum_s^{n_s}(W_{a,s}+W_{d,s})+W_r} < \zeta_1 \leq \frac{\sum_s^{n_s}(W_{a,s})+W_{d,A}+W_{d,B}}{\sum_s^{n_s}(W_{a,s}+W_{d,s})+W_r}$, then desorption of species B is selected.
- If $\frac{\sum_s^{n_s}(W_{a,s}+W_{d,s})}{\sum_s^{n_s}(W_{a,s}+W_{d,s})+W_r} < \zeta_1 \leq 1$, then reaction is selected.

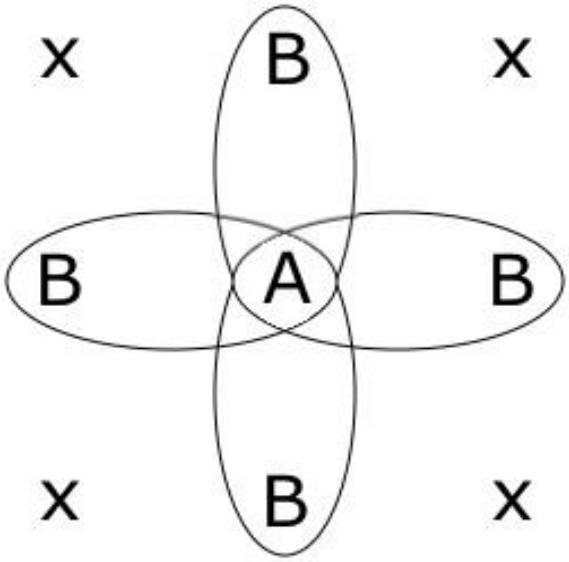

Figure 3-2. Four A-B surface reactant ensembles on a kMC lattice.

Here, n_S denotes the total number of chemical species in the system. Once an event has been selected, a second uniform random number, ζ_2, is generated from the standard uniform distribution to select the location on the lattice surface where the event will occur. Note that not all lattice sites are capable of executing each kinetic event, i.e. adsorption can only occur on an empty catalyst site, desorption of species s can only occur on a site where a molecule of s is adsorbed, and reaction can only occur where surface reactant ensembles exist. It is therefore necessary to keep track of the location of each empty site, adsorbed molecule, and surface reactant ensemble on the catalyst surface in order to appropriately select a site to execute a particular kinetic event. The site is selected by multiplying ζ_2 by the total number of available event sites (N_e, N_s, or N_r) and rounding up to determine the site number. Once an appropriate site has been randomly selected, the kinetic event is executed. If the selected event is reaction, then the reaction counter $M_{C,prod}(x,\rho,t)$ is incremented by one. This reaction counter is defined as the number of molecules of species C produced directly into the fluid phase from a kMC lattice at (x,ρ) and at time t, and it is needed to calculate the surface boundary condition (Eq. (3-7)) in the macroscopic fluid phase model, as will be discussed in the next section. Following the event execution, the time of reaction is incremented as follows:

$$\tau_\iota(x,\rho) = -\frac{\ln(\zeta_3)}{\sum_s^{n_S}[W_{a,s}(x,\rho,t)+W_{d,s}(x,\rho,t)]+W_r(x,\rho,t)} \tag{3-15}$$

where $\tau_\iota(x,\rho)$ denotes the amount of time that has passed between the current executed kinetic event and the previously-executed kinetic event, and ζ_3 is a third random number generated from the standard uniform distribution. The cycle repeats until the final time Δt_{MST} has been reached in a transient system. A complete flowchart of the implemented kMC algorithm is displayed in Figure 3-3a. Alternatively, in a time-independent system, the kMC cycle ends once lattice has reached steady state. It is assumed that a lattice has attained steady state when the change in the number of adsorbed molecules over the past 1000 kMC events falls below the kMC tolerance criterion, ε_{kMC}. A complete flowchart of the steady-state kMC algorithm is illustrated in Figure 3-3b.

3.2.3 The Handshake Region

The macroscopic fluid phase model and the microscopic catalyst surface model both rely on terms that are dependent upon the other domain, and thus cannot be solved independently. Communication between the two domains occurs at a 'handshake' region, which exists where there is overlap between the domains.[10] Information regarding the concentrations of the chemical species at the catalyst surface is passed from the fluid phase model to the catalyst surface model, where it is used to determine the kinetic rates of the surface events. Similarly, the concentration of adsorbates and the number of reactions that occurred on the catalyst surface over a set period of time are passed back to the fluid phase domain model in order to compute the rates of the surface boundary condition presented in Eq. (3-7). Note that the rates depicted in Eq. (3-7) depend on the kinetic model used to simulate the microscopic catalyst surface behaviour. If the MF approximation is implemented into the multiscale model, then the rates in Eq. (3-7) for the bimolecular reaction mechanism considered in this work (Eqs. (3-1)-(3-3)) can be determined as follows:

$$\omega_{s,ads}(x,\rho,t) = \lambda k_{a,s} C_s(x,\rho,t)\theta_e(x,\rho,t) \tag{3-16}$$

$$\omega_{s,des}(x,\rho,t) = \lambda k_{d,s} \mathrm{e}^{-\frac{E_{d,s}}{RT}} \theta_s(x,\rho,t) \tag{3-17}$$

$$\omega_{C,prod}(x,\rho,t) = \lambda k_r \mathrm{e}^{-\frac{\mathrm{E_r}}{RT}} \theta_A(x,\rho,t)\theta_B(x,\rho,t) \tag{3-18}$$

$$\omega_{s,cons}(x,\rho,t) = 0 \tag{3-19}$$

where λ is a unit conversion constant whose value depends on the concentration of active sites on the catalyst surface and can be calculated as follows:

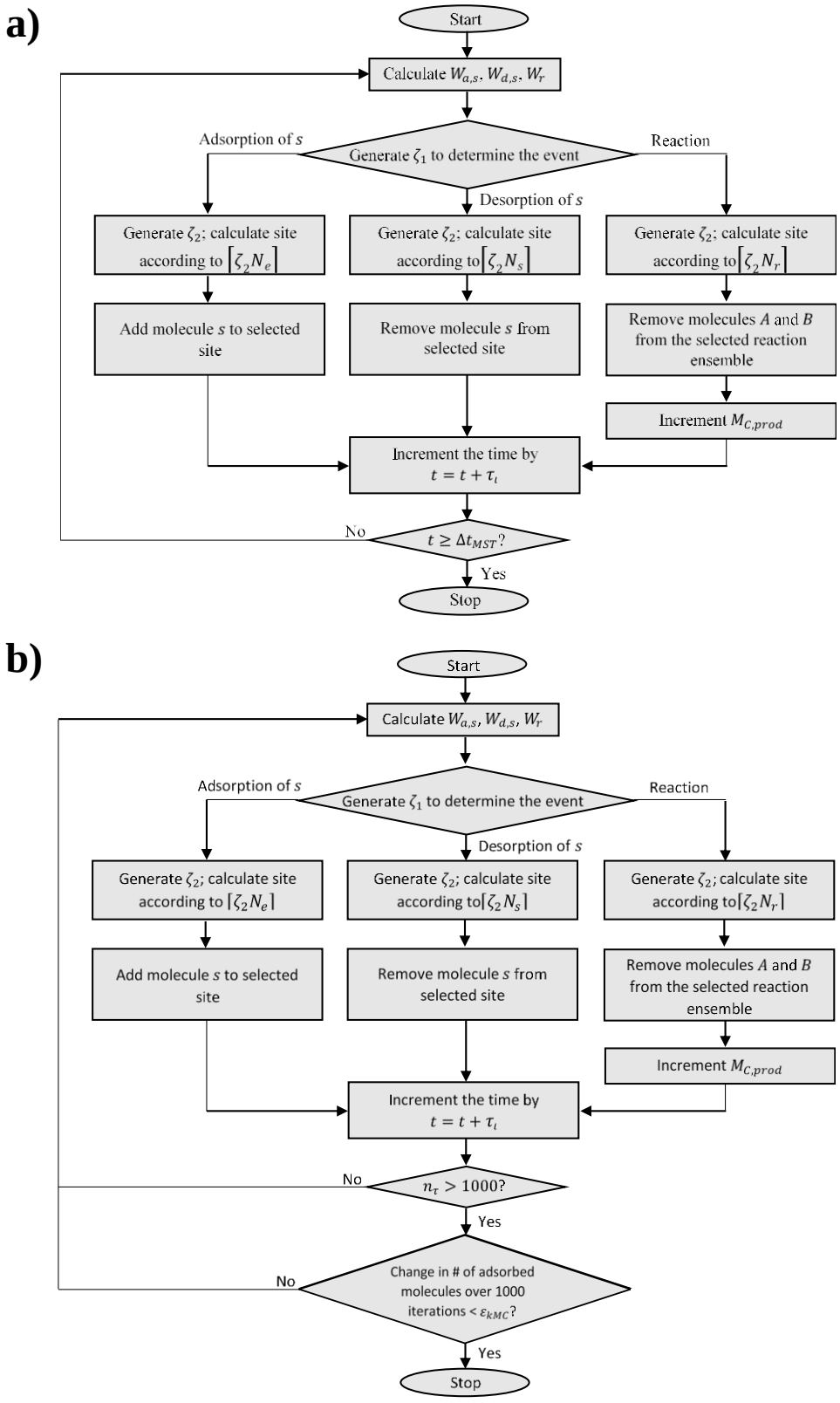

Figure 3-3. Flowchart of: a) the transient kMC algorithm; b) the steady-state kMC algorithm.

$$\lambda = \kappa \frac{C_{site}}{N_{Av}} \tag{3-20}$$

where $\kappa = 0.001 \frac{\mathrm{m}^3}{\mathrm{L}}$ is a unit conversion factor, C_{site} denotes the active site concentration on the catalyst surface, and N_{Av} is Avogadro's number.

On the other hand, if kMC is implemented into the multiscale model, then for the reaction mechanism considered in this work, the rates in Eq. (3-7) can be determined as follows:

$$\omega_{s,ads}(x,\rho,t) = \lambda k_{a,s} C_s(x,\rho,t) \frac{N_e(x,\rho,t)}{N_{total}} \tag{3-21}$$

$$\omega_{s,des}(x,\rho,t) = \lambda k_{d,s} \mathrm{e}^{-\frac{E_{d,s}}{RT}} \frac{N_s(x,\rho,t)}{N_{total}} \tag{3-22}$$

$$\omega_{C,prod}(x,\rho,t) = \lambda \frac{M_{C,prod}(x,\rho,t)}{N_{total} \sum_{\iota=1}^{n_\tau(x,\rho,t)} \tau_\iota(x,\rho,t)} \tag{3-23}$$

$$\omega_{s,cons}(x,\rho,t) = 0 \tag{3-24}$$

where N_{site} denotes the total number of catalyst sites on the kMC lattice, and $M_{C,prod}(x,\rho,t)$ denotes the number of molecules of C produced directly into the fluid phase via reaction over $n_\tau(x,\rho,t)$ kinetic events on the catalyst surface ($y = \rho$) at an axial distance x and at time t.

The single-pore catalytic reactor considered in this work is spatially-heterogeneous which produces concentration gradients along the axial length of the fluid phase domain. Thus, the catalyst surface behaviour varies as a function of the reactor length and unique MF equation evaluations or kMC lattice simulations are required in order to simulate the catalyst behaviour at every point along the reactor surface.[90] Alternatively, spatial coarse-graining techniques such as the gap-tooth method can be incorporated into the handshake region to approximate the axial variation of the catalytic surface events using significantly fewer MF equations or kMC lattices.[91–95] The gap-tooth approach incorporated in this work subdivides the axial length of the catalyst surface into n_{teeth} 'teeth', where the microkinetic activity is directly computed using independent kMC lattices. The teeth are separated by 'gaps', where the microkinetic activity is approximated through interpolation. The teeth are equidistantly spaced, such that each tooth is located at a fixed position along the catalyst surface (x_{tooth}, ρ, t) for all time t. The first tooth is considered at the reactor entrance $(0, \rho, t)$, and the last tooth is considered at the reactor's outlet (L, ρ, t). The process begins by 'lifting' concentrations out of the fluid phase at each tooth location on the catalyst surface to calculate the adsorption rates. The catalyst surface at each tooth is allowed to evolve using independent kMC or MF simulations, i.e. each tooth has its own lattice-based kMC model or series of MF equations representing the

catalyst surface at that particular point in the reactor's spatial domain. The microkinetic activity is extracted at each tooth and interpolated to approximate the activity across each gap. The process concludes through 'restriction', where the complete set of microkinetic data is returned to the fluid phase model through the boundary conditions presented in Eq. (3-7). Note that decreasing the number of teeth used in the gap-tooth model will lower the computational cost at the price of decreased model accuracy. Consequently, it is necessary to determine the minimum number of required teeth required to achieve suitable accuracy *a priori*. For the catalytic reactor system implemented in this work, the number of teeth used varied between seven and eight teeth, depending on the application.

3.3 Multiscale Model Assembly and Solution Approach

The multiscale model is assembled to assess the transient behaviour of the single-pore catalytic reactor system. At the beginning of the simulation, the fluid phase continuum models are solved using an implicit Euler method FD approach that subdivides the reactor interior into 101 axial points and 43 radial points. The continuum models are solved using a temporal step size of Δt_{FD} = 0.01s, until the initial multiscale trade-off time Δt_{MST} = 0.2s has been attained. Increasing the number of discretization points does not enhance the model accuracy and results in additional unnecessary computational cost. Subsequently, the fluid concentrations are extracted near the catalyst surface and used to determine the microkinetic rates for the MF equations and the kMC lattices at each tooth in the gap-tooth model. For the MF approximation, the MF ODEs (Eqs. (3-9) and (3-10)) are solved at each point using an explicit Runge-Kutta-Fehlberg (Runge-Kutta (4,5)) method until the total MF integration time reaches Δt_{MST}. For the kMC approach, independent kMC simulations are applied at each tooth until the kMC integration time reaches t_{MST}. The noise in the kMC results is reduced by using an average of the outputs over the last 1,000 kMC events. Afterward, the relevant catalyst surface information is extracted for each tooth and interpolated using cubic interpolation to determine the values across the gaps. These values are plugged into the surface boundary condition (Eq. (3-7)) and used to re-evaluate the fluid phase behaviour over another time interval t_{MST}. This multiscale cycle is repeated until the overall reactor time has reached the final simulation time t_{final}. Figure 3-4a provides an illustration of the overall multiscale model algorithm. Note that the multiscale trade-off time (Δt_{MST}) denotes the time domain over which each modeling method is simulated before communicating with the other modeling method. Using larger multiscale trade-off times can decrease the computational cost of the multiscale model, but larger values of Δt_{MST} can additionally produce instabilities in the model coupling. Consequently, it is necessary to determine *a priori* the maximum value of Δt_{MST} that will not produce any instabilities.

The algorithm for the steady-state multiscale catalytic reactor model is similar to that of the transient model described previously. At the start of the reactor simulation, the steady-state fluid phase continuum models are solved using an elliptic FD approach. The spatial domain of the reactor is discretized into 43 radial points and 101 axial points, akin to the transient model. The fluid concentrations are subsequently extracted at each of the tooth locations on the catalyst surface and used as inputs for the MF and kMC approaches. If the MF model is used, the steady-state MF equations are solved at each tooth using root-finding methods. Alternatively, if the kMC model is used, kMC simulations are used to evolve the catalyst surface behaviour at each tooth until the surface lattices have reached steady state. It is assumed that a lattice has attained steady state when the change in the number of adsorbed molecules for each species falls below the kMC tolerance criterion, ε_{kMC}, over the last 1,000 kMC events. The noise in the kMC results is additionally reduced by taking an average of the outputs over the last 1,000 kMC events. The outputs from both kinetic modeling methods at each tooth are subsequently interpolated to determine the values along the gaps. These values are inserted into the surface boundary condition (Eq. (3-7)), and the fluid phase behaviour is re-assessed based on the updated catalyst surface information. This cycle is repeated until the maximum variation in the species concentrations at each point (x, y) within the reactor model is less than the multiscale tolerance criterion, ε_{MS}, at which point the system is assumed to be at steady state. A graphical representation of the steady-state multiscale algorithm can be found in Figure 3-4b.

3.3.1 Lattice Size Determination

Due to the stochastic nature of the kMC simulations, the responses obtained from the multiscale model can be noisy depending on the lattice size. Larger lattices produce more accurate results since stochastic fluctuations have less impact due to the increased number of sites. However, larger lattices require more kMC event steps to reach the same integration times as smaller lattices, which results in additional computational costs. Therefore, a lattice size that provides enough accuracy while still maintaining as low a computational cost as possible must be specified through offline analysis. Figure 3-5 shows the evolution of the surface coverage for species A on the first tooth approximated using 30x30, 100x100, and 200x200 kMC lattice sizes. The 30x30 lattice is able to capture the general behaviour of the surface evolution process; however, the noise in the response impedes accurate determination of the surface coverage values. Alternatively, larger lattices provide a good approximation of the surface evolution during the kMC simulation with minimal noise. No significant improvement is observed between the 100x100 and 200x200 lattice sizes. However, both larger lattices require significantly more computational time compared to the 30x30 lattice as can be seen in the computational times recorded in the caption of Figure 3-5. To improve the accuracy of the smaller lattice-size kMC simulations without gaining significant additional

a)

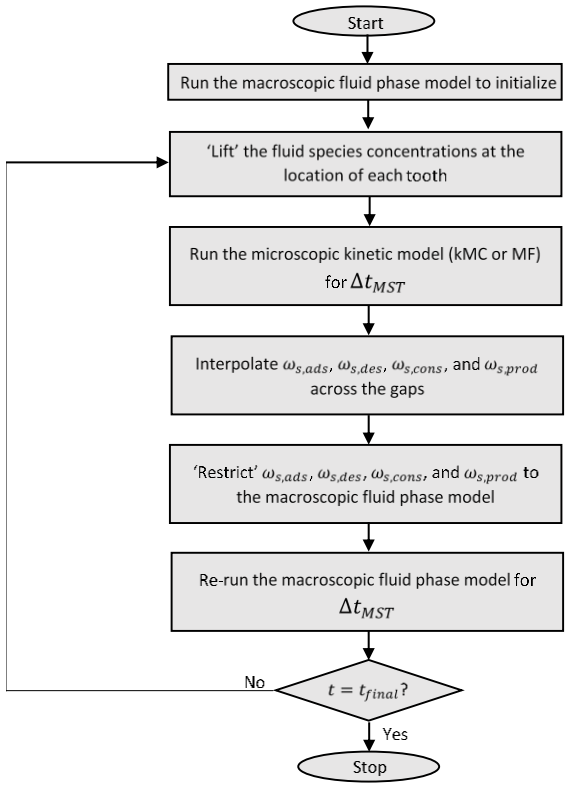

b)

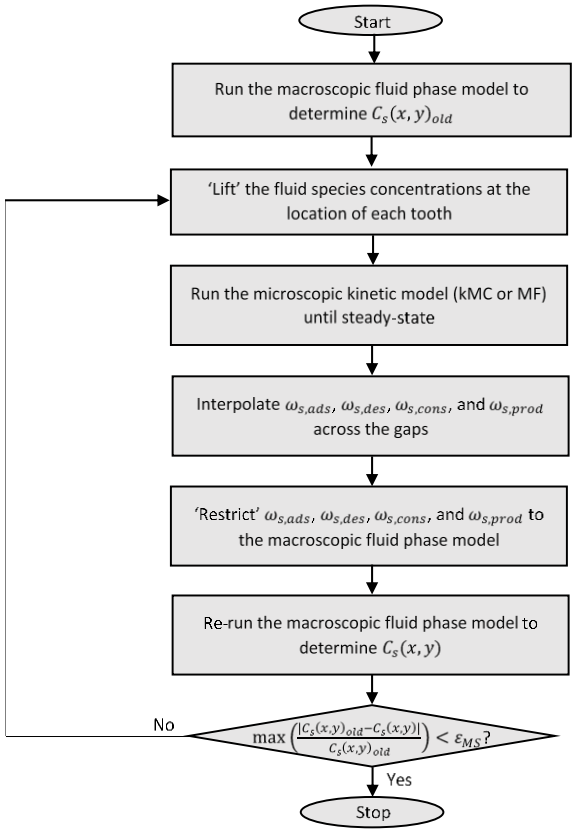

Figure 3-4. Flowchart of: a) the transient and b) the steady-state multiscale algorithms.

computational time, the results from eight independent 30x30 lattice kMC simulations are averaged and compared to the previous simulation results. This averaging technique has been used in previous studies to reduce the noise produced by smaller kMC lattices.[13,83] As shown in Figure 3-5, the noise in the coverage of species *A* using the averaged 30x30 lattices is comparable to the noise of the result obtained from a 100x100 lattice. Furthermore, as presented in the caption of Figure 3-5, the computational time for the averaged 30x30 lattice approach is significantly lower as compared to the higher lattice sizes. The present work, therefore, employs the average of eight independent multiscale simulations utilizing 30x30 kMC lattice sizes to represent the evolution of the surface catalyst. In order to further reduce the computational costs, parallel computation techniques are also implemented to calculate each of the eight multiscale simulations in parallel.

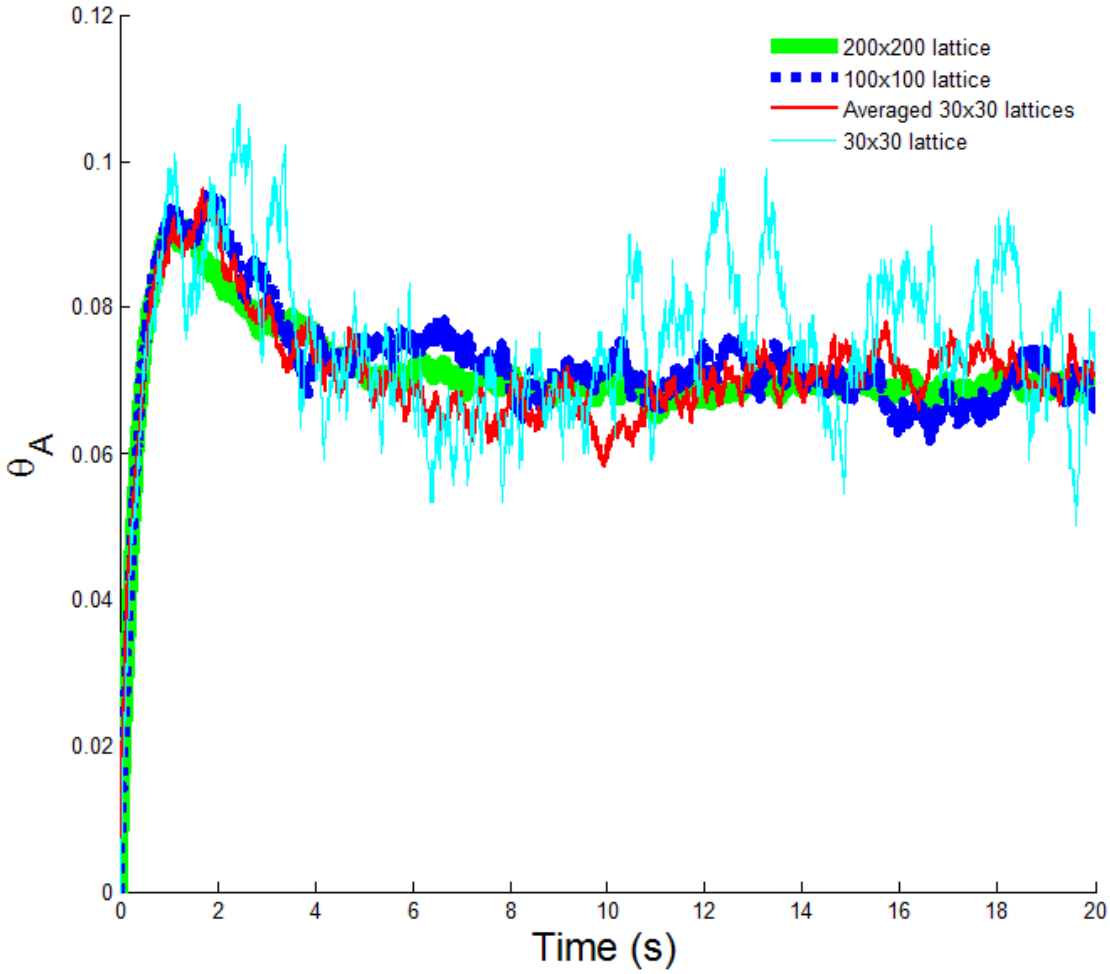

Figure 3-5. Comparison of the surface coverage evolution of species *A* at the first reactor tooth using 30x30 (1s), 100x100 (21s), 200x200 (422s), and an average of eight 30x30 (3s) lattices in the kMC simulations.

Note that the computational costs of the kMC algorithm can be reduced through decoupling techniques, where the predominant kinetic events are decoupled from the kMC model and handled deterministically.[74] For the reaction mechanism considered in this work, the predominant kinetic events under nominal conditions consist of the adsorption of species A and B, which each account for 32% of the total kinetic events (i.e. they were each executed 32% of the time by the kMC model). However, these adsorption terms cannot be decoupled from the kMC model, as these events determine the configuration of the adsorbates on the catalyst surface, which is necessary to determine the location of the surface reactant ensembles required to accurately determine the kinetic rates of reaction.

3.3.2 Comparison of Mean-Field and Kinetic Monte Carlo

In order to investigate the performance of the MF approximation with respect to the lattice-based kMC approach, multiscale models were developed for both methods. These multiscale models were subsequently used to simulate the behaviour of a single-pore catalytic flow reactor at steady state under the nominal conditions presented in Table 3-1. The values for these parameters were derived from a previous study by Dooling and Broadbelt.[66] The computational costs (3.4GHz Intel i7-3770 processor) and outlet concentration of each chemical species of both modeling approaches are listed in Table 3-2. In addition, Figure 3-6 illustrates the axial concentration profiles derived from both multiscale models at the catalyst surface ($y = \rho$). In the aforementioned figure, the circles illustrate the local concentrations at each of the teeth considered in the gap-tooth model. The results in Table 3-2 illustrate that the computational costs of the kMC-based multiscale model (92s) are approximately 30 times higher than the computational costs of the MF-based multiscale model (3s), demonstrating the computational advantages of using the MF approximation over kMC simulations. However, the results presented in Table 3-2 and Figure 3-6 reveal a large discrepancy between the MF-based multiscale results and the kMC-based multiscale results. Specifically, the MF-based multiscale model significantly over-predicts the number of reactions taking place on the catalyst surface, resulting in a final product concentration that is 1.7 times the product concentration obtained using the kMC-based multiscale model. These results are to be expected, as the MF approximation is unable to account for lateral interactions and other catalyst surface spatial heterogeneities. On the other hand, the kMC approach can readily incorporate these spatial catalyst surface phenomena, resulting in significantly improved accuracy in the model results. These results demonstrate that lateral interactions play a major role in the reaction mechanism considered in this work, and as a result the MF-based multiscale model is unable to accurately predict the catalytic reactor behaviour. This is in accordance with previous analyses that have been performed in the literature for bimolecular reaction mechanisms.[14] As a result, the kMC-based multiscale model was determined to be the superior model for this application

Table 3-1. Nominal parameter values for the multiscale catalytic reactor model.

Parameter	Value	Units
$C_{A,in}$	241	mmol/L
$C_{B,in}$	241	mmol/L
$C_{C,in}$	0	mmol/L
D_A	5300	μm^2/s
D_B	5300	μm^2/s
D_C	5300	μm^2/s
$E_{d,A}$	95	kJ/mol
$E_{d,B}$	100	kJ/mol
E_r	57	kJ/mol
$k_{a,A}$	1	molecule·L/(mol·site·s)
$k_{a,B}$	1	molecule·L/(mol·site·s)
$k_{d,A}$	10	molecule/(site·ns)
$k_{d,B}$	10	molecule/(site·ns)
k_r	16	molecule/(site·μs)
L	1	μm
n_s	3	chemical species
T	450	K
λ	2.08	sites·μm·mol/(L·molecule)
C_{site}	1.25×10^{21}	sites/m^2
ε_{kMC}	5	%
ε_{MS}	5	%
ν	10	mm/s
ρ	10	nm

and therefore it was incorporated into the modeling approaches implemented throughout the remainder of this work.

Table 3-2. Concentration of each chemical species at the reactor outlet as determined by the MF-based and kMC-based multiscale models

	Total CPU Time (s)	$C_{A,out}$ **(mmol/L)**	$C_{B,out}$ **(mmol/L)**	$C_{C,out}$ **(mmol/L)**
MF-Based Multiscale Model	3	238.2251	238.2251	2.7749
kMC-Based Multiscale Model	92	239.3588	239.3617	1.6422

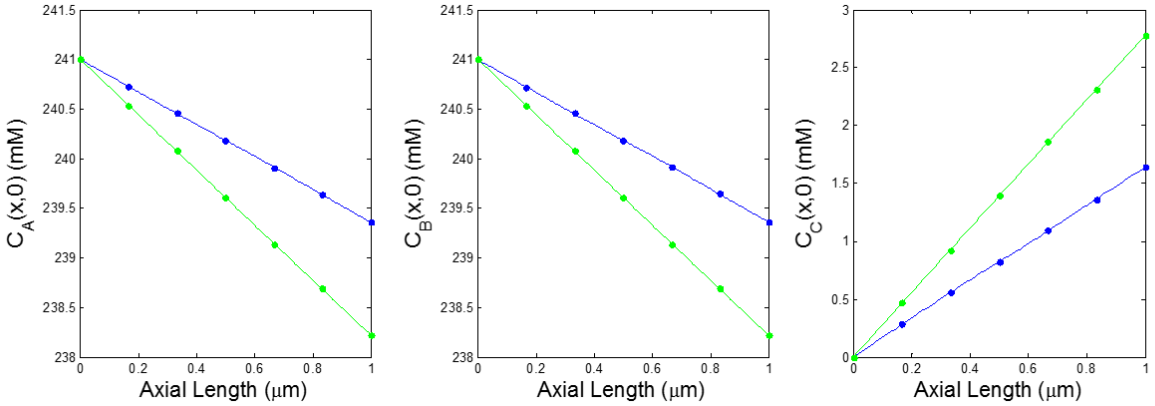

Figure 3-6. Axial concentration profiles on the catalyst surface ($y = \rho$) for the MF-based multiscale model (green) and the kMC-based multiscale model (blue) for a) Species A, b) Species B, c) Species C. The circles denote the locations of the teeth used in the gap-tooth approximation for both multiscale models.

3.4 Summary

This chapter provided an extensive description of the single-pore catalytic flow reactor system considered in this work and the multiscale modeling approach used to capture the reactor's behaviour. The multiscale model combined continuum modeling approaches to capture the macroscopic behaviour of the reactor fluid phase with MF or lattice-based kMC to describe the microscopic catalyst surface behaviour. Furthermore, the gap-tooth approach was implemented to manage the effects of the fluid phase

concentration gradients on the catalyst surface behaviour. The models discussed were developed to capture the transient behaviour of the catalytic reactor system. Discussion was also provided regarding the modification of these models to capture the steady state behaviour of the reactor. Furthermore, the MF and kMC approaches were compared to determine which model would be most suitable for capturing the catalyst surface behaviour in the multiscale reactor system. When compared to the kMC approach, the MF approximation required substantially lower computational costs. However, its inability to account for lateral surface interactions limit its ability to provide sufficient accuracy. As a result, the kMC-continuum multiscale model was implemented throughout the remainder of this work.

Chapter 4
Uncertainty Propagation using Polynomial Chaos Expansions and Power Series Expansions

It is well-established that uncertainty in key parameters of a catalytic reactor system can result in significant model-plant mismatch.[21–23,96] This is especially detrimental for optimization and process improvement studies, which depend upon model accuracy to predict and improve reactor performance. Uncertainty analysis seeks to quantify the difference $\Delta\boldsymbol{\psi}(x,y,t)$ between the actual outputs $\widehat{\boldsymbol{\psi}}(x,y,t)$ and the predicted outputs $\boldsymbol{\psi}(x,y,t)$ at a specific spatial point (x,y) within the reactor interior at any time t. This is accomplished by implementing probabilistic or bound restraints on each model output $\psi_n(x,y,t)$, where $\psi_n(x,y,t)$ denotes the nth model output in $\boldsymbol{\psi}(x,y,t)$, based on the uncertainty of the input parameters $\boldsymbol{\Phi}$ through the identification of output PDFs, $f_{PD,\psi_n(x,y,t)}$. These output PDFs provide the data required to determine statistical information such as the mean $\mu\big(\psi_n(x,y,t)\big)$ and variance $\sigma^2\big(\psi_n(x,y,t)\big)$. Additionally, $f_{PD,\boldsymbol{\psi}(x,y,t)}$ can be used to determine probabilistic bounds $\psi_n^{up}(x,y,t)$ and $\psi_n^{lw}(x,y,t)$ to evaluate $\psi_n(x,y,t)$ at a particular confidence level, α, i.e.

$$\psi_n^b(x,y,t) = F^{-1}\big(\Pi\big|\psi_n(x,y,t)\big) \tag{4-1}$$

where $b \in \{up, lw\}$, and $F^{-1}\big(\Pi\big|\psi_n(x,y,t)\big)$ represents the inverse cumulative distribution function for a probability $\Pi \in \left\{1-\frac{\alpha}{2}, \frac{\alpha}{2}\right\}$. The empirical cumulative distribution function for each output is obtained from the corresponding cumulative frequency histogram. To calculate the histogram of the output, the range of the output data is divided into bins of equal widths, and the number of data points that fall into each bin is counted. The cumulative probability at point p is then approximated by determining the cumulative summation of the sample points in each of the bins between (and including) the first bin and the bin that encompasses p. Subsequently, this value is divided by the total number of sample points P.

Parametric uncertainty in the uncertain parameters $\boldsymbol{\Phi}$ can be propagated through a system model using direct sampling methods such as MC sampling, or through the use of low-order mathematical models such as PSE and PCE. The PSE approach is derived from Taylor series, and it relies on the sensitivity of the model outputs with respect to the uncertain variables in order to construct low-order approximations.[25,120] Alternatively, PCE targets the relationship between the desired model outputs $\boldsymbol{\psi}$ and the uncertain parameters $\boldsymbol{\Phi}$ using orthogonal stochastic polynomial expansions.[120,122,123,141] The objective of this chapter is to discuss and compare PSE and PCE for uncertainty propagation in a multiscale catalytic flow reactor

system. Sections 4.1 and 4.2 will discuss the PSE and PCE algorithms respectively that were implemented in this work. Although these modelling approaches have been previously implemented in the literature,[83,120,125,126] they have been adapted to form a new algorithmic framework that practically quantifies spatially-varying and transiently-varying uncertainty for catalytic multiscale systems. Note that the effects of transient uncertainty are not explored in this work. The PSE and PCE methodologies are subsequently validated and contrasted in Section 4.3 in order to assess the accuracy and the efficiency of each approach when performing uncertainty analysis on the multiscale catalytic reactor system considered in this work.

4.1 Uncertainty Propagation using Power Series Expansions

The PSE approach is a Taylor series-based method that calculates the deviation from the predicted model output due to uncertainty. The PSE formulation for the nth system output can be expressed as follows:

$$\psi_n(x,y,t) = \hat{\psi}_n(x,y,t) + \sum_{\eta=1}^{\infty} \frac{(\boldsymbol{\Phi}-\hat{\boldsymbol{\Phi}})^{\eta}}{\eta!} \left(\frac{\delta^{\eta}\psi_n(x,y,t)}{\delta \boldsymbol{\Phi}^{\eta}}\right)_{\boldsymbol{\Phi}=\hat{\boldsymbol{\Phi}}} \tag{4-2}$$

where η denotes the order of the PSE term and $\hat{\boldsymbol{\Phi}}$ denotes the nominal values of the uncertain parameters $\boldsymbol{\Phi}$. This equation illustrates the dependence of PSE on the sensitivities of the model outputs with respect to the uncertain parameters. The use of sensitivities is a common practice as it requires minimal sampling from the multiscale model and therefore the computational cost for PSE remains reasonable regardless of the model complexity. Needless to say, the computational cost for PSE depends on the number of uncertain parameters and the number of terms considered in the PSE, which both require the calculation of additional sensitivities in order to construct representative low-order models.[132,142] First-order PSEs can be used to provide analytical expressions for the variability in $\psi_n(x,y,t)$ at low computational cost, whereas higher order PSEs require MC sampling to determine the PDFs for the system outputs. In addition, higher-order series expansions result in further increased computational costs due to the computation of the higher-order sensitivity terms. However, adding more terms to the PSE can improve the accuracy of the PSE-based approximation[83,120,127] and the number of terms required for reasonable accuracy depends on the degree of nonlinearity of the system model. The order of the PSE required to approximate the model must therefore be determined offline through direct comparison to the primary model.

In heterogeneous multiscale systems, a single uncertainty analysis is not sufficient to explicitly describe the effects of uncertainty throughout the spatial domain of the model. PSEs must subsequently be constructed at multiple discrete spatial points within the reactor to establish a comprehensive understanding

of the effects of uncertainty. Accordingly, a step-by-step spatially-varying PSE-based uncertainty propagation algorithm for spatially heterogeneous multiscale systems has been used in this study and is as follows:

1. Discretize the spatial and temporal domains into *I* axial points, *J* radial points, and *K* temporal points corresponding to points $(x_{ud,i}, y_{ud,j}, t_{ud,k})$ at which different uncertainty distributions will be applied to each uncertain parameter considered in $\boldsymbol{\Phi}$. To evaluate the system outputs $\boldsymbol{\psi}$ at various points in space and time within the reactor, similarly discretize the reactor interior into *U* axial points, *V* radial points, and *W* temporal points corresponding to the locations $(x_{ov,u}, y_{ov,v}, t_{ov,w})$ where the process output variation is to be assessed. Note that the discretization points $(x_{ov,u}, y_{ov,v}, t_{ov,w})$ at which the output variation is to be assessed are independent from the discretization points $(x_{ud,i}, y_{ud,j}, t_{ud,k})$ at which unique uncertainty descriptions are applied to the uncertain parameters; that is, it is not necessary to sample the output variation at every uncertainty distribution discretization point and vice versa. Thus, different indexes are required to differentiate between $(x_{ov,u}, y_{ov,v}, t_{ov,w})$ and $(x_{ud,i}, y_{ud,j}, t_{ud,k})$.
2. Define the vector of system outputs $\boldsymbol{\psi}(x_{ov,u}, y_{ov,v}, t_{ov,w}) = [\psi_1(x_{ov,u}, y_{ov,v}, t_{ov,w}), \dots, \psi_n(x_{ov,u}, y_{ov,v}, t_{ov,w}), \dots, \psi_N(x_{ov,u}, y_{ov,v}, t_{ov,w})] \in \mathbb{R}^{1\times N}$ and the vector of nominal system outputs $\hat{\boldsymbol{\psi}}(x_{ov,u}, y_{ov,v}, t_{ov,w}) = [\hat{\psi}_1(x_{ov,u}, y_{ov,v}, t_{ov,w}), \dots, \hat{\psi}_n(x_{ov,u}, y_{ov,v}, t_{ov,w}), \dots, \hat{\psi}_N(x_{ov,u}, y_{ov,v}, t_{ov,w})] \in \mathbb{R}^{1\times N}$ at each discrete point $(x_{ov,u}, y_{ov,v}, t_{ov,w})$. Similarly, define the matrix-block for the uncertain parameters $\boldsymbol{\Phi} = [\boldsymbol{\phi}_1, \dots, \boldsymbol{\phi}_m, \dots, \boldsymbol{\phi}_M] \in \mathbb{R}^{1\times M}$, where the elements of the 3D matrix $\boldsymbol{\phi}_m \in \mathbb{R}^{I\times J\times K}$ denote the values for the mth uncertain parameter at each uncertainty description point $(x_{ud,i}, y_{ud,j}, t_{ud,k})$, i.e.:

$$\boldsymbol{\phi_m} = \{\phi_m(x_{ud,i}, y_{ud,j}, t_{ud,k}) | i = 1, 2, \dots I;\ j = 1, 2, \dots J;\ k = 1, 2, \dots K\} \tag{4-3}$$

Similarly, let the matrix-block $\hat{\boldsymbol{\Phi}} = [\hat{\boldsymbol{\phi}}_1, \dots, \hat{\boldsymbol{\phi}}_m, \dots, \hat{\boldsymbol{\phi}}_M] \in \mathbb{R}^{1\times M}$ represent the nominal values of the uncertain parameters, where the elements of the 3D matrix $\hat{\boldsymbol{\phi}}_m \in \mathbb{R}^{I\times J\times K}$ denote the nominal values for the mth uncertain parameter at each uncertainty description point $(x_{ud,i}, y_{ud,j}, t_{ud,k})$.
3. Define the PDF $f_{PD,\phi_m(x_{ud,i}, y_{ud,j}, t_{ud,k})}$ for each uncertain parameter ϕ_m at each point $(x_{ud,i}, y_{ud,j}, t_{ud,k})$ according to:

$$\phi_m\left(x_{ud,i}, y_{ud,j}, t_{ud,k}\right) \in f_{PD,\phi_m\left(x_{ud,i}, y_{ud,j}, t_{ud,k}\right)}\left(\mu\left(\phi_m\left(x_{ud,i}, y_{ud,j}, t_{ud,k}\right)\right), \sigma^2\left(\phi_m\left(x_{ud,i}, y_{ud,j}, t_{ud,k}\right)\right)\right) \quad (4\text{-}4)$$

Note that different types of probability distributions can be implemented to describe the uncertainty in the input parameters. These PDFs can be constructed from data gathered from laboratory or computational experiments.

4. Determine the sensitivities of each system output ψ_n at every discretized point $\left(x_{ov,u}, y_{ov,v}, t_{ov,w}\right)$ with respect to the uncertain parameters $\mathbf{\Phi}$. The first and second-order sensitivities can be obtained as follows:

$$\mathbf{J}\left(x_{ov,u}, y_{ov,v}, t_{ov,w}\right) = \left(\frac{\partial \psi_n\left(x_{ov,u}, y_{ov,v}, t_{ov,w}\right)}{\partial \mathbf{\Phi}}\right)_{\mathbf{\Phi}=\hat{\mathbf{\Phi}}} \quad (4\text{-}5)$$

$$\mathbf{M}\left(x_{ov,u}, y_{ov,v}, t_{ov,w}\right) = \left(\frac{\partial^2 \psi_n\left(x_{ov,u}, y_{ov,v}, t_{ov,w}\right)}{\partial \mathbf{\Phi}^2}\right)_{\mathbf{\Phi}=\hat{\mathbf{\Phi}}} \quad (4\text{-}6)$$

5. Build a PSE model for each system output, $\psi_n\left(x_{ov,u}, y_{ov,v}, t_{ov,w}\right)$, using the sensitivities calculated from the previous step, i.e.

$$\psi_n\left(x_{ov,u}, y_{ov,v}, t_{ov,w}\right) = \hat{\psi}_n\left(x_{ov,u}, y_{ov,v}, t_{ov,w}\right) + \mathbf{J}\left(x_{ov,u}, y_{ov,v}, t_{ov,w}\right)\left(\mathbf{\Phi} - \hat{\mathbf{\Phi}}\right) + \frac{1}{2}\left(\mathbf{\Phi} - \hat{\mathbf{\Phi}}\right)^T \mathbf{M}\left(x_{ov,u}, y_{ov,v}, t_{ov,w}\right)\left(\mathbf{\Phi} - \hat{\mathbf{\Phi}}\right) + \cdots \quad (4\text{-}7)$$

Note that higher order terms can be added to the PSE model provided that their corresponding sensitivities have been computed in Step 4.

6. Propagate the parametric uncertainty through the PSE models using MC sampling to determine the system output variability at each discretized point, $\psi_n\left(x_{ov,u}, y_{ov,v}, t_{ov,w}\right)$ using the expansion shown in Eq. (4-7). The MC sample points are generated from the PDF $f_{PD,\mathbf{\Phi}}$ for the matrix-block of uncertain parameters, $\mathbf{\Phi}$. This will result in a PDF, $f_{PD,\mathbf{\Psi}\left(x_{ov,u}, y_{ov,v}, t_{ov,w}\right)}$, that represents the effect of uncertain parameters on the system output at the point $\left(x_{ov,u}, y_{ov,v}, t_{ov,w}\right)$. Alternatively, if the PSE is first-order ($\eta = 1$), then the PDF for the variability in ψ_n can be directly calculated as follows:

$$f_{PD,\psi_n} = \frac{1}{\sqrt{2\pi\sigma^2(\psi_n)}} e^{-\frac{\left(\psi_n - \hat{\psi}_n\right)^2}{2\sigma^2(\psi_n)}} \quad (4\text{-}8)$$

where $\sigma^2(\psi_n) = J\sigma_{\mathbf{\Phi}}^2 J^T$.

7. Compute the desirable statistics on $\psi_n(x_{ov,u}, y_{ov,v}, t_{ov,w})$, i.e., the mean $\mu\left(\psi_n(x_{ov,u}, y_{ov,v}, t_{ov,w})\right)$, the variance $\sigma^2\left(\psi_n(x_{ov,u}, y_{ov,v}, t_{ov,w})\right)$, and the probabilistic bounds $\psi_n^{up}(x_{ov,u}, y_{ov,v}, t_{ov,w})$ and $\psi_n^{lw}(x_{ov,u}, y_{ov,v}, t_{ov,w})$. The probabilistic bounds can be determined at a specified confidence level, α, according to Eq. (4-1). This step should be repeated for each output variable ψ_n at each output discretization point $(x_{ov,u}, y_{ov,v}, t_{ov,w})$.

The multiscale model used in this work is stochastic; therefore, stochastic sensitivity is required to compute the gradients in the PSE approximations. As discussed in Chapter 3, the stochastic noise can be reduced by taking the average over multiple model simulations with the same parameter values and using the averaged responses to calculate the sensitivities. A larger number of sample points for each average leads to more accurate results at the cost of additional computational time. This trade-off was addressed within this work by taking the average over eight simulations of the multiscale model performed in parallel, which was determined to provide reasonable accurate results at acceptable computational costs.

4.2 Uncertainty Propagation using Polynomial Chaos Expansions

The PCE uncertainty propagation methodology uses orthogonal basis functions to approximate the relationship between the uncertain parameters $\mathbf{\Phi}$ and the system output ψ_n, as follows:[120,122,123,141]

$$\psi_n(x, y, t) = \sum_{\eta=0}^{\infty} \boldsymbol{a}_\eta(x, y, t)\boldsymbol{\beta}_\eta(\Xi) \tag{4-9}$$

where $\boldsymbol{a}_\eta$ denotes the ηth order PCE coefficients, $\boldsymbol{\beta}_\eta$ represents the ηth order orthogonal polynomial basis functions that are defined as a function of Ξ, which denotes a set of independent random parameters from standard distributions that vary as a function of the uncertain parameters $\mathbf{\Phi}$. The orthogonal basis functions $\boldsymbol{\beta}(\Xi)$ comply with the following condition:[123]

$$\int \boldsymbol{\beta}_i(\Xi)\boldsymbol{\beta}_j(\Xi)P(\Xi)d\Xi = \delta_{i,j}\left\|\boldsymbol{\beta}_\eta\right\|^2 \tag{4-10}$$

where $P(\boldsymbol{\Xi})$ denotes the joint density of $\boldsymbol{\Xi}$ and $\delta_{i,j}$ is the Kronecker delta. Note that the PCE coefficients $\mathbf{a}_\eta$ are dependent on the system's spatial and temporal domains (x, y, and t). The spatially-varying PCE method implemented in this work to propagate parametric uncertainty through the multiscale catalytic flow reactor model can be expressed by the following step-by-step algorithm:

1. Perform Steps 1 to 3 from the PSE algorithm presented in the previous section.
2. Define $\boldsymbol{\Xi} = [\boldsymbol{\xi}_1, \dots, \boldsymbol{\xi}_m, \dots, \boldsymbol{\xi}_M] \in \mathbb{R}^{1\times M}$ as the uncorrelated standard random variables where the elements of 3D matrix $\boldsymbol{\xi}_m \in \mathbb{R}^{I\times J\times K}$ denote the values for the mth parameter at each uncertainty description point $\left(x_{ud,i}, y_{ud,j}, t_{ud,k}\right)$, i.e.

$$\boldsymbol{\xi_m} = \left\{\xi_m\left(x_{ud,i}, y_{ud,j}, t_{ud,k}\right) \middle| i = 1, 2, \dots I;\ j = 1, 2, \dots J;\ k = 1, 2, \dots K\right\} \tag{4-11}$$

   As shown in Eq. (4-9), $\boldsymbol{\Xi}$ is a requirement for the PCE implementation since the orthogonal polynomial basis functions $\boldsymbol{\beta}$ require independent random variables generated from standard distributions as inputs.[122,123] The values of $\boldsymbol{\Xi}$ are a function of $\boldsymbol{\Phi}$ and can be determined by transforming $\boldsymbol{\Phi}$ such that $f_{PD,\boldsymbol{\Xi}}$ has standard properties.[122] For example, if the uncertain parameters $\boldsymbol{\Phi}$ are independent and normally distributed, which is a typical assumption made in uncertainty quantification, then the PDFs of the standard random variables $\boldsymbol{\Xi}$ ($f_{PD,\boldsymbol{\Xi}}$) will have a normal distribution with mean $\mu = 0$ and variance $\sigma^2 = 1$.
3. Select a hypergeometric polynomial $\boldsymbol{\beta}(\boldsymbol{\Xi})$ to use as an orthogonal basis for the PCE model depending on the distribution of $f_{PD,\boldsymbol{\Xi}}$. The Askey scheme of stochastic polynomials provide an ideal choice of polynomial bases since the weight functions of Askey polynomials are orthogonal to the density functions for most standard probability distributions.[122] For example, the recommended polynomial basis for multivariate Gaussian uncertainty distributions are the Hermite polynomials, a subset of the Askey scheme, which are expressed as follows:[122]

$$He_\eta(\boldsymbol{\Xi}) = (-1)^\eta e^{\boldsymbol{\Xi}'\boldsymbol{\Xi}/2}\frac{\delta^\eta}{\delta\boldsymbol{\Xi}^\eta}e^{-\boldsymbol{\Xi}'\boldsymbol{\Xi}/2} \tag{4-12}$$

   The first four Hermite polynomials are as follows:

$$He_0(\boldsymbol{\Xi}) = 1;\ He_1(\boldsymbol{\Xi}) = \boldsymbol{\Xi};\ He_2(\boldsymbol{\Xi}) = \boldsymbol{\Xi}^2 - 1;\ He_3(\boldsymbol{\Xi}) = \boldsymbol{\Xi}^3 - 3\boldsymbol{\Xi} \tag{4-13}$$

The complete Hermite-based PCE formulation takes the following form:

$$\psi_n(x_{ov,u}, y_{ov,v}, t_{ov,w}) = a_0(x_{ov,u}, y_{ov,v}, t_{ov,w}) + \sum_{i=1}^{I}\sum_{j=1}^{J}\sum_{k=1}^{K}\sum_{m=1}^{M}\Big[a_{1,m}(x_{ov,u}, y_{ov,v}, t_{ov,w})\xi_m(x_{ud,i}, y_{ud,j}, t_{ud,k}) + a_{2,m,m}(x_{ov,u}, y_{ov,v}, t_{ov,w})\left(\xi_m(x_{ud,i}, y_{ud,j}, t_{ud,k})^2 - 1\right) + \sum_{l=1}^{m-1} a_{2,l,m}(x_{ov,u}, y_{ov,v}, t_{ov,w})\xi_m(x_{ud,i}, y_{ud,j}, t_{ud,k})\xi_l(x_{ud,i}, y_{ud,j}, t_{ud,k})\Big] + \cdots \quad (4\text{-}14)$$

4. Determine the PCE coefficients $\boldsymbol{a}_\eta(x_{ov,u}, y_{ov,v}, t_{ov,w})$. This can be accomplished through intrusive techniques that directly modify the source code such as Galerkin projection,[121] or non-invasive approaches that require sampling the primary model such as the least-squares approximation and non-intrusive spectral projection.[122,123] The number of sample points required for non-intrusive PCE is dependent on the number of uncertain parameters $\boldsymbol{\Phi}$ and the number of discretized uncertainty description points $(x_{ud,i}, y_{ud,j}, t_{ud,k})$. Thus, more sample points are required to accurately determine $\boldsymbol{a}_\eta(x_{ov,u}, y_{ov,v}, t_{ov,w})$ when larger numbers of uncertain parameters and uncertainty description points are considered. Note that the intrusive approaches require direct modification of constitute equations and therefore are only applicable for closed-form systems. Ergo, non-invasive techniques are required to determine the PCE coefficients for process models that lack a closed-form, such as the multiscale catalytic flow reactor considered in this work. Also note that a PCE model with a set of coefficients $\boldsymbol{a}_\eta(x_{ov,u}, y_{ov,v}, t_{ov,w})$ can only capture the output variability for a single output variable ψ_n at a single point $(x_{ov,u}, y_{ov,v}, t_{ov,w})$. Consequently, unique independent PCE models must be determined for each output $\boldsymbol{\psi}$ at each output analysis point $(x_{ov,u}, y_{ov,v}, t_{ov,w})$.
5. Propagate the parametric uncertainty through the PCE models using MC sampling to determine the variability in each output $\psi_n(x_{ov,u}, y_{ov,v}, t_{ov,w})$. MC sampling is used to determine random values in the uncorrelated standard parameters $\boldsymbol{\Xi}$, which are substituted into the PCE model to determine $\psi_n(x_{ov,u}, y_{ov,v}, t_{ov,w})$.
6. Compute the mean $\mu\left(\psi_n(x_{ov,u}, y_{ov,v}, t_{ov,w})\right)$, the variance $\sigma^2\left(\psi_n(x_{ov,u}, y_{ov,v}, t_{ov,w})\right)$, the probabilistic bounds $\psi_n^{up}(x_{ov,u}, y_{ov,v}, t_{ov,w})$ and $\psi_n^{lw}(x_{ov,u}, y_{ov,v}, t_{ov,w})$, and other desirable statistics from the PCE outputs $\psi_n(x_{ov,u}, y_{ov,v}, t_{ov,w})$. The probabilistic bounds can be determined at a specified confidence level α as demonstrated in Eq. (4-1). This step should be repeated for each output variable ψ_n at each output discretization point $(x_{ov,u}, y_{ov,v}, t_{ov,w})$.

The computational efficiency of non-intrusive PCE is limited by the number of uncertain parameters $\boldsymbol{\phi}_m$, the number of discretized uncertainty description points $\left(x_{ud,i}, y_{ud,j}, t_{ud,k}\right)$, the PCE order η, and the number of sample points used to determine the PCE coefficients. Lower-order PCE models require fewer PCE coefficients $\boldsymbol{a}_\eta$ compared to higher-order PCE models and therefore have significantly reduced computational costs, however decreasing η can significantly impede the accuracy of the PCE model and introduce significant error. Similarly, decreasing the number of sample points used in non-intrusive PCE reduces the computational cost, at the cost of additional error in the PCE models. The optimal PCE order and the optimal number of sample points can be determined by increasing η and the number of points respectively until no further improvement in the model accuracy is achieved.

4.3 Comparison of Polynomial Chaos Expansions and Power Series Expansions

In order to compare the performance of PSE and PCE, parametric uncertainty was propagated through the primary multiscale catalytic flow reactor model and evaluated in the concentration of the product species C at the reactor outlet, $C_{C,out}(t)$. For this analysis, the reactor model was subjected to step changes in temperature. The reactor temperature was initialized at T = 460K, and the reactor species concentrations were allowed to evolve for five seconds at this temperature. Subsequently, the reactor was subjected to 20K step changes every five seconds for a total reaction time of t_{final} = 35s, according to the temperature profile presented in Figure 4-1a. Uncertainty was considered for a single kinetic parameter (the activation energy of desorption for species A, $E_{d,A}$) and a single reactor design parameter (the pore radius, ρ). The uncertainty in the activation energy, $E_{d,A}$, was assumed to vary as a function of space due to catalyst deactivation. To account for this behaviour, different uncertainty descriptions were applied to $E_{d,A}$ at each tooth considered in the gap-tooth model. For this analysis, the reactor was sub-divided into seven teeth ($n_{teeth} = 7$), and therefore uncertainty analysis was performed with respect to eight independent parameters consisting of the radius, ρ, and seven different uncertainty descriptions of the desorption activation energy of species A at each tooth ($I = 7$). Note that the uncertainty in $E_{d,A}$ cannot vary radially as this parameter only affects phenomena that occur along the catalyst surface; thus, $J = 1$. The uncertainty in each parameter was assumed to be normally-distributed for simplicity, with a mean and variance defined as follows:

$$\left[\mu(\rho), \mu(E_{d,A})\right] = [10\ \text{nm}, 95\ \text{kJ/mol}]$$

$$\left[\sigma^2(\rho), \sigma^2\left(E_{d,A}(0,\rho)\right), \ldots, \sigma^2\left(E_{d,A}(x_{ud,i},\rho)\right), \ldots, \sigma^2\left(E_{d,A}(L,\rho)\right)\right] =$$

$$[4\ \text{nm}^2, 3.61\,\frac{\text{kJ}^2}{\text{mol}^2}, 8.1225\,\frac{\text{kJ}^2}{\text{mol}^2}, 14.44\,\frac{\text{kJ}^2}{\text{mol}^2}, 22.5625\,\frac{\text{kJ}^2}{\text{mol}^2}, 14.44\,\frac{\text{kJ}^2}{\text{mol}^2}, 8.1225\,\frac{\text{kJ}^2}{\text{mol}^2}, 3.61\,\frac{\text{kJ}^2}{\text{mol}^2}] \quad (4\text{-}15)$$

The accuracies of PSE and PCE were determined by direct comparison of both methods to the output probability distributions determined via direct MC sampling of the multiscale reactor model. The comparison was performed using a second-order PSE expansion with sensitivities calculated using centered finite differences. Conversely, the PCE formulation was determined using second-order Hermite polynomials with 45 model coefficients computed using the least-squares method over 75 randomly generated sample points. The number of model coefficients is consistent with the number of terms for a second-order PCE applied to a system with eight uncertain parameters. Additionally, the number of sample points for the PCE formulation was determined *a priori* as the lowest number of sample points necessary to achieve sufficient accuracy, as increasing the number of sample points does not significantly improve the predictions. The comparison was performed at each discretized point in time t at the center of the reactor outlet $(x = L, y = 0)$ for the product concentration $C_{C,out}(t)$. The resulting distributions were used to determine upper and lower bounds, i.e. $C_{C,out}^{up}(t)$ and $C_{C,out}^{lw}(t)$, at a confidence interval of $\alpha = 1\%$ for each series expansion. These bounds were compared against those calculated from probability distributions obtained from 5,000 MC realizations in the uncertain parameters. The number of MC sample points was sufficient to accurately capture the system behaviour.

The results for both PSE and PCE are illustrated in Figures 4-1b, c, and d. In Figure 4-1b, the upper and lower bounds obtained via PSE and PCE are compared to the transient concentration profiles obtained from MC sampling as well as the nominal transient concentration profile. In addition, Figure 4-1c compares the PDFs obtained from each sampling method at the end of the reaction process (t_{final} = 35s), and Figure 4-1d compares the temporal evolution of the statistical parameters (probabilistic bounds and expected values) for each sampling method. Furthermore, Table 4-1 compares the computational cost and the statistical parameters for each model expansion with respect to MC sampling after 8s, 23s, and 33s. These times were selected because they correspond to the reactor behaviour at steady state for each of the implemented temperatures (T = 480K, T = 440K, and T = 460K, respectively). Table 4-1 additionally compares the absolute errors and percentage errors between the statistical parameters calculated via PSE/PCE and the statistical parameters of the MC sampling results. For the sake of comparison, the percentage errors were calculated by normalizing the absolute errors by the difference in the probabilistic bounds, as follows:

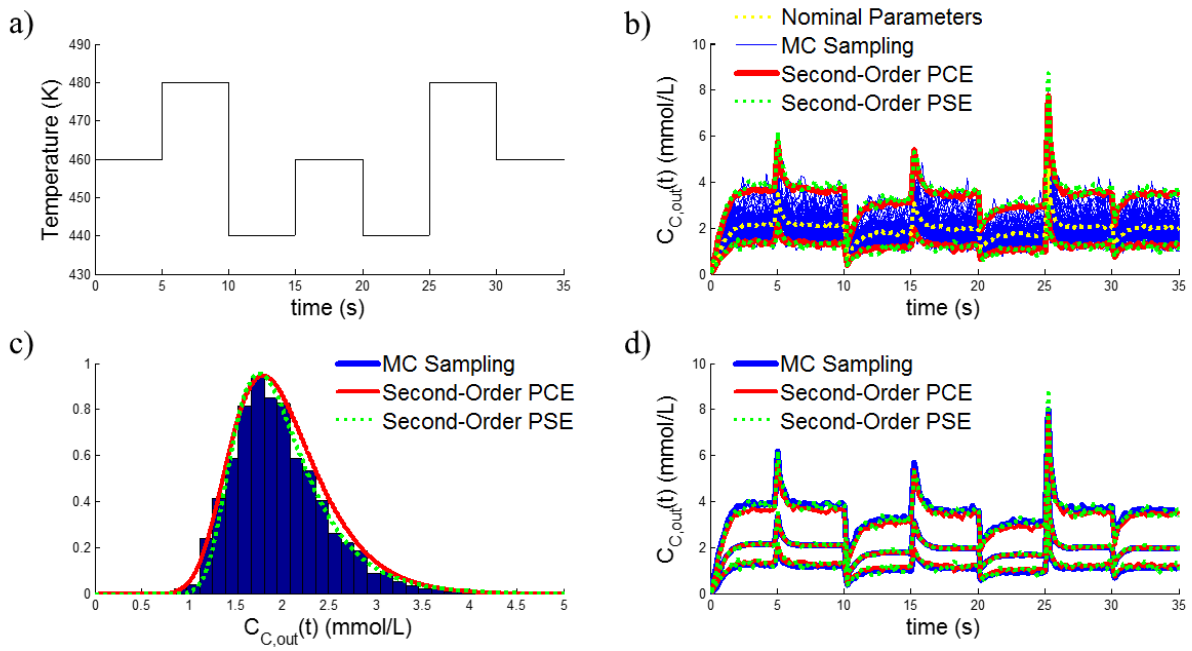

Figure 4-1. Comparison of PSE and PCE on the multiscale catalytic reactor model: (a) Dynamic temperature profile; (b) Outlet concentration response; (c) PDF: Outlet concentration; (d) Expected value and bounds evaluated at a 2% confidence level.

$$\% \text{ Error} = \frac{X_{Expansion}(L,0,t) - X_{MC}(L,0,t)}{C^{up}_{s,out,MC}(t) - C^{lw}_{s,out,MC}(t)} \tag{4-16}$$

where $X_{Expansion}(L,0,t)$ and $X_{MC}(L,0,t)$ denote the value of statistical parameter X, which denotes the expected value and probabilistic bounds as determined via PSE/PCE expansions and MC sampling respectively. In addition, $C^{up}_{s,out,MC}(t)$ and $C^{lw}_{s,out,MC}(t)$ denote the values for the upper and lower bounds for species s determined from the MC sampling results at a time t and at the reactor output.

As shown in Figure 4-1b, parametric uncertainty results in significant variations in the reactor behaviour that cannot be neglected without severe loss of performance. Specifically, the upper and lower probabilistic bounds indicate variations as high as 80% and 44% respectively from the expected values of the reactor outlet product concentrations. Table 4-1 illustrates that the errors in both PSE and PCE remain below 200 μmol/L (10%), indicating that both expansions provide reasonable representations of the effects of parametric uncertainty on the outlet product concentration of the reactor. According to Figure 4-1b, the probabilistic bounds derived from both PSE and PCE are able to adequately bound the MC simulation results within the desired confidence level, with an average of one violation per 100 MC sample points at any one time. Additionally, Figure 4-1c demonstrates that both PCE and PSE are able to capture the shape

Table 4-1. Statistics and computational costs of the reactor outlet product concentration at times t = 8s, t = 23s, and t = 33s

		MC Sampling	PCE	PSE
Total CPU Time (s)		67 h	21 h	29 h
Outlet Product Concentration, t=8s, T=480 K (mmol/L)	$\mu(C_{C,out}(8s))$	2.104136	2.111071 (6.935 μmol/L, 0.262% Error)	2.142147 (38.011 μmol/L, 1.435% Error)
	$C_{C,out}^{up}(8s)$	3.828483	3.788037 (40.446 μmol/L, 1.527% Error)	3.643543 (184.94 μmol/L, 6.981% Error)
	$C_{C,out}^{lw}(8s)$	1.179294	1.171071 (8.223 μmol/L, 0.310% Error)	1.374553 (195.26 μmol/L, 7.371% Error)
Outlet Product Concentration, t=23s, T=440 K (mmol/L)	$\mu(C_{C,out}(23s))$	1.699618	1.7299 (30.282 μmol/L, 1.426% Error)	1.725425 (25.807 μmol/L, 1.215% Error)
	$C_{C,out}^{up}(23s)$	3.055214	3.194008 (138.79 μmol/L, 6.536% Error)	3.107126 (51.912 μmol/L, 2.445% Error)
	$C_{C,out}^{lw}(23s)$	0.93184	0.951576 (19.736 μmol/L, 0.929% Error)	1.033342 (101.502 μmol/L, 4.780% Error)
Outlet Product Concentration, t=33s, T=460 K (mmol/L)	$\mu(C_{C,out}(33s))$	1.998262	1.974835 (23.427 μmol/L, 0.945% Error)	2.009483 (11.221 μmol/L, 0.453% Error)
	$C_{C,out}^{up}(33s)$	3.637066	3.438921 (198.15 μmol/L, 7.995% Error)	3.502315 (134.75 μmol/L, 5.437% Error)
	$C_{C,out}^{lw}(33s)$	1.15872	1.187462 (28.742 μmol/L, 1.160% Error)	1.217854 (59.134 μmol/L, 2.386% Error)

of the outlet distribution, whereas Figure 4-1d illustrates that both expansions provide good approximations of the expected value and the probabilistic bounds of the outlet distribution. The results in Table 4-1 show that PSE and PCE provide a 31.3% and 43.3% decrease respectively in the computational cost as compared to MC sampling. At time t = 23s, the PCE results are 81.8 μm (3.9%) more accurate than PSE at capturing the lower bound behaviour, whereas PSE provides a 86.9 μm (4.1%) superior fitting of the upper bound. Similar behaviour is observed at t = 33s, where PCE is 30.4 μm (1.2%) better at capturing the lower bound behaviour and PSE is 63.4 μm (2.6%) better at capturing the upper bound behaviour. At t = 8s, the PCE results are 144.5 μm (5.5%) and 187.0 μm (7.1%) better at approximating the behaviour of the upper and lower bounds respectively as compared to PSE. Overall, these results demonstrate that neither PSE nor PCE is clearly better when it comes to accurately capturing the catalytic model behaviour. On average, PCE provides a better fit than PSE for the multivariate uncertainty distribution implemented as predicted in the literature,[134] but PCE does not provide a significant increase in accuracy over PSE. However, PCE requires fewer sample points to build its model approximation compared to PSE, and therefore incurs lower computational cost.

4.4 Summary

This chapter provided a general overview of the PSE and PCE uncertainty propagation methods and discussed how they could be used to propagate spatially-varying and transiently-varying uncertainty through a multiscale catalytic flow reactor system. Although the algorithms provided are capable of propagating uncertainty that evolves over time, this type of uncertainty description (i.e. time-varying uncertainty) has not been considered in any of the case studies implemented in this work. This chapter additionally compared the accuracy and efficiency of PSE and PCE in the propagation of spatially-varying uncertainty through the transient multiscale reactor model. These results demonstrated that both methods are capable of accurately capturing the variation in the reactor concentrations due to parametric uncertainty, and at significantly lower computational costs as compared to MC sampling. PCE proved to be slightly superior to PSE in terms of accuracy and computational cost. However, since both methods have similar accuracy, both series expansions were used to propagate parametric uncertainty in this work.

Chapter 5
Distributional Uncertainty Analysis and Robust Optimization in a Steady-State Catalytic Flow Reactor*

Catalytic reactors play an important role in a wide variety of chemical engineering applications. This has promoted significant interest in model-based catalyst design and optimization to improve reactor efficiency at minimal cost and resources. The effectiveness of a model-based optimization scheme is dependent on the accuracy and the efficiency of the system model. Since reactor systems are generally operated under continuous conditions,[1,4] they are most efficiently optimized by neglecting the transient reactor behaviour through the implementation of steady-state multiscale modeling approaches. However, these models are subject to uncertainty in the system parameters, which can introduce substantial model-plant mismatch and can lead to significant deviations when performing optimization and process improvement studies. It is therefore necessary to understand the impact of parametric uncertainty on the catalytic reactor behaviour and to account for it within model-based optimization schemes.

Motivated by this, the objective of this chapter is to study the effects of parametric uncertainty on the steady-state behaviour of a single-pore catalytic reactor system. This is accomplished by propagating uncertainty in an increasing number of key system parameters and observing their impact on reactor performance. The catalytic reactor implemented in this study is simulated using a kMC-continuum based steady-state multiscale reactor model as described in Chapter 3. Additionally, PSE expressions are developed to propagate the parametric uncertainty through the multiscale model. These techniques are then used to perform robust optimization on the catalytic reactor system subject to uncertainty in key system parameters.

This chapter is divided as follows. In Section 5.1, uncertainty analysis is performed to evaluate the effects of uncertainty in several key system parameters on the concentration of the product species C along the length of the reactor. For these studies, uncertainty is considered in both the catalyst kinetic parameters and the reactor design parameters such as the pore radius. In Section 5.2, the proposed uncertainty quantification method is embedded within optimization formulations that aim to specify the optimal operating conditions and design parameters, which can improve reactor productivity in the presence of uncertainty.

*The contents of this chapter have been published in the American Institute of Chemical Engineering Journal.[25]

5.1 Uncertainty Analysis

In order to understand the negative impact of model-plant mismatch on the optimization of catalytic reactor systems, it is crucial to first understand how uncertainty in key system parameters affects the behaviour of the steady-state multiscale catalytic reactor. To that extent, the PSE-based algorithm described in Chapter 4 was used to perform uncertainty analysis by propagating key parameter uncertainties through the steady-state multiscale single-pore catalytic reactor model. The following three scenarios were considered in this work: an uncertainty analysis of a reactor with a known catalyst pore size and three uncertain key kinetic parameters, an uncertainty analysis of a reactor where the catalyst pore size was not known with certainty in addition to the three uncertain kinetic parameters, and an extension of the uncertainty analysis to encompass all uncertain model parameters. In all three scenarios, the catalyst surface domain of the multiscale model was coarse-grained into eight teeth (i.e. n_{teeth} = 8) separated by 125nm gaps. Consequently, the effects of uncertainty were analyzed in the species concentrations at eight axial points on the catalyst surface corresponding to the locations of each tooth (located at $\left(x_{ov,u} = x_{tooth}, y_{ov,v} = \rho\right)$, where $U = 8$ and $V = 1$ in the PSE algorithm). Furthermore, the variation in the effects of uncertainty on the fluid concentrations were considered at four equidistant radial points at the reactor outlet with coordinates ($x_{ov,u} = L, y_{ov,u} = y_{ti}$), where $y_{ti} = \{0\text{nm}, 3.33\text{nm}, 6.67\text{nm}, 10\text{nm}\}$, $U = 1$, and $V = 4$ in the PSE algorithm. Probabilistic bounds for each scenario were calculated at a confidence level of $\alpha = 2\%$. The results obtained from these scenarios are discussed in the next sections.

5.1.1 Scenario 1: Uncertainty Analysis on the Catalytic Reactor with Known Pore Size

Uncertainty in key system parameters was propagated to the fluid concentrations inside the catalytic reactor. The key parameters were identified prior to the analysis by performing an offline sensitivity analysis on each model parameter. The sensitivity analysis was conducted by varying each of the multiscale model parameters independently by ±25% and ±50%. The results from this analysis were used to determine the sensitivity of the output concentrations to each of the uncertain parameters. Note that the temperature, the inlet fluid velocity, the length, and the radius of the catalytic pore, i.e. the operating conditions and design parameters, remained constant during this analysis and were set to the nominal values reported in Table 3-1. From this analysis, it was determined that the activation energies of desorption for species A and reaction, i.e. $E_{d,A}$ and E_r, have the largest overall effect on the system. Uncertainty was also applied to the adsorption constant $k_{a,A}$ as it is the key parameter affecting the adsorption rate of species A. The key

uncertain parameters considered in this work were assumed to be normally distributed around the mean values of $\left[\mu\left(k_{a,A}\right), \mu\left(E_{d,A}\right), \mu(E_r)\right] = [1, 95, 57]$ with the following covariance matrix:

$$\sigma^2\left(k_{a,A}, E_{d,A}, E_r\right) = \begin{bmatrix} 0.01 & 0.005 & 0.005 \\ 0.005 & 8.1225 & 1.46205 \\ 0.005 & 1.46205 & 2.9241 \end{bmatrix} \tag{5-1}$$

Figure 5-1 displays the effects of the uncertainty on the output fluid concentrations $C_{s,out}$ for each chemical species, determined via MC sampling through both the primary multiscale reactor model and the second-order PSE. The probabilistic bounds are presented in Table 5-1 alongside the computational times required by each method. Note that for the sake of comparison, the percent errors were calculated using Eq. (4-16). Second-order PSE was chosen based on preliminary simulations using different PSE orders, which revealed that second-order PSE provides suitable results at acceptable computational costs. A total of 2,000 MC sampling points were applied to the primary multiscale model to capture the effects of uncertainty on the multiscale catalytic reactor behaviour. The number of MC simulations was determined by adding sample points to the analysis until the difference in the mean and variance of the PDFs in the outputs remained fairly constant, i.e. below 1% error between subsequent simulation runs.

As shown in Figure 5-1, uncertainty in these kinetic model parameters results in substantial variability in the concentrations. This is especially apparent in product C, where the probabilistic bounds show that the concentration can deviate from 45% to 65% of its predicted mean value, as shown in Table 5-1. Furthermore, Table 5-1 illustrates that the second-order PSE approximation can accurately describe the

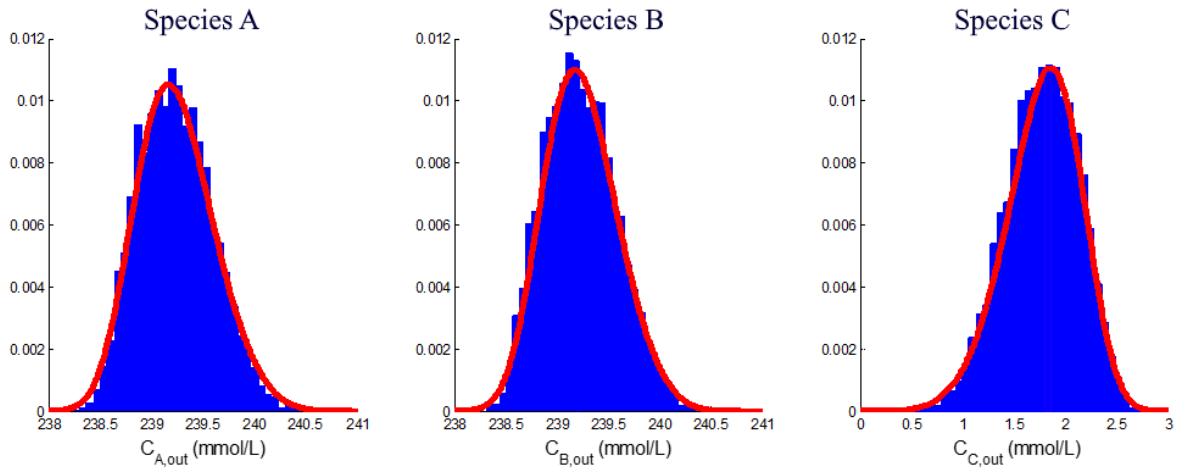

Figure 5-1. PDFs of the steady state output concentrations $C_{s,out}$ generated by MC sampling through the primary multiscale model (blue) and second-order PSE (red).

uncertainty propagation through the single-pore catalytic reactor model using only 11% of the computational cost required by the MC sampling method when applied to the primary multiscale model. Figure 5-2a shows the concentration PDFs for each chemical species at various radial distances across the reactor outlet ($C_s(L, y_{ti})$), which were determined using second-order PSE. This figure reveals that the concentrations do not significantly change along the reactor's radial domain. As a result, for brevity, the uncertainty propagation in the radial direction is not considered in the remainder of this work. Additionally, Figure 5-2b shows the concentration PDFs of each chemical species at the catalyst surface along the reactor's axial direction, i.e. $C_s(z_{tooth}, \rho)$. As shown in this figure, the uncertainties are propagated in the axial direction, resulting in more variability in the steady state concentrations towards the end of the pore. The propagation of uncertainty implies that the variability in the output concentrations can be reduced by shortening the lengths of the reactor pore. However, this would occur at the expense of reducing the production of species C, and results in decreased reactor productivity.

Table 5-1. Distributional uncertainty analysis, Scenario 1.

Method	**Species**	$C_{s,out}^{lw}$ **(mmol/L)**	$C_{s,out}^{up}$ **(mmol/L)**	**Nominal Concentration (mmol/L)**	**Computational Time (s)**
MC applied to the Primary Multiscale Model	A	238.51	240.17	239.18	10,812
	B	238.52	240.11	239.22	
	C	0.8990	2.4961	1.8022	
MC applied to the Second-Order PSE	A	238.42 (81 μmol/L, 4.87% Error)	240.16 (19 μmol/L, 1.15% Error)	239.18	1,193
	B	238.45 (67 μmol/L, 4.22% Error)	240.09 (13 μmol/L, 0.83% Error)	239.22	
	C	0.9116 (13 μmol/L, 0.79% Error)	2.5689 (73 μmol/L, 4.56% Error)	1.8022	

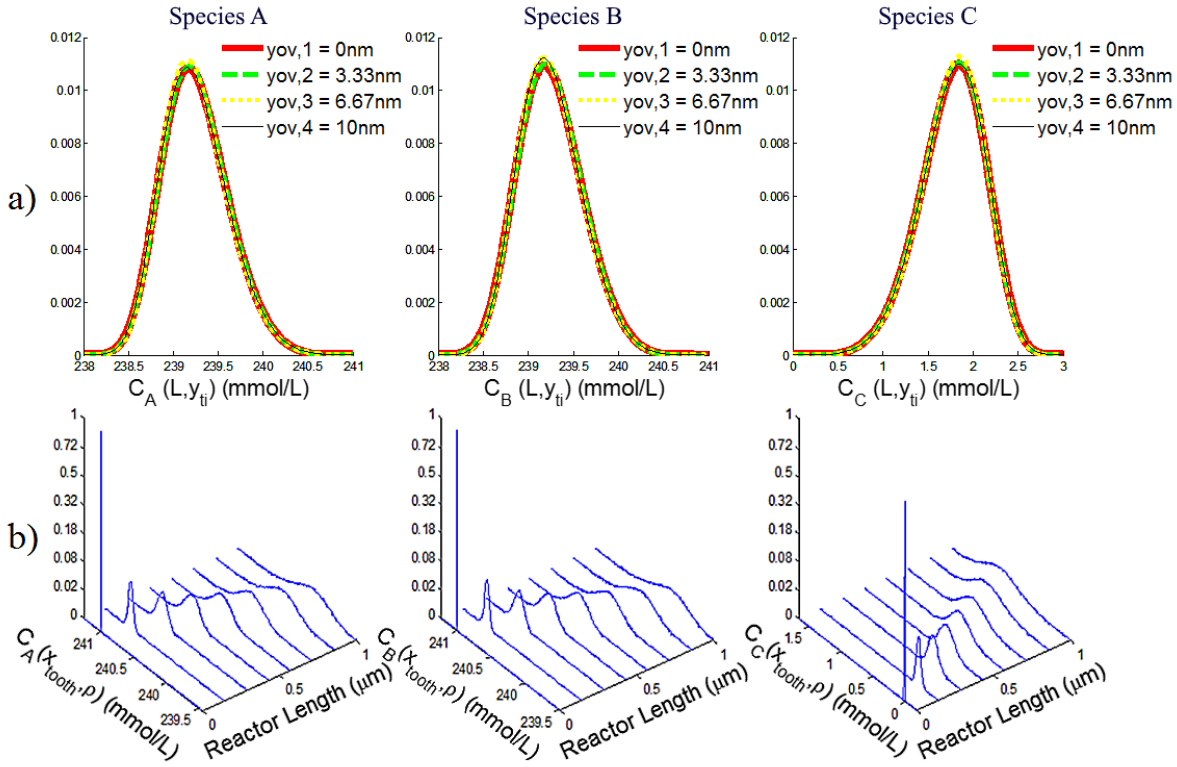

Figure 5-2. PDFs of the concentration for each chemical species (a) along the radial direction at the reactor outlet ($C_s(L, y_{ti})$), and (b) along the axial direction within the reactor interior ($C_s(x_{tooth}, \rho)$).

5.1.2 Scenario 2: Uncertainty Analysis on the Catalytic Reactor with Uncertain Pore Size

The results discussed in the previous subsection assumed that the size of the pore in the single-pore catalytic reactor system is known with certainty. Experimental observations have demonstrated that the shape and size of a nanopore can deviate significantly from their expected value,[143] as the dimensions of a nanopore cannot be precisely determined through experimental observations. Therefore, uncertainty in the pore size should be taken into account when assessing the performance of catalytic flow reactor systems. Taking this into consideration, uncertainty analysis was performed on a catalytic reactor where the pore size was assumed to be uncertain. For this analysis, both the pore radius and the kinetic parameters studied in Scenario 1 (Section 5.1.1) were considered as the set of uncertain parameters. The pore radius was assumed to be normally distributed with a mean value of $\mu(\rho) = 10$ nm and a standard deviation of 20% of the mean value. This assumption was based on a previous study performed on the pore size distribution of nanoporous alumina.[143] The key kinetic parameters were assumed to follow the same normal distribution

Table 5-2. Distributional uncertainty analysis, Scenario 2.

Method	Species	$\mu(C_{s,out})$ (mmol/L)	$C_{s,out}^{lw}$ (mmol/L)	$C_{s,out}^{up}$ (mmol/L)	Nominal Concentration (mmol/L)	Computational Time (s)
MC applied to the Primary Multiscale Model	A	239.16	237.38	240.19	239.18	10,898
	B	239.16	237.43	240.18	239.22	
	C	1.8461	0.8267	3.6036	1.8022	
MC applied to the Second-Order PSE	A	239.17 (9 μmol, 0.36% Error)	237.40 (15 μmol, 0.53% Error)	240.18 (11 μmol, 0.41% Error)	239.18	1,784
	B	239.16 (9 μmol, 0.36% Error)	237.37 (63 μmol, 2.30% Error)	240.16 (24 μmol, 0.89% Error)	239.22	
	C	1.8377 (8 μmol, 0.30% Error)	0.8185 (8 μmol, 0.29% Error)	3.6013 (2 μmol, 0.09% Error)	1.8022	

as described in the previous subsection. Figure 5-3 shows the effect of parameter uncertainties on the output species concentrations $C_{s,out}$ determined using MC sampling applied to the primary multiscale reactor model and the second-order PSE. A comparison of the mean values, probabilistic bounds, nominal model parameter values and computational times is also presented in Table 5-2. Note that for the sake of comparison, the percent errors were calculated using Eq. (4-16). Second-order PSE was chosen based on preliminary simulations using different PSE orders, which revealed that second-order PSE provides suitable results at acceptable computational costs. A total of 2,000 MC sampling points were applied to the primary multiscale model to capture the effects of uncertainty on the multiscale catalytic reactor behaviour. The number of MC simulations was determined by adding sample points to the analysis until the difference in

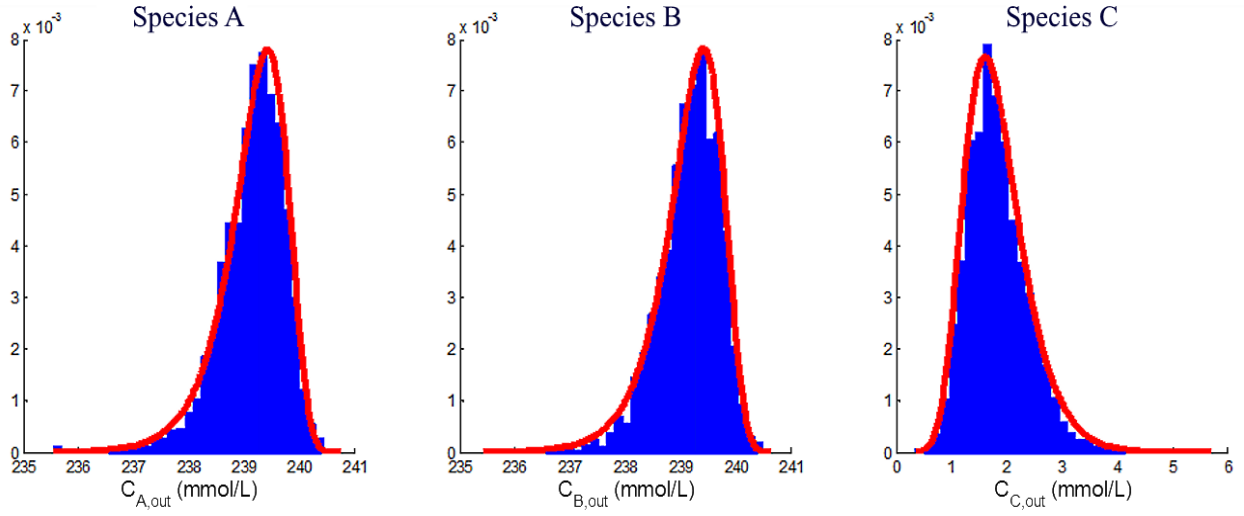

Figure 5-3. PDFs of the output fluid concentrations $C_{s,out}$ using MC applied to the primary multiscale model (blue) and the second-order PSE (red).

the mean and variance of the PDFs in the outputs remained fairly constant, i.e. below 1% error between subsequent simulation runs.

The results show that the second-order PSE is capable of capturing the effect of uncertainties in the pore radius in addition to the key kinetic parameters. The errors in the bounds obtained from the second-order PSE are within $\pm$ 5%, and the PSE-based uncertainty analysis requires 16% of the computational time required using MC sampling applied to the primary multiscale model. Figure 5-4a compares the PDFs of the output concentration $C_{s,out}$ for the cases of known and uncertain pore radius sizes. This figure reveals that uncertainty in the pore radius has a significant effect on the shape and bounds of the steady-state concentration profiles and therefore has a significant effect on the reactor performance. Specifically, when the probabilistic bounds listed in Tables 5-1 and 5-2 are compared, the lower bounds for species A and B decrease by 984 µM while the upper bounds for species C increased by 892 µM when the pore radius is assumed to be uncertain. Figure 5-4b, on the other hand, shows the PDFs of the axial concentrations along the reactor length $C_s(x_{tooth}, \rho)$ for reactors with known and uncertain pore radius size. This figure demonstrates notably wider PDFs throughout the reactor for each chemical species when uncertainty is considered in the pore radius.

5.1.3 Scenario 3: Uncertainty Analysis on the Catalytic Reactor for All Uncertain Parameters

The previous scenarios presented in this work only considered uncertainty in the pore radius and three kinetic parameters. The aim of this scenario is to evaluate the effects of considering additional uncertain

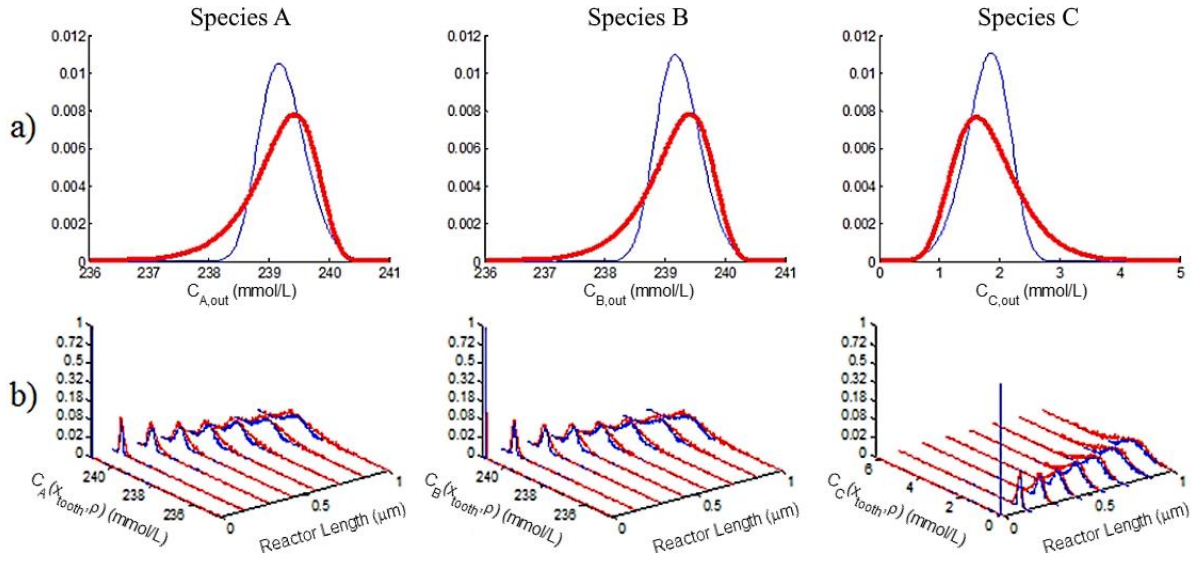

Figure 5-4. PDFs of the (a) output fluid concentrations $C_{s,out}$ and (b) steady state fluid concentrations, $C_s(x_{tooth}, \rho)$, along the reactor axial length; pore radius fixed (blue) and uncertain (red).

parameters into the analysis. Accordingly, two analyses were performed using six and ten uncertain parameters, respectively. For the six parameter case study, uncertainty was considered in the pore radius in addition to the five kinetic parameters which had the largest effect on the concentrations, i.e. $k_{a,A}$, $k_{a,B}$, $E_{d,A}$, $E_{d,B}$, and E_r. The uncertain kinetic parameters were assumed to be normally distributed around their mean values as listed in Table 3-1, with the following covariance matrix:

$$\sigma^2\left(k_{a,A}, k_{a,B}, E_{d,A}, E_{d,B}, E_r, \rho\right) = \begin{bmatrix} 0.01 & 0.005 & 0.005 & 0.005 & 0.005 & 0 \\ 0.005 & 0.01 & 0.005 & 0.005 & 0.005 & 0 \\ 0.005 & 0.005 & 8.1225 & 4.06125 & 1.46205 & 0 \\ 0.005 & 0.005 & 4.06125 & 9 & 1.46205 & 0 \\ 0.005 & 0.005 & 1.46205 & 1.46205 & 2.9241 & 0 \\ 0 & 0 & 0 & 0 & 0 & 4 \times 10^{-18} \end{bmatrix} \quad (5\text{-}2)$$

The ten uncertain parameter case study considered parametric uncertainty in all eight kinetic parameters in addition to uncertainty in the pore radius and the fluid diffusivity, i.e. $k_{a,A}$, $k_{a,B}$, $k_{d,A}$, $k_{d,B}$, $E_{d,A}$, $E_{d,B}$, k_k, E_r, ρ, and D_s. Note that in this case study, the diffusivity of each fluid species was assumed to be the same, such that each diffusivity would be equally affected by parametric uncertainty. All uncertain parameters were assumed to be normally distributed around their nominal values as listed in Table 3-1, with the following covariance matrix:

$$\sigma^2\left(k_{a,A}, k_{a,B}, k_{d,A}, k_{d,B}, E_{d,A}, E_{d,B}, k_k, E_r, \rho, D_s\right) =$$

$$\begin{bmatrix}
0.01 & 0.005 & 0.005 & 0.005 & 0.005 & 0.005 & 0.005 & 0.005 & 0 & 0 \\
0.005 & 0.01 & 0.005 & 0.005 & 0.005 & 0.005 & 0.005 & 0.005 & 0 & 0 \\
0.005 & 0.005 & 1\times10^{20} & 5\times10^{19} & 4.06125 & 4.5 & 2\times10^{12} & 1.46205 & 0 & 0 \\
0.005 & 0.005 & 5\times10^{19} & 1\times10^{20} & 4.06125 & 4.5 & 2\times10^{12} & 1.46205 & 0 & 0 \\
0.005 & 0.005 & 4.06125 & 4.06125 & 8.1225 & 4.06125 & 4.06125 & 1.46205 & 0 & 0 \\
0.005 & 0.005 & 4.5 & 4.5 & 4.06125 & 9 & 4.5 & 1.46205 & 0 & 0 \\
0.005 & 0.005 & 2\times10^{12} & 2\times10^{12} & 4.06125 & 4.5 & 4\times10^{12} & 1.46205 & 0 & 0 \\
0.005 & 0.005 & 1.46205 & 1.46205 & 1.46205 & 1.46205 & 1.46205 & 2.9241 & 0 & 0 \\
0 & 0 & 0 & 0 & 0 & 0 & 0 & 0 & 4\times10^{-18} & 0 \\
0 & 0 & 0 & 0 & 0 & 0 & 0 & 0 & 0 & 1.1236\times10^{-18}
\end{bmatrix} \quad (5\text{-}3)$$

Figure 5-5 shows the effect of parametric uncertainties on the output concentration of species C, $C_{C,out}$, for both the six parameter and ten parameter uncertainty analyses, using MC sampling applied to the primary multiscale model and second-order PSE approximations. The computational costs, mean, variance, and upper and lower bounds evaluated at a 2% confidence interval are additionally presented in Table 5-3. Note that for the sake of comparison, the percent errors for the means and the probabilistic bounds were calculated using Eq. (4-16). Second-order PSE was chosen based on preliminary simulations using different PSE orders, which revealed that second-order PSE provides suitable results at acceptable computational costs. A total of 10,000 and 16,000 MC sampling points were applied to the primary multiscale model to capture the effects of uncertainty in the six uncertain parameter and the ten uncertain parameter cases, respectively. The number of MC simulations was determined by adding sample points to the analysis until the difference in the mean and variance of the PDFs in the outputs remained fairly constant, i.e. below 1% error between subsequent simulation runs.

Table 5-3. Distributional uncertainty analysis, Scenario 3.

Method	Number of Uncertain Parameters	$\mu(C_{C,out})$ (mmol/L)	$\sigma^2(C_{C,out})$ (mmol^2/L^2)	$C_{C,out}^{lw}$ (mmol/L)	$C_{C,out}^{up}$ (mmol/L)	Computational Time (s)
MC applied to the Primary Multiscale Model	6	1.7641	0.3907	0.5972	3.6995	68,623
	10	1.7673	0.3965	0.5817	3.7031	101,672
MC applied to the Second-Order PSE	6	1.7705 (6 μmol/L, 0.21% Error)	0.3865 (4 μmol^2/L^2, 1.06% Error)	0.5861 (11 μmol/L, 0.36% Error)	3.5448 (154 μmol/L, 4.98% Error)	2,156
	10	1.7510 (16 μmol/L, 0.52% Error)	0.3938 (2 μmol^2/L^2, 0.38% Error)	0.5067 (75 μmol/L, 2.40% Error)	3.5667 (136 μmol/L, 4.37% Error)	5,819

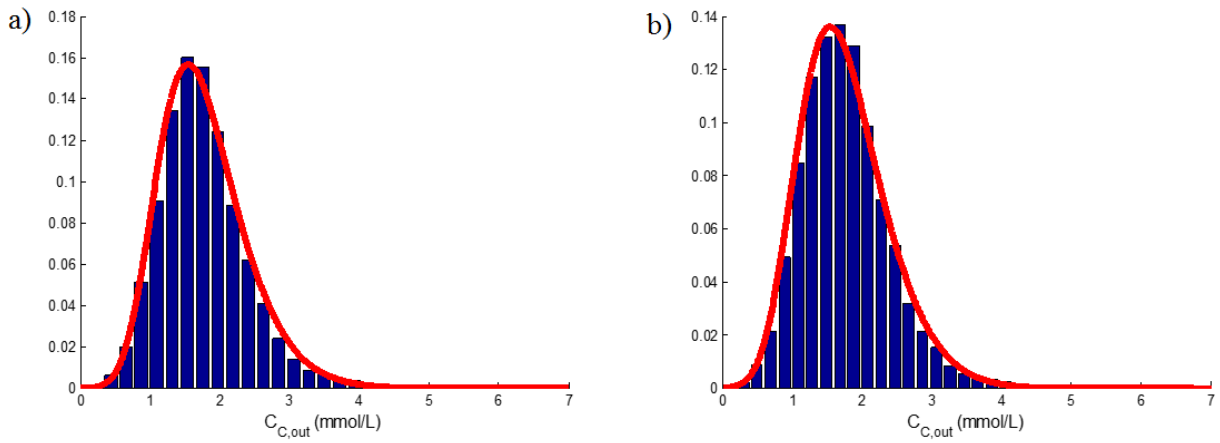

Figure 5-5. PDFs of the output fluid concentration for species C, $C_{C,out}$, using MC applied to the primary multiscale model (blue) and the second-order PSE (red) for (a) six uncertain parameters and (b) ten uncertain parameters.

The results from Figure 5-5 and Table 5-3 indicate that the second-order PSE is able to capture the output variability, as the PSE model errors for the mean and variance are below $\pm$ 1% while probabilistic bounds all remain within $\pm$ 5% of the bounds obtained from the primary reactor model. MC sampling directly applied to the primary model required a CPU time that is 12 and 35 times larger than the computational costs of the second-order PSE functions, respectively. Accuracy may be slightly improved using higher order PSEs; however, it requires substantially larger computational cost due to the additional multiscale simulations necessary to calculate the higher order sensitivities. Figure 5-5 illustrates that the inclusion of additional uncertain parameters produces slight changes in the shape of the concentration distributions. As shown in Tables 5-2 and 5-3, the lower and upper bounds deviated 230 and 57 µM respectively between the output variability for the six and the four uncertain parameter cases; likewise, the lower and upper bounds deviated 18 and 47 µM respectively between the six uncertain parameter and the ten uncertain parameter case. Tables 5-2 and 5-3 also show that higher CPU times are required to compute the PSE-based model when additional uncertain parameters are included in the analysis as there are more input-output sensitivities that need to be estimated thus requiring the need to perform additional sampling using the primary multiscale model. Figure 5-6 illustrates the effects of uncertainty on the concentration of species C as it varies along the axial reactor length, $C_C(x_{tooth}, \rho)$, when six and ten uncertain parameters are considered in the analysis. This figure reveals that the uncertainties are propagated axially, similar to the previous scenarios, resulting in larger variability at the pore outlet.

In the present scenario, the uncertainty in the pre-exponential factors for the desorption and reaction terms i.e. $k_{d,A}, k_{d,B}$, and k_r, were assumed to vary with a standard deviation of 10% of their nominal values. In principle, these terms can vary orders in magnitude from their corresponding expected values,[17] which

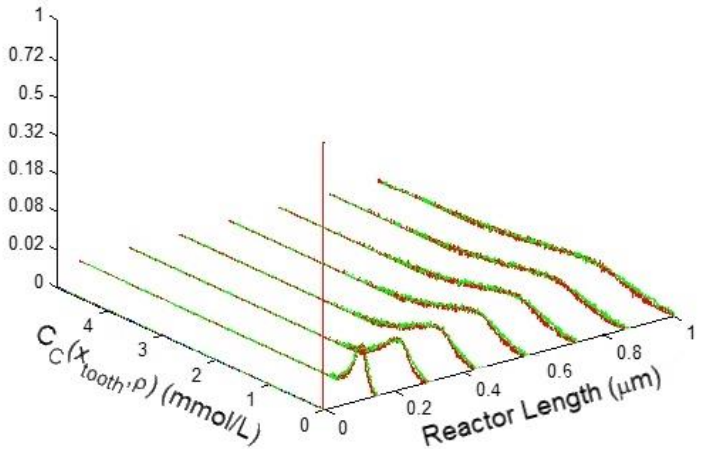

Figure 5-6. PDFs of the steady state fluid concentration for species C, $C_C(x_{tooth},\rho)$, along the reactor axial length; six uncertain parameters (red) and ten uncertain parameters (green).

could have a significant effect on the resulting output concentration profiles. To illustrate these effects, the standard deviations for the pre-exponential factors were increased from 10% to 32% of the corresponding nominal values, thus allowing these parameters to change by at least an order of magnitude with respect to their expected values. Figure 5-7 compares the variation in the concentration of the output product PDFs generated using the PSE approximation when the standard deviations of the pre-exponential factors are set to 10% and 32% of the nominal values respectively within the ten uncertain parameter case study. Similarly, the difference in the mean, variance, and probabilistic bounds are listed in Table 5-4. These results indicate that larger variations in the pre-exponential factor have significant effects on the output concentrations, resulting in a 13% wider standard deviation and a 6.5% shift in the upper and lower bounds for the outlet concentration of species C.

5.2 Robust Optimization

Process optimization is often sought as a practical tool for performance improvement. The quality of the solution obtained from optimization is directly determined by the accuracy of the model being used to represent the system under analysis and the model parameters. High-order models such as mechanistic models of large-scale or complex systems often cannot be embedded within an optimization framework due to excessive computational costs. In addition, model parameters are always subject to uncertainty which adds complexity into the analysis. Parametric uncertainty can be directly propagated through the system model to accommodate for its effects, however this approach can be computationally prohibitive to implement for a large number of uncertain parameters. Consequently, low-order models that capture the

Table 5-4. Distributional pre-exponential factor uncertainty analysis.

Pre-exponential Factor, Standard Deviation	$\mu(C_{C,out})$ **(mmol/L)**	$\sigma^2(C_{C,out})$ **(mmol^2/L^2)**	$C_{C,out}^{lw}$ **(mmol/L)**	$C_{C,out}^{up}$ **(mmol/L)**
10% of the Nominal Values	1.7510	0.3938	0.5067	3.5667
32% of the Nominal Values	1.7425	0.5056	0.3045	3.7732

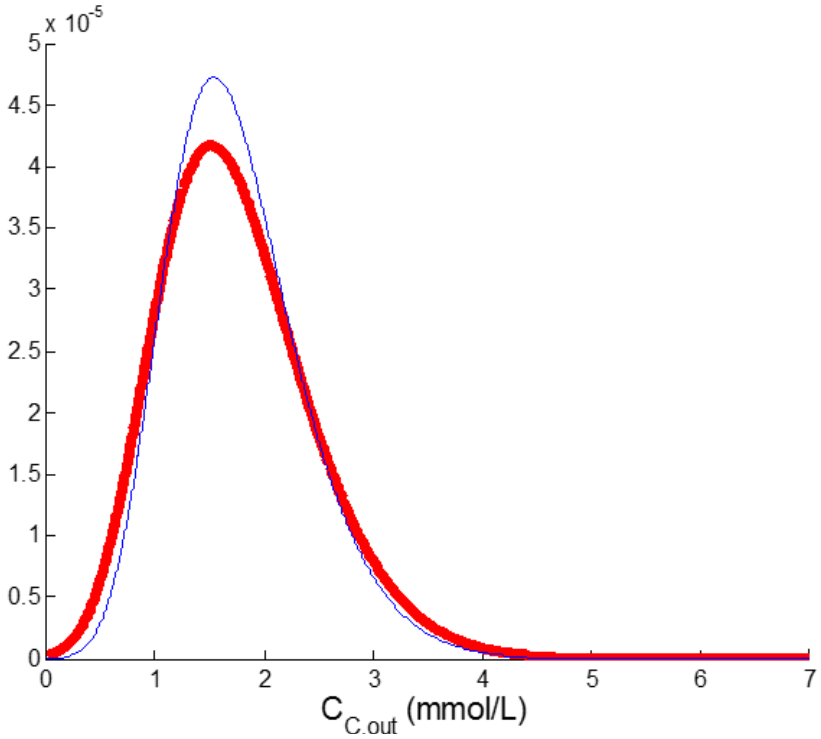

Figure 5-7. PDFs of the output fluid concentration for species C, $C_{C,out}$, for ten uncertain parameters using a standard deviation of 10% of the nominal value (blue) and 32% of the nominal value (red) in the pre-exponential factors.

key system characteristics under parameter uncertainty are used in model-based optimization to improve the performance of the process. These models are implemented subject to uncertainty in only the most sensitive key system parameters to effectively minimize computational costs.

In order to illustrate the benefits of applying the low-order series expansions discussed in Chapter 4 for uncertainty quantification, the PSE-based framework was used to identify the optimal operating conditions on the multiscale catalytic flow reactor system that maximize the reactor productivity under uncertainty in

the most relevant key system parameters. As shown in the previous sections, the present heterogeneous multiscale reactor model is subject to product concentration variability due to uncertain realizations in the model parameters. On the other hand, key operating conditions and design parameters such as the temperature (T), inlet fluid velocity (v), and pore length (L) can be adjusted to improve process productivity. Accordingly, a robust optimization formulation can be specified for this process as follows:

$$\max_{T,L,v} \Lambda\mu(C_{C,out}) - (1-\Lambda)\sigma^2(C_{C,out})$$

Subject to:

Multiscale model, Eqs. (3-1)-(3-24)

Uncertain parameter descriptions

PSE model, Eqs. (4-7)

$$T_{min} \leq T \leq T_{max}$$

$$L_{min} \leq L \leq L_{max}$$

$$v_{min} \leq v \leq v_{max} \qquad (5\text{-}4)$$

where $\mu(C_{C,out})$ represents the expected concentration of species C at the center of the pore outlet while $\sigma^2(C_{C,out})$ represents its variance. The parameter Λ is a weight that determines the significance of the expected value and variance in the optimization formulation. In principle, $\mu(C_{C,out})$ and $\sigma^2(C_{C,out})$ can be estimated through a large number of MC sampling points applied on the primary multiscale model. As shown in the results presented in the previous section, this approach is computationally prohibitive. Accordingly, $\mu(C_{C,out})$ and $\sigma^2(C_{C,out})$ in Eq. (5-4) are calculated using a second-order PSE. That is, for each set of values in the optimization variables, a second-order PSE is built, using the primary multiscale model, to estimate $\mu(C_{C,out})$ and $\sigma^2(C_{C,out})$. Note that the primary multiscale model is only used in Eq. (5-4) to compute the sensitivities needed for the PSE approximations. In the present analysis, the weight Λ in Eq. (5-4) was set to 0.5. Furthermore, uncertainty was considered in the three kinetic parameters $k_{a,A}, E_{d,A}, E_r$, and the pore radius ρ. Although it is important to account for uncertainty in all unknown parameters, the addition of each uncertain parameter results in additional computational costs. In order to perform efficient robust optimization, uncertainty was therefore only considered in the parameters that had the most significant impact on the catalytic reactor performance. The uncertainty analyses from the previous sections illustrated that although increasing the number of parameters did affect the product concentration PDF, they did not result in a substantial change in shape or in probabilistic bounds between *Scenario 2* and

the ten uncertain parameter study in *Scenario 3*. As a result, uncertainty was only considered in $k_{a,A}, E_{d,A}, E_r$, and ρ. The uncertainty in each of the parameters was assumed to follow a normal distribution with the means and standard deviations defined as in *Scenario 2*. To compare the results obtained from Eq. (5-4), a similar problem was formulated under the assumption of perfect knowledge of the model parameters, i.e.

$$\max_{T,L,u} \ \mu(C_{C,out})$$

Subject to:

Multiscale model, Eqs. (3-1)-(3-24)

$$T_{min} \leq T \leq T_{max}$$

$$L_{min} \leq L \leq L_{max}$$

$$\nu_{min} \leq \nu \leq \nu_{max} \qquad (5\text{-}5)$$

As shown in Eq. (5-5), only the expected value of the outlet concentration of species C was considered in the cost function. At each optimization step, simulations of the primary multiscale model were performed to compute $\mu(C_{C,out})$. For the two optimization problems (5-4) and (5-5), T_{min} and T_{max} were set to 300K and 700K while L_{min} and L_{max}were set to 0.5μm and 1.5μm and ν_{min} and ν_{max} were set to 5mm/s and 15mm/s, respectively.

The optimal reactor temperature, pore length, and fluid velocity obtained from the robust optimization formulation (*MaxConc*) and the nominal optimization formulation (*Nominal*), i.e. problems (5-4) and (5-5) respectively, are shown in Table 5-5. The mean, variance, and probabilistic bounds at a 2% confidence interval for the species C concentration PDFs obtained using these two optimization formulations are also shown in Table 5-5. For the case of the nominal optimization, the statistics on the process outputs were obtained by performing MC sampling on the primary multiscale model using the same uncertainty parameter descriptions as for problem (5-4). As shown in Table 5-5, large pore lengths ($L = L_{max}$) and small fluid velocities ($\nu = \nu_{min}$) are needed to maximize the production of species C, which is expected for a catalytic flow reactor system. Additionally, reasonably high temperatures maximize the number of reactions taking place on the surface to improve the production of species C. As shown in Figure 5-8, the concentration of species C experiences a maximum at T = 466K, as predicted by the nominal optimization results. This optimal temperature is a result of the surface reaction ensembles necessary for reaction to occur. Initially, increasing the temperature will increase the rate of reaction, resulting in higher product

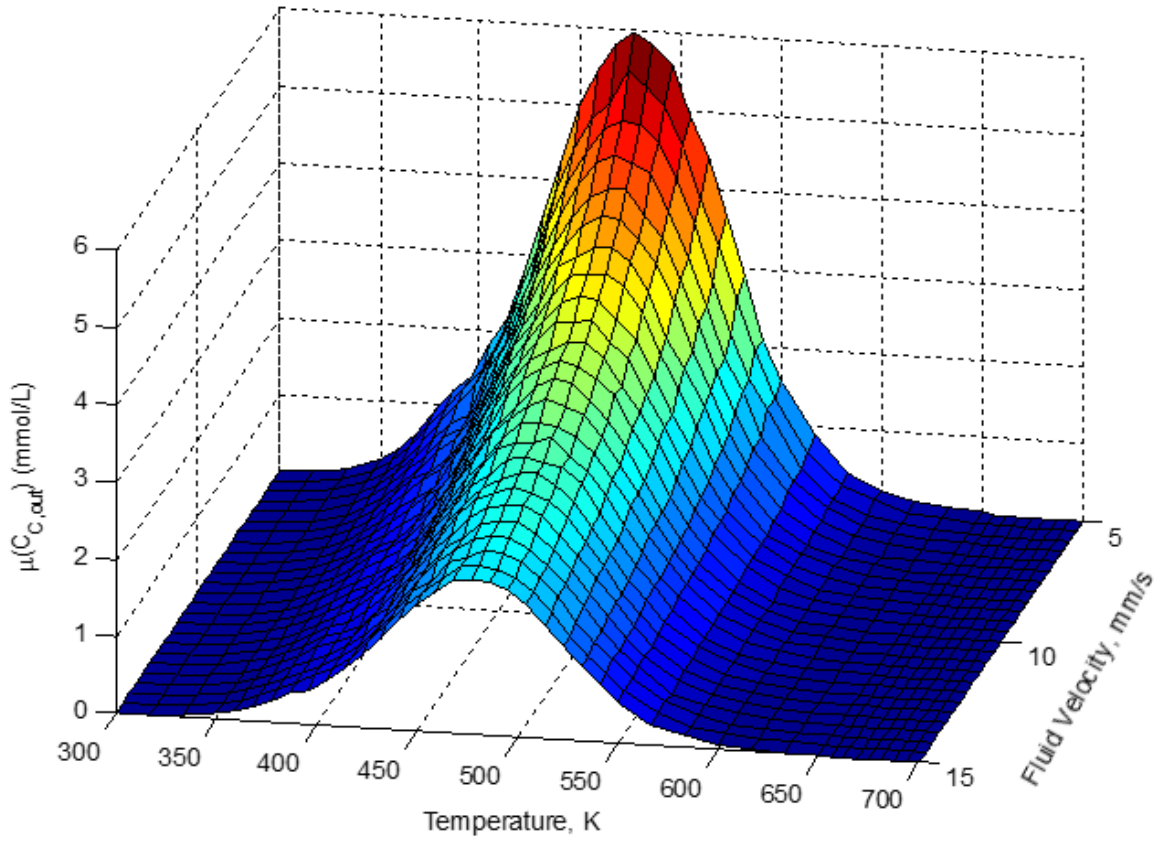

Figure 5-8. Nominal outlet fluid concentration for species C, $\mu(C_{C,out})$, as a function of temperature T and fluid velocity v; pore length L = 1.5 μm.

concentrations; however, at sufficiently high temperatures, the increasing desorption rate significantly affects the number of surface reaction ensembles, which decreases the reaction rate.

The results for the robust optimization under uncertainty (*MaxConc* in Table 5-5) indicate that a lower reactor temperature, with the same pore length and inlet velocity as that obtained from the nominal optimization, is needed to account for parameter uncertainty. As shown in Table 5-5, accounting for the variance in the outlet concentration due to parameter uncertainty results in a 9.76% and 3.92% decrease in the mean and variance of the product concentration, respectively, when compared to the nominal optimization. Figure 5-9 depicts the outlet concentration PDFs of species C from both the robust optimization formulation (*MaxConc*) and the nominal optimization formulation (*Nominal*). This figure shows that product variability can be reduced at the expense of reducing production of species C. To further investigate this condition, an additional robust optimization problem was formulated to minimize product variability under specific production constraints in the presence of uncertainty, i.e.

Table 5-5. Nominal and robust optimization results.

Optimization Scenarios	T (K)	L (μm)	v (mm/s)	$\mu(C_{C,out})$ (mmol/L)	$\sigma^2(C_{C,out})$ (mmol^2/L^2)	$C_{C,out}^{lw}$ (mmol/L)	$C_{C,out}^{up}$ (mmol/L)
Nominal Optimization (*Nominal*)	466	1.50	5.00	5.7568	3.4694	2.2658	11.2122
Robust Optimization (*MaxConc*)	455	1.50	5.00	5.1949	3.3331	1.5345	10.3859
Robust Optimization (*MinVar*)	466	1.44	5.54	5.0185	2.6944	2.0069	9.9064

$$\min_{T,L,v} \sigma^2(C_{C,out})$$

Subject to:

Multiscale model, Eqs. (3-1)-(3-24)

Uncertain parameter descriptions

PSE model, Eqs. (4-7)

$$\mu(C_{C,out}) \geq \mu^*(C_{C,out})$$

$$T_{min} \leq T \leq T_{max}$$

$$L_{min} \leq L \leq L_{max}$$

$$v_{min} \leq v \leq v_{max} \quad (5\text{-}6)$$

where $\mu^*(C_{C,out})$ represents a minimum acceptable concentration of species C on average, which was set to 5 mmol/L for this problem. Similar to the robust optimization problem (5-4), a second-order PSE was used to evaluate $\mu(C_{C,out})$ and $\sigma^2(C_{C,out})$. Additionally, the same uncertain parameter descriptions used to solve problem (5-4) were applied in this problem. The results from this optimization formulation are presented in Table 5-5 (*MinVar*) and Figure 5-9. These results reveal a 22.3% decrease in the variance of the outlet concentration PDF for species C when compared to the nominal optimization results; accordingly, the upper and lower bounds computed from the results of this robust optimization problem (*MinVar*) are

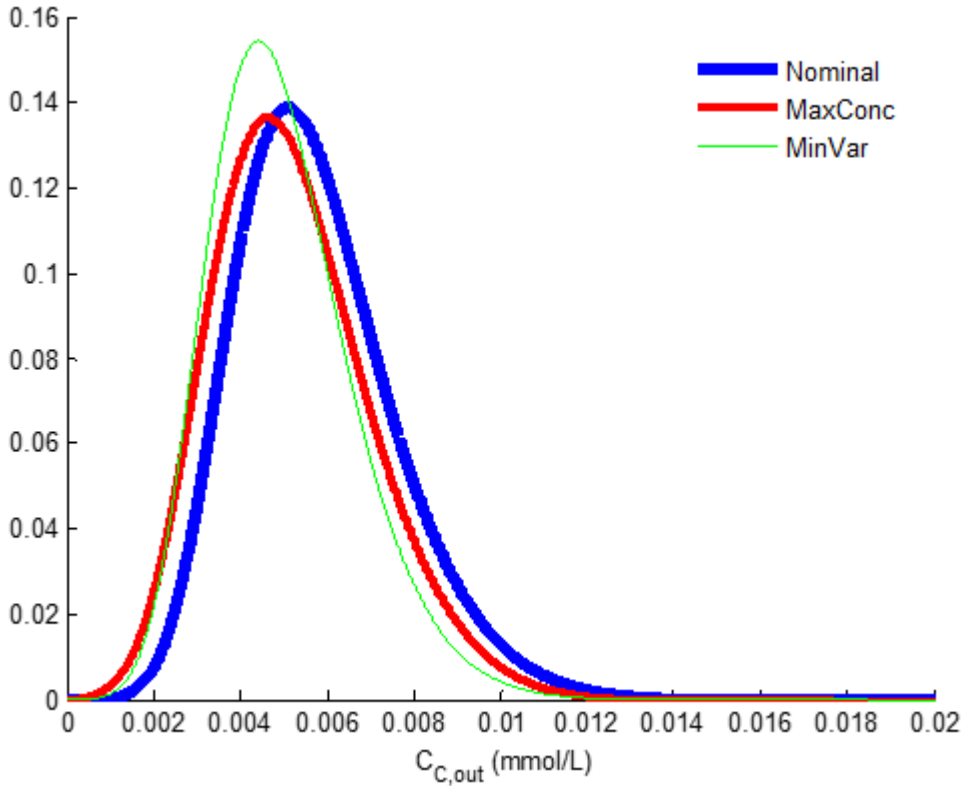

Figure 5-9. PDFs of the output fluid concentration for species C, $\mu(C_{C,out})$, at the nominal optimization conditions (Nominal, blue) and the robust optimization formulations, i.e. MaxConc (red) and MinVar (green).

10.4% and 13.7% closer to its mean value when compared to the bounds obtained from the nominal optimization formulation (*Nominal*). Note that the mean value in the production of species C obtained from *MinVar* is close to the production constraint considered in problem (5-4). These product specifications are obtained at approximately the same temperature as the nominal optimization results, but with a 60nm shorter pore length and with a 540μm/s faster inlet fluid velocity. Figure 5-9 clearly indicates that the results obtained from problem (5-6) produces a narrower distribution centered on its mean production value when compared to the distributions obtained from problems (5-4) and (5-5), respectively. These results show that parameter uncertainty play a key role and must be considered for process improvement in multiscale systems.

5.3 Summary

Model-based robust optimization of catalytic flow reactor systems are adversely affected by uncertainties in the system parameters. Consequently, it is important to understand the impact of uncertainty

in key system parameters on the overall performance of a catalytic reactor system. In this chapter, uncertainty analysis was performed on the multiscale catalytic flow reactor system and subsequently implemented into robust optimization schemes. Uncertainty in an increasing number of different key system parameters was propagated through the multiscale catalytic reactor using PSE to fully observe its impact on the reactor performance. This revealed that parametric uncertainty has a significant effect on the catalytic reactor performance and cannot be neglected in the design of the reactor. It was likewise observed that increasing the number of uncertain parameters has a significant impact on the product concentration PDFs, which illustrates the importance of propagating uncertainty in all uncertain parameters.

Increasing the number of uncertain parameters, however, additionally increases the computational cost of the analysis, and consequently there is a trade-off between accuracy and efficiency. Based on the results from the uncertainty analysis, robust optimization was performed on the catalyst reactor system considering uncertainty in only the most significant system parameters. For these optimization studies, uncertainty was considered in $k_{a,A}, E_{d,A}, E_r,$ and ρ, as it was observed that adding more uncertain parameters did not result in a critical change in the shapes of the product concentration PDFs or their statistical properties. PSE was used to propagate the uncertainty through the multiscale model in order to determine the mean and variance of the output distribution for use in the robust optimization scheme. This methodology was used in order to determine the temperature, reactor length, and fluid velocity values that simultaneously maximized the reactor productivity and minimized the variance of the product concentration PDFs due to uncertainty. These studies illustrated that parametric uncertainty can have a substantial effect on robust optimization and process improvement studies, which highlights the importance of taking uncertainty into account.

Chapter 6
Data-Driven Model-based Optimization of a Catalytic Reactor Subject to Spatially-Varying Uncertainty[†]

Catalysts are crucial to the majority of chemical fabrication applications. They are particularly advantageous as they are not consumed over the course of the reaction, and therefore do not need to be constantly resupplied. They are prone, however, to deactivation due to mechanisms such as catalyst poisoning and fouling, which can significantly impede the reactor productivity. In poisoning and fouling mechanisms, undesired species chemically or physically adhere to the catalyst active sites, blocking them from interacting with the system reactants and thus preventing them from catalyzing the reaction. In addition, catalyst poisons have been known to alter the electronic and structural properties of the catalyst.[36] Consequently, catalyst poisoning and fouling can have significant adverse effects on the catalyst performance.[18–20] Catalyst deactivation can be directly incorporated into the multiscale model through inclusion of the kinetic poisoning and fouling mechanisms; however, this approach requires explicit knowledge of the catalyst deactivation kinetics, and it can be computationally intensive to implement. Alternatively, the catalytic parameters can be directly adjusted to indirectly capture the effects of deactivation on the catalyst behaviour. However, in a catalytic reactor system subject to an unknown degree of poisoning or fouling, the values of the adjusted catalytic parameters would not be known with complete certainty unless additional tests were performed to assess the variation in the parameters needed to capture the reactor behaviour subject to various degrees of catalyst deactivation. Alternatively, these parameters could be treated as uncertain, such that the uncertainty propagation techniques discussed in previous chapters can be applied to account for the catalyst deactivation.

Further complications arise in catalytic flow-type reactors, where concentration gradients lead to non-uniform rates of catalyst deactivation along the catalyst surface.[20,108,109] The uncertainty in the catalyst parameters of a catalytic flow reactor would vary as a function of space, and multiple uncertainty descriptions would be required to capture the effects of poisoning and fouling along the length of the reactor. Consequently, a large number of uncertainty descriptions would be required to adequately account for the effects of parametric uncertainty in catalytic flow reactors subject to non-uniform catalyst deactivation, resulting in large computational costs. Despite the efficiency of PSE and PCE, these approaches would require significant computational power to adequately approximate the effects of spatially-varying uncertainty that are due to catalyst deactivation in the multiscale catalytic flow reactor system. Consequently, these methods may become computationally-prohibitive to implement for the robust

[†]The contents of this chapter have been accepted for publication in the Canadian Journal of Chemical Engineering.[26]

optimization of a poisoned catalytic flow reactor, since unique PSE or PCE models would be required at each operating point considered in the optimization process. Subsequently, it is necessary to develop alternative models to enable efficient optimization of a catalytic reactor system subject to non-uniform catalyst deactivation.

Based on the above, the aim of this chapter is to perform efficient robust optimization on a multiscale catalytic flow reactor system subject to spatially-varying uncertainty that is due to catalyst fouling. To that extent, the effects of spatially-varying uncertainty descriptions were analyzed on the performance of the steady-state multiscale catalytic reactor described in Chapter 3. Spatially-varying uncertainty was propagated through the reactor model by assigning unique uncertainty descriptions for the uncertain parameters at each tooth considered in the gap-tooth model. The impact of the spatially-varying uncertainty due to catalyst fouling was assessed via comparison to uncertain catalytic reactor systems where the uncertainty is constant in space. Subsequently, low-order DDMs were developed to capture the key statistical information of the product variability at the catalytic reactor outlet due to spatially-constant and spatially-varying uncertainty. These DDMs were implemented into robust optimization schemes to perform efficient optimization of the catalytic reactor system subject to spatially-varying uncertainty.

This chapter is organized as follows. In Section 6.1, uncertainty analysis is performed to compare the effects of spatially-constant and spatially-varying uncertainty descriptions on the catalytic reactor performance. In this study, PCE is used to efficiently propagate each parametric uncertainty description through the multiscale reactor model. In Section 6.2, the statistical DDM algorithm is discussed and implemented for efficient robust optimization of the multiscale catalytic reactor model that is subject to spatially-constant and spatially-varying uncertainty.

6.1 Spatially-Varying Uncertainty Analysis

The objective of this section is to analyze the impact of spatially-varying parametric uncertainty on the multiscale catalytic reactor performance using PCE. Spatial variation in the catalyst parameters is assumed to occur due to heterogeneous catalyst poisoning and fouling along the axial length of the reactor.[20,108,109] Catalyst deactivation is primarily known to affect the number of catalyst sites available for interaction with the reactant and product species;[18,19,103] however, it is challenging to propagate uncertainty through the number of available catalyst sites without directly simulating the kinetic events for the deactivation mechanisms. This is because the number of available catalyst sites has a direct effect on the kMC simulation lattices. Thus, any deactivated site due to poisoning and fouling would require random selection of a lattice site, which can become computational intensive or even prohibitive for actual applications. Furthermore, the poisoning and fouling mechanisms are subject to uncertainty thus increasing the problem's complexity.

In order to overcome this issue, the effects of catalyst deactivation on the multiscale reactor behaviour were approximated by propagating uncertainty through alternative catalytic parameters such as the activation energies of desorption and reaction. The catalyst deactivation varies as a function of the reactor axial length, and as a result, spatially-varying uncertainty distributions were applied to these parameters to account for the effects of catalyst deactivation on the catalytic reactor behaviour. Further complications arise due to the transient nature of catalytic poisoning and fouling. Specifically, catalyst deactivation is a dynamic process that accumulates over time, and special care must consequently be taken when analyzing the effects of poisoning and fouling within a steady-state catalytic reactor model. To overcome this issue, it was assumed that the steady-state reactor model implemented in this work would capture a snapshot of the catalytic reactor subject to an unknown degree of poisoning and fouling at a specific point in time. In order to extend the usefulness of this assumption, it was further assumed that the rates of the poisoning and fouling mechanisms were significantly lower than the rates of the reaction mechanism taking place (Eqs. (3-1)-(3-3)), i.e. the rates of catalyst deactivation were orders of magnitude slower than the reaction mechanism. Hence, the steady-state multiscale model behaviour dominates over the dynamic catalyst deactivation processes.

In order to fully assess the impact of spatially-varying parametric uncertainty on the catalytic flow reactor performance, uncertainty analysis was performed on the steady-state multiscale catalytic flow reactor model subject to spatially-constant and spatially-varying uncertainty distributions. For these studies, the catalyst surface domain was discretized into seven teeth (i.e. n_{teeth} = 7) separated by 143nm gaps. Parametric uncertainty due to catalytic deactivation was considered in the activation energy of desorption for species *A*, $E_{d,A}$. This parameter was chosen as it was determined to have the most significant effect on the catalyst reactor behaviour out of all the kinetic parameters. For the case of the spatially-constant uncertainty description, *Scenario 1A*, the parametric uncertainty was assumed to be normally distributed with statistical properties defined as follows:

$$\mu\left(E_{d,A}\right) = 95\text{kJ/mol}$$
$$\sigma^2\left(E_{d,A}\right) = 8.1225\text{kJ}^2/\text{mol}^2 \quad (6\text{-}1)$$

For the case of the spatially-varying uncertainty descriptions, *Scenario 1B*, a unique uncertainty description was applied at each of the seven teeth considered in the gap-tooth model ($I = 7$ in the PCE model). Note that the uncertainty in $E_{d,A}$ cannot vary radially as this parameter only affects phenomena that occur along the catalyst surface; thus, $J = 1$ in the PCE model. In addition, it was assumed that the rates of catalyst fouling would be highest at the center of the reactor pore ($x = 0.5, y = \rho$), and thus the uncertainty

in $E_{d,A}$ was assumed to be highest at the pore center and lowest at the pore inlets and outlets. The uncertainty distributions at each point were assumed to be normally distributed with their means and variances as follows:

$$\mu(E_{d,A}) = 95 \text{ kJ/mol}$$

$$\left[\sigma^2\left(E_{d,A}(0,\rho)\right), \dots, \sigma^2\left(E_{d,A}(x_{ud,i},\rho)\right), \dots, \sigma^2\left(E_{d,A}(L,\rho)\right)\right] =$$

$$[3.61, 8.1225, 14.44, 22.5625, 14.44, 8.1225, 3.61] \text{ kJ}^2/\text{mol}^2 \quad (6\text{-}2)$$

A graphical illustration of the uncertainty descriptions applied to $E_{d,A}$ as a function of the axial reactor length is presented in Figure 6-1a. Second-order Hermite polynomial PCEs (η = 2 in Eq. (4-12)) were used to propagate uncertainty through the primary multiscale model for both *Scenario 1A* and *Scenario 1B*. The PCE coefficients were calculated using the least-squares approach over 50 and 100 randomly-generated sample points for *Scenario 1A* and *Scenario 1B*, respectively. The number of sample points were determined *a priori* to be sufficient as increasing the number of points did not significantly alter the PCE model results. The effects of uncertainty were analyzed in the product concentration of species C at the reactor outlet $C_{C,out}$ in addition to seven points along the length of the reactor $C_C(x_{ov,u}, 0)$ where $x_{ov,u} = x_{tooth}$ correlates to the axial locations of each tooth considered in the gap-tooth model. Thus, seven unique PCE models were developed for each scenario in order to assess the impact of parametric uncertainty on the catalytic flow reactor system.

The statistical parameters derived from the uncertainty analysis are listed in Table 6-1 for both *Scenario 1A* and *Scenario 1B* at various spatial points along the catalytic reactor pore length. Table 6-1 additionally lists the computational costs required for each scenario. The probabilistic bounds were generated at a confidence level of α = 2%. Figure 6-2a and 6-2b additionally illustrate the product variability for *Scenario 1A* and *Scenario 1B* respectively at the reactor outlet ($C_{C,out}$) using PCE and MC sampling applied to the

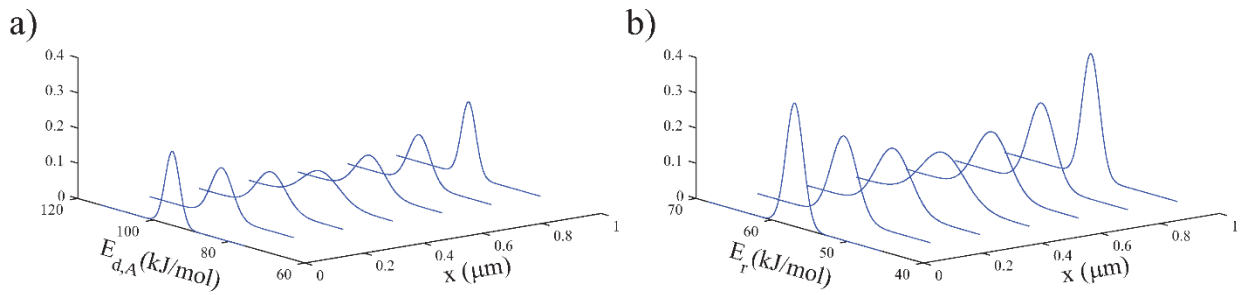

Figure 6-1. Spatially-varying uncertainty descriptions applied to a) $E_{d,A}$, b) E_r

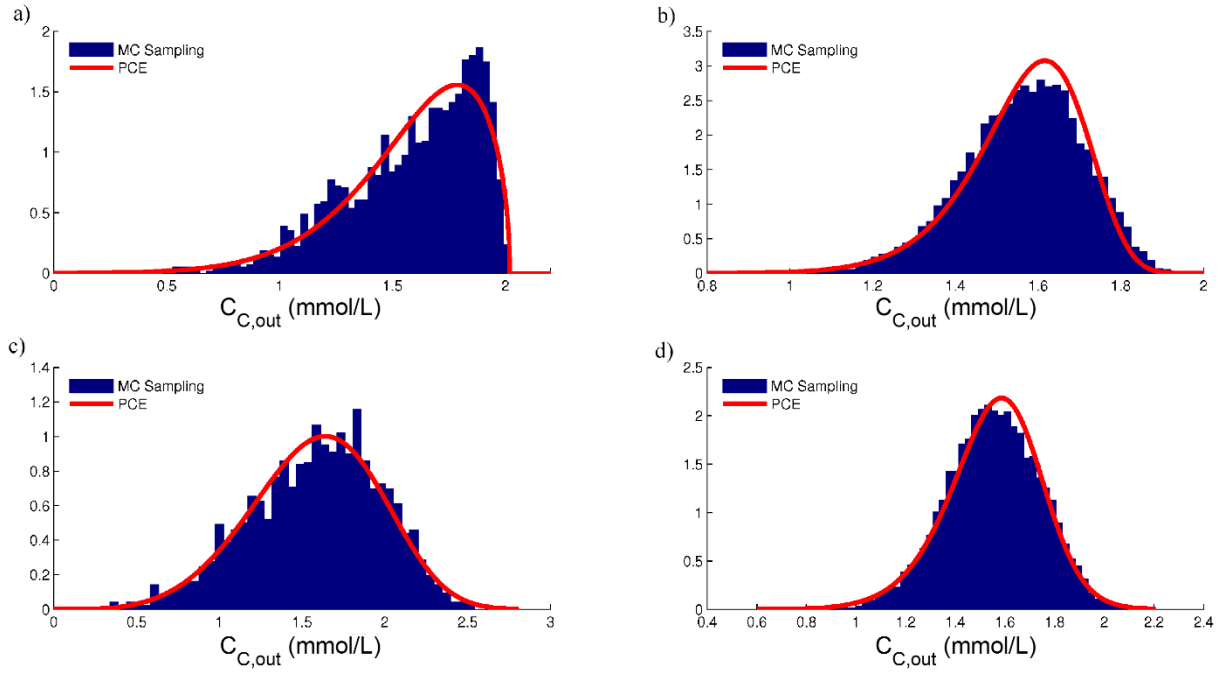

Figure 6-2. Graphical comparison of the output variability for $C_{C,out}$ determined via MC sampling (blue) and second-order PCE (red) for: a) *Scenario 1A* (MC determined via 1000 sample points), b) *Scenario 1B* (MC determined via 5000 sample points), c) *Scenario 2A* (MC determined via 1000 sample points), d) *Scenario 2B* (MC determined via 12 000 sample points)

primary multiscale model. Figure 6-3a similarly showcases the effects of parametric uncertainty for *Scenario 1A* and *Scenario 1B* at each tooth along the pore axial length. As shown in Figure 6-2, the PCE approximations provide accurate estimates of the product variability caused by each of the uncertainty descriptions considered. Additionally, Figures 6-2a, 6-2b, and 6-3a demonstrate that spatially-varying uncertainty descriptions have a significant impact on the ranges and shapes of the output PDFs. In particular, the right tail of the outlet PDFs demonstrate the most abrupt differences in shape between *Scenario 1A* and *Scenario 1B*, as illustrated Figures 6-2a and 6-2b. The right tail of the output PDF for *Scenario 1B* gradually decreases over increasing values of $C_{C,out}$ whereas the right side of the output PDF for *Scenario 1A* terminates abruptly at approximately $C_{C,out}$ = 2mmol/L. According to Table 6-1, the variances in the output PDFs for *Scenario 1B* are notably smaller than the variances in the output PDFs for *Scenario 1A* throughout the axial length of the reactor. In particular, the *Scenario 1B* variance is 40% smaller at the reactor's second tooth ($x = 0.1667$nm, $y = \rho$), and 77% smaller at the reactor outlet ($x = L, y = \rho$). Table 6-1 additionally demonstrates that there is a 1.5% decrease, an 8.5% decrease, and a 45% increase in the expected value, the upper bound, and the lower bound respectively between *Scenario 1B* and *Scenario 1A* at the reactor outlet. Note that the differences between *Scenario 1A* and *Scenario 1B* vary across the reactor axial length, as demonstrated in Figure 6-3a. The largest difference in the expected value does not occur at the reactor

Table 6-1. Statistical parameters for *Scenario 1A*, *Scenario 1B*, *Scenario 2A*, and *Scenario 2B* generated via PCE for the second tooth (x = 167nm), the fifth tooth (x = 667nm), and the seventh tooth ($x = L$).

		$\mu(C_{C,out})$ (mmol/L)	$\sigma^2(C_{C,out})$ (mmol^2/L^2)	$C_{C,out}^{up}$ (mmol/L)	$C_{C,out}^{lw}$ (mmol/L)	Computational Time (h)
Scenario 1A	**Second Tooth**	0.273052	0.002366	0.35937	0.136114	1.20
	Fifth Tooth	1.060009	0.039881	1.338404	0.508057	
	Seventh Tooth	1.588864	0.085173	1.981756	0.803473	
Scenario 1B	**Second Tooth**	0.27191	0.001413	0.331029	0.159438	2.39
	Fifth Tooth	1.039666	0.013819	1.234957	0.693248	
	Seventh Tooth	1.56425	0.019978	1.813259	1.162544	
Scenario 2A	**Second Tooth**	0.269546	0.004704	0.410496	0.087068	1.21
	Fifth Tooth	1.061179	0.072682	1.616761	0.342353	
	Seventh Tooth	1.579944	0.160057	2.403091	0.511757	
Scenario 2B	**Second Tooth**	0.270852	0.002622	0.38104	0.138607	4.18
	Fifth Tooth	1.032405	0.026899	1.37824	0.599408	
	Seventh Tooth	1.552789	0.036642	1.964148	1.062671	

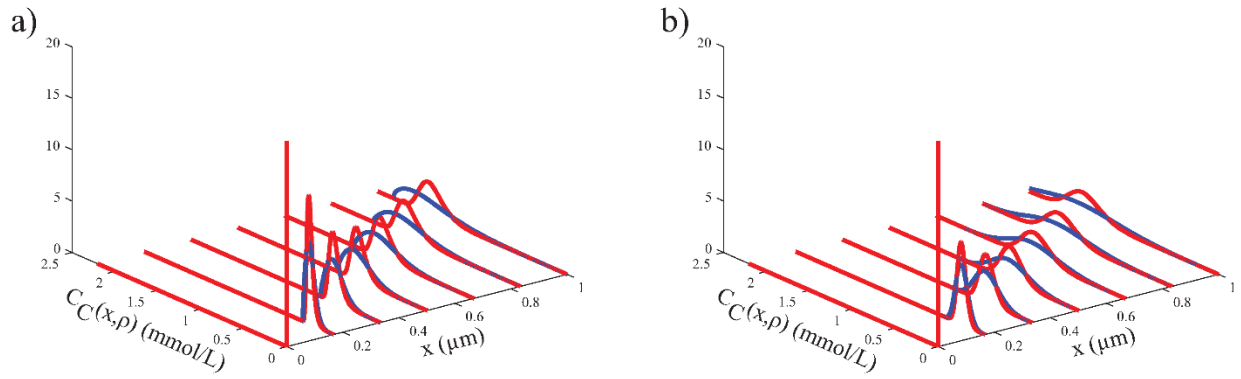

Figure 6-3. PDFs of the output variability in C_C as a function of reactor axial length for: a) *Scenario 1A* (blue) and *Scenario 1B* (red), b) *Scenario 2A* (blue) and *Scenario 2B* (red)

outlet as would be expected; according to Table 6-1, the largest difference occurs in the middle of the pore at the location corresponding to the reactor model's fifth tooth ($x = 0.667$nm, $y = \rho$), with a 1.9% difference as opposed to the 1.5% difference at the reactor outlet. This result clearly exhibits the effect of spatially-varying uncertainty on the reactor performance. Note that the computational cost for *Scenario 1B* (2.39 h) was approximately double the computational cost of *Scenario 1A* (1.20 h). This is primarily due to the number of sample points used to determine the PCE models for each scenario (50 points for *Scenario 1A* and 100 points for *Scenario 1B*.)

To further analyze the difference between spatially-constant and spatially-varying uncertainty distributions, the uncertainty analysis was expanded to consider uncertainty in more than one key parameter. In a realistic catalytic reactor scenario, few parameters would be known with complete certainty, and thus uncertainty would have to be applied to each system parameter. In addition, each of the parameters affected by catalyst deactivation would be subject to spatially-varying uncertainty along the reactor length. As a result, the most influential sensitive uncertain parameters to the system must be first identified. Subsequently, uncertainty can be propagated through the key parameters that have the most significant effects on the catalytic reactor performance in order to approximate the reactor behaviour under uncertainty. The remaining parameters can be assumed constant at their nominal values. Although this approach would not provide a complete description of realistic uncertainty propagation on the catalyst reactor system, it can provide a good approximation if sufficiently significant parameters are selected. For the catalytic reactor system considered in this work, it was determined that the activation energy of desorption for species A, $E_{d,A}$, and the activation energy of reaction, E_r, are the two parameters that had the most significant effect on the catalytic reactor performance. Consequently, the effects of spatially-varying uncertainty was assessed by applying spatially-constant and spatially-varying uncertainty descriptions to both parameters in order to account for the effects of catalyst deactivation on the reactor behaviour. In the case of the

spatially-constant uncertainty profiles, *Scenario 2A*, the parametric uncertainty was assumed to be normally distributed for both parameters, with means and variances defined as follows:

$$\left[\mu\left(E_{d,A}\right), \mu(E_r)\right] = [95, 57] \text{ kJ/mol}$$
$$\left[\sigma^2\left(E_{d,A}\right), \sigma^2(E_r)\right] = [8.1225, 2.9241] \text{ kJ}^2/\text{mol}^2 \quad (6\text{-}3)$$

In the case of the spatially-varying uncertainty descriptions, *Scenario 2B*, a unique uncertainty description was applied for both $E_{d,A}$ and E_r at each of the seven teeth considered in the gap-tooth model, for a total of 14 unique uncertainty descriptions. The uncertainty descriptions applied to $E_{d,A}$ were assumed to be normally distributed with the statistical parameters defined in Eq. (6-2). Likewise, the uncertainty descriptions applied to E_r were assumed to be normally distributed with statistical parameters defined as follows:

$$[\mu(E_r)] = 57 \text{ kJ/mol}$$
$$\left[\sigma^2(E_r(0,\rho)), \dots, \sigma^2\left(E_r\left(x_{ud,i},\rho\right)\right), \dots, \sigma^2(E_r(L,\rho))\right] =$$
$$[1.2996, 2.9241, 5.1984, 8.1225, 5.1984, 2.9241, 1.2996] \text{ kJ}^2/\text{mol}^2 \quad (6\text{-}4)$$

A graphical illustration of the uncertainty descriptions applied to $E_{d,A}$ as a function of the axial reactor length is presented in Figure 6-1a. Similarly, Figure 6-1b graphically displays the uncertainty descriptions applied to E_r as a function of the axial reactor length.

Second-order Hermite polynomial PCEs ($\eta = 2$ in Equation (4-12)) were used to propagate uncertainty through the primary multiscale model for both *Scenario 2A* and *Scenario 2B*. The PCE coefficients were calculated using the least-squares approach from data gathered over 50 and 175 randomly-generated sample points for *Scenario 2A* and *Scenario 2B* respectively.

The results and computational costs for both uncertainty analyses are detailed in Table 6-1. The probabilistic bounds were computed at a confidence level of α = 2%. In addition, Figure 6-2c and 6-2d illustrate the product variability for *Scenario 2A* and *Scenario 2B* respectively at the reactor outlet ($C_{C,out}$) using both PCE and MC sampling applied to the full multiscale model. Figure 6-3b similarly illustrates the effects of parametric uncertainty for both cases at each tooth along the axial length of the reactor. As described in Table 6-1, the computational cost for *Scenario 2B* was approximately 3.5 times higher than that of *Scenario 2A*. Similar to the previous scenarios, these differences are due to the number of sampling

points required to determine the PCE coefficients for both scenarios (50 points for *Scenario 2A* and 175 points for *Scenario 2B*). Figures 6-2c, 6-2d, and 6-3b illustrate that there are significant differences in the shapes and ranges of the output PDFs between *Scenario 2A* and *Scenario 2B*. However, the differences in the shapes are not as extreme as the differences observed between *Scenario 1A* and *Scenario 1B*. According to Table 6-1, the spatially-varying uncertainty distributions still have the greatest effect on the variance of the output distributions. In particular, the variance for *Scenario 2B* is 44% smaller than that of *Scenario 2A* at the reactor's second tooth ($x = 0.1667$nm, $y = \rho$), and 77% smaller at the reactor outlet ($x = L, y = \rho$). Additionally, there is an 18.3% increase in the upper bounds and a 108% decrease in the lower bounds is observed in *Scenario 2B* relative to *Scenario 2A*. Similar to the single uncertain parameter cases (*Scenario 1A* and *Scenario 1B*), the difference in the expected value is greatest at the fifth tooth in the reactor model, ($x = 0.667$nm, $y = \rho$), which is 2.7% lower for *Scenario 2B* than for *Scenario 2A*. On the other hand, there is only a 1.7% decrease in the expected value between *Scenario 2B* and *Scenario 2A* at the reactor outlet, as illustrated in Table 6-1. These results demonstrate that spatially-varying uncertainty descriptions can have a significant impact on the catalytic reactor behaviour and must be incorporated into catalytic reactor models when spatially-varying catalyst deactivation is present.

6.2 Robust Optimization Using Statistical Data-Driven Models

This section aims to perform robust optimization on the multiscale catalytic flow reactor process. In order to provide efficient optimization of the multiscale catalytic reactor model subject to a large number of uncertainty descriptions, statistical DDMs were determined to model the key statistical parameters of the variability in the reactor outlet product concentration, $C_{C,out}$. These DDMs were subsequently embedded within robust optimization schemes to determine the values of key design and operational parameters that maximize the reactor productivity. The pathway from the multiscale model to the robust optimizer can therefore be described as follows. The primary multiscale model is used to determine sample points at random realizations of the uncertain parameters and at each combination of design and operation parameters. These points are used to determine the PCE model coefficients that describe the parametric uncertainty at each combination between the design and operation parameters. The resulting PCE models are then used to determine the statistical information (mean, variance, and probabilistic bounds) for each combination of design and operation parameter conditions, which are the key inputs used to construct the DDMs. The DDMs are subsequently embedded within the robust optimizer in order to determine the conditions that maximize the reactor productivity. The next section describes the algorithm used to calculate the statistical DDMs for the multiscale catalytic reactor model subject to uncertainty. The performance of the statistical DDMs were subsequently validated by comparison to the uncertain catalytic reactor behaviour

as determined via PCE at random values for the desired design and operating conditions. These DDMs were subsequently implemented into efficient robust optimization schemes that aim to maximize the reactor productivity and minimize the reactor variability subject to the spatially-constant and spatially-varying uncertainty descriptions detailed previously.

6.2.1 Statistical Data-Driven Model Determination and Assessment

The statistical data-driven modeling approach seeks to develop low-order DDMs to estimate the values of key statistical parameters of the process output variability over a specified range of design and operational parameters **X**. The DDMs are highly efficient and require substantially lower computational costs compared to uncertainty propagation techniques such as PCE, which makes them ideal for process improvement and robust optimization studies. However, DDMs are less accurate compared to the aforementioned uncertainty propagation techniques which can limit their applications in systems that are highly sensitive to **X**. In this work, DDMs are determined using output information gathered at discrete operating points for each input design and operational parameter. This data is most readily determined using low-order mathematical approaches such as PCE to propagate parametric uncertainty to the model outputs $\boldsymbol{\psi}$. The DDM approach incorporated in this work was adapted from previous DDM algorithms in the literature.[129,130] The description below provides a general algorithm that can be used to compute DDMs for an output parameter of interest ψ_n at a point $(x_{ov,u}, y_{ov,v})$ over a given range of Q different design and operational parameters labeled as $\boldsymbol{\chi}_1, \dots, \boldsymbol{\chi}_q, \dots, \boldsymbol{\chi}_Q$.

1. Discretize the operational region for each input parameter $\boldsymbol{\chi}_q$ into $\mathcal{N}_q$ equidistantly-spaced values χ_{q,n_q} separated by intervals of $\Delta\chi_q$ as follows:

$$\boldsymbol{\chi}_q = \left[\chi_{q,1}, \dots, \chi_{q,n_q}, \dots, \chi_{q,\mathcal{N}_q}\right] \in \mathbb{R}^{\mathcal{N}_q},$$
$$\chi_{q,n_q} = \left\{\chi_{q,min} + (n_q - 1)\Delta\chi_q \middle| \chi_{q,min} \leq \chi_{q,n_q} \leq \chi_{q,max}, n_q = 1, 2, \dots, \mathcal{N}_q\right\} \quad (6\text{-}5)$$

   Note that the accuracy of the data-driven models can be improved by increasing $\mathcal{N}_q$; however, a large $\mathcal{N}_q$ can significantly increase the computational costs. Thus, the minimum number of discretization points for each input parameter $\boldsymbol{\chi}_q$ needed to achieve sufficient DDM accuracy must be determined *a priori* by analyzing how each of the model outputs ψ_n are affected by $\boldsymbol{\chi}_q$ and selecting the number of points needed to adequately fit the data to a low-order model.

2. Apply the PCE algorithm described previously to determine the variability in $\boldsymbol{\psi}(x_{ov,u}, y_{ov,v})$ with respect to the uncertain parameters $\boldsymbol{\Phi}$ at each combination of the input design and operational parameters $\left(\chi_{1,n_1}, \dots, \chi_{q,n_q}, \dots, \chi_{Q,n_Q}\right)$. The PCE results can be used to determine the mean $\mu\left(\psi_n(x_{ov,u}, y_{ov,v})\right)$, the variance $\sigma^2\left(\psi_n(x_{ov,u}, y_{ov,v})\right)$, and the upper and lower bounds $\psi_n^{up}(x_{ov,u}, y_{ov,v})$ and $\psi_n^{lw}(x_{ov,u}, y_{ov,v})$ at each combination of input parameters $(\chi_{1,n_1}, \dots, \chi_{q,n_q}, \dots, \chi_{Q,n_Q})$. Note that the accuracy of the DDMs is directly proportional to the accuracy of the PCE models used to generate the data points.
3. Based on the design and operational parameters values (i.e. the input) and the statistics of the output variables (i.e. the outputs), select suitable models to correlate the statistical data determined in the previous step to the input operational and design parameters $\boldsymbol{\chi}_1, \dots, \boldsymbol{\chi}_q, \dots, \boldsymbol{\chi}_Q$. The selection of suitable data-driven models is problem-specific and depends on the correlation and sensitivity between the input-output information. Thus, a general model selection procedure is not currently available; typically, model selection is mostly based from observations and process experience.
4. Estimate the parameter values for the models selected in the previous step using model regression techniques such as the least-squares approach.

Using this algorithm, low-order statistical DDMs were constructed to approximate key statistical parameters of the output variability in the multiscale single-pore catalytic reactor model subject to parametric uncertainty. The DDMs were determined as a function of the reactor temperature T, the fluid velocity v, and the pore radius ρ, which were considered as the optimization parameters in this analysis. The statistical data used to determine the DDMs were obtained using the PCE-based algorithm proposed in Chapter 3 over an operational temperature range of 446K $\leq T_{n_T} \leq$ 486K, a fluid velocity range of 6mm/s $\leq v_{n_v} \leq$ 14mm/s, and a range in the pore radius between 6nm $\leq \rho_{n_\rho} \leq$ 14nm. The input parameters to the DDMs, i.e. T, v, and ρ, were discretized into $\mathcal{N}_T = 5$ temperature values, $\mathcal{N}_v = 3$ fluid velocity values, and $\mathcal{N}_\rho = 3$ pore radius values. The number of discretization points was determined *a priori* to be the lowest number of data points needed to adequately capture the reactor variability subject to each of these design and operational parameters. Following the discretization, PCE was used to determine the mean, $\mu(C_{C,out})$, the variance, $\sigma^2(C_{C,out})$, the upper bound, $C_{C,out}^{up}$, and the lower bound $C_{C,out}^{lw}$ for each of the 45 possible combinations of T_{n_T}, v_{n_v}, and ρ_{n_ρ} subject to each of the uncertainty descriptions presented in *Scenarios 1A-2B* (Eqs. (6-1)-(6-4)). The upper and lower bounds were generated at a confidence interval of α = 2%. The generated data was fit to suitable models of the following form:

$$Z\left(C_{C,out}\right) = f(T, \nu, \rho) \tag{6-6}$$

Where $Z\left(C_{C,out}\right)$ represents a key statistical parameter of the variability in $C_{C,out}$. Further information concerning the determination of the DDMs can be found in Appendix A. The coefficients of the DDMs were determined using the least-squares approach to fit the PCE-generated data to T_{n_T}, ν_{n_ν}, and ρ_{n_ρ} for each of the uncertainty descriptions considered. The DDMs for the uncertainty descriptions used in *Scenarios 1A* and *2A*, *Scenario 1B*, and *Scenario 2B* required 50h, 100h, and 190h to compute respectively using PCE. The model coefficients determined for each DDM are listed in Appendix A.

In order to assess the accuracy of the statistical DDM approach, the DDMs constructed subject to the spatially-varying uncertainty conditions in Eq. (6-2) (*Scenario 1B*) were graphically assessed with respect to the PCE-generated data points for each of the statistical parameters, as illustrated in Figure 6-4. This figure demonstrates that the DDMs can fit the generated data quite well, as significant deviations were only observable in the relationship between the variance and the reactor temperature. This is because the relationship between $\sigma^2\left(C_{C,out}\right)$ and T varies sporadically and there is consequently no clear-cut model that can perfectly fit the variance data. Therefore, the temperature dependence of the variance was approximated using a linear relationship, as presented in Appendix A, as this was determined to provide the most accurate representation of the variance for all values of T. To demonstrate the performance of the statistical DDMs, five randomly-generated combinations of T, ν, and ρ were passed through the DDMs constructed using the spatially-varying uncertainty PDF described in *Scenario 1B*. These results were compared to those generated using PCE subject to the same uncertainty descriptions under the same combinations of T, ν, and ρ. Table 6-2 compares the results obtained from the DDMs and from the PCE approximations for each of the five randomly-generated input parameter combinations. As these results demonstrate, the DDMs are able to predict the catalytic flow reactor behaviour with sufficient accuracy over the desired range of input parameters. Significant errors (>10%) were only observed in the variance, however this was to be expected due to large deviations observed between the DDMs and the PCE model with respect to this statistic. Similar comparisons were implemented to assess the performance of the DDMs subject to the uncertainty descriptions in *Scenarios 1A*, *2A*, and *2B*. The results of these analyses are detailed in Appendix A.

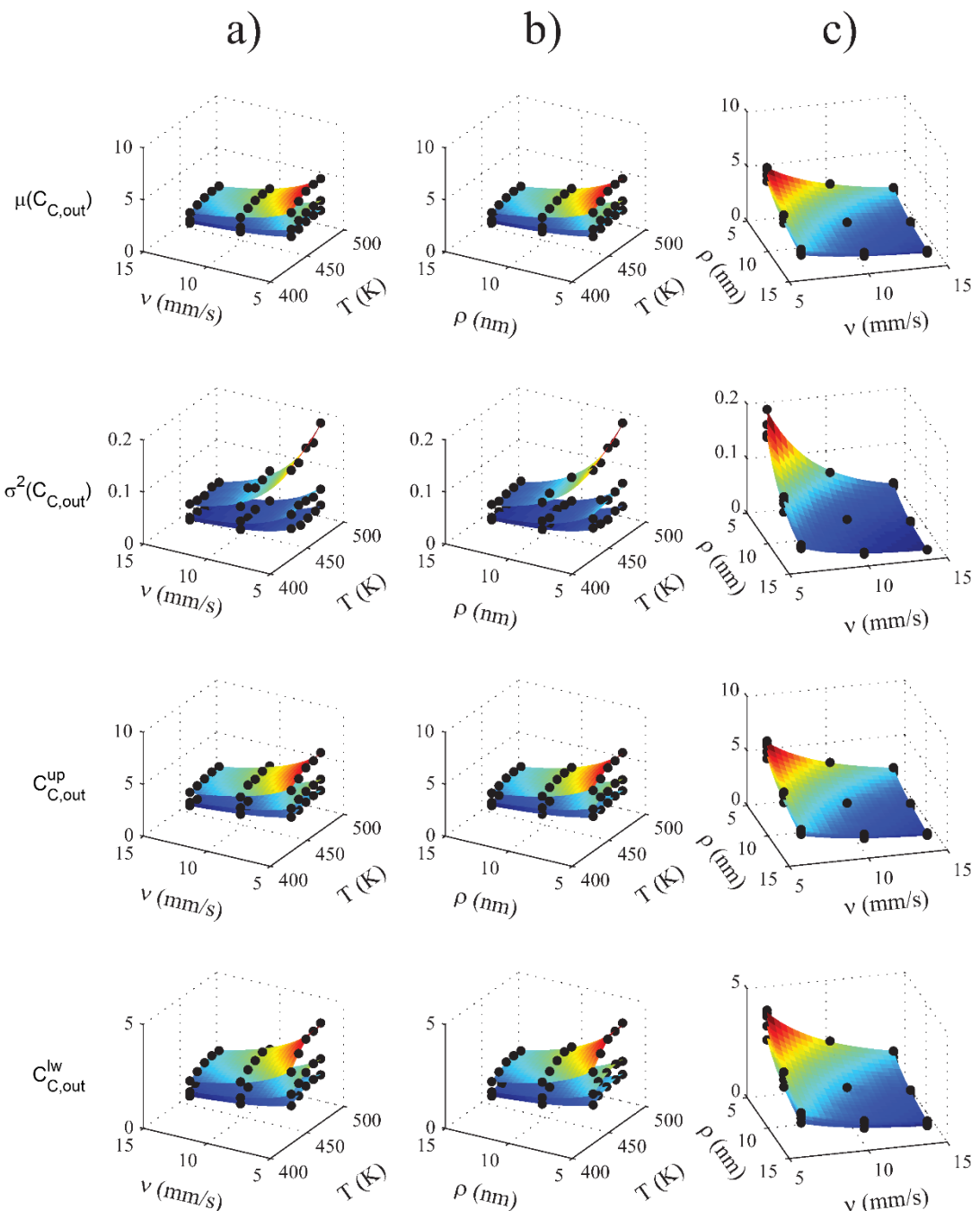

Figure 6-4. Comparison of the DDMs for $\mu(C_{C,out})$, $\sigma^2(C_{C,out})$, $C^{up}_{C,out}$, and $C^{lw}_{C,out}$ to the PCE-generated data points with respect to: a) temperature and fluid velocity for various pore radii values, b) temperature and pore radius for various fluid velocity values, and c) fluid velocity and pore radius for various temperature values. The data points were generated at each combination of the reactor temperature values T = [446, 456, 466, 476, 486] K, the fluid velocity values ν = [6, 10, 14] mm/s, and the pore radius values ρ = [6, 10, 14] nm.

Table 6-2. Accuracy of the DDMs for for $\mu(C_{C,out})$, $\sigma^2(C_{C,out})$, $C_{C,out}^{up}$, and $C_{C,out}^{lw}$ compared to five randomly-generated sample points determined via PCE.

			$\mu(C_{C,out})$ (mmol/L)	$\sigma^2(C_{C,out})$ (mmol^2/L^2)	$C_{C,out}^{up}$ (mmol/L)	$C_{C,out}^{lw}$ (mmol/L)
Point 1: MC sampling	***T* (K)**	485.88	1.78781	0.02188	2.09602	1.42984
	***v* (mm/s)**	10.500				
PCE			1.79060	0.02318	2.11632	1.37263
	***ρ* (nm)**	10.263	(0.16%)	(5.95%)	(0.97%)	(4.00%)
Point 2: MC sampling	***T* (K)**	447.82	0.99798	0.00871	1.17390	0.71213
	***v* (mm/s)**	13.108				
PCE			1.00657	0.00983	1.21028	0.72746
	***ρ* (nm)**	11.532	(0.86%)	(12.9%)	(3.10%)	(2.15%)
Point 3: MC sampling	***T* (K)**	467.89	2.33791	0.03778	2.67874	1.80561
	***v* (mm/s)**	7.3199				
PCE			2.33277	0.04040	2.72809	1.78492
	***ρ* (nm)**	10.859	(0.22%)	(6.94%)	(1.84%)	(1.15%)
Point 4: MC sampling	***T* (K)**	473.52	2.10901	0.03463	2.40456	1.63539
	***v* (mm/s)**	7.6877				
PCE			2.09779	0.03175	2.45158	1.61055
	***ρ* (nm)**	11.802	(0.53%)	(8.32%)	(1.96%)	(1.52%)
Point 5: MC sampling	***T* (K)**	463.65	2.69515	0.04951	3.07983	2.09216
	***v* (mm/s)**	8.7780				
PCE			2.69109	0.05549	3.16913	2.04680
	***ρ* (nm)**	7.6514	(0.15%)	(12.1%)	(2.90%)	(2.17%)

6.2.2 Robust Optimization

In this section, the DDMs constructed in the previous section were implemented to perform robust optimization on the single-pore catalytic reactor system. The optimization scheme sought to determine the values of key design and operating parameters (i.e. the reactor temperature T, the fluid velocity v, and the pore radius ρ) that improve the reactor performance subject to each of the parametric uncertainty descriptions listed in Equations (6-1)-(6-4). This section considers two different optimization schemes. The first optimization scenario, *maxProd*, aims to enhance the reactor performance by maximizing the expected value of the outlet product concentration, $\mu(C_{C,out})$, in order to improve the anticipated yield of the product species C. This scenario is meant to illustrate how the reactor performance can be optimized under nominal circumstances. The second optimization scenario, *minImpact*, seeks to minimize the impact of parametric uncertainty on the reactor system in a two-fold approach. First, it aims to minimize the product variability due to parametric uncertainty by decreasing the difference between the upper and lower bounds (i.e. $C_{C,out}^{up} - C_{C,out}^{lw}$). Secondly, this scenario aims to maximize the lower bound of the product outlet concentration, $C_{C,out}^{lw}$, in order to maximize the reactor productivity under uncertainty. This scenario is meant to illustrate how the effects of parametric uncertainty on the reactor performance can be minimized while simultaneously aiming to maximize the reactor productivity. Note that these optimization scenarios can be readily implemented subject to uncertainty in any of the remaining system parameters. Nevertheless, each different uncertainty formulation will require the development of a new DDM model to determine the key statistical parameters for the catalytic reactor behaviour. Such an approach can be computationally costly to implement for a realistic scenario with multiple sources of uncertainty in each of the uncertain parameters.

As stated previously, the first scenario (*maxProd*) aims to maximize the expected value of the catalytic reactor model, as described in the following formulation:

$$\max_{T,v,\rho} \mu(C_{C,out})$$

Subject to:

Parametric Uncertainty, Equations (6-1)-(6-4)

DDMs, Equation (6-6)

$$T_{min} \leq T \leq T_{max}$$

$$v_{min} \leq v \leq v_{max}$$

$$\rho_{min} \leq \rho \leq \rho_{max} \qquad (6\text{-}7)$$

In the formulation depicted above, the reactor performance was optimized with respect to the mean value of the outlet product concentration, $\mu(C_{C,out})$ while accounting for uncertainty in the kinetic parameters, $E_{d,A}$ and E_r, as detailed in *Scenarios 1A-2B*. The parameters were constrained by their minimum and maximum values, where $[T_{min}, T_{max}] = [446, 486]$ K, $[\nu_{min}, \nu_{max}] = [6, 14]$ mm/s, and $[\rho_{min}, \rho_{max}] = [6, 14]$ nm. The optimization problem was implemented for each of the uncertainty descriptions considered in the Section 6.1, i.e. constant uncertainty in $E_{d,A}$ (*Scenario 1A*, Equation (6-1)), spatially-varying uncertainty in $E_{d,A}$ (*Scenario 1B*, Equation (6-2)), constant uncertainty in $E_{d,A}$ and E_r (*Scenario 2A*, Equation (6-3)), and spatially-varying uncertainty in $E_{d,A}$ and E_r (*Scenario 2B*, Equation (6-4)). DDMs were constructed for each scenario by fitting PCE-generated statistical data for each uncertainty description to the models presented in the Appendix A. A complete listing of the DDM coefficients for each scenario can additionally be found in Appendix A.

The results of the optimization study for each uncertainty description are listed in Table 6-3. Additionally, Figure 6-5 depicts the PDFs for the output variation in $C_{C,out}$ at the optimal conditions for each of the uncertainty descriptions considered. Table 6-3 demonstrates that the optimal operating

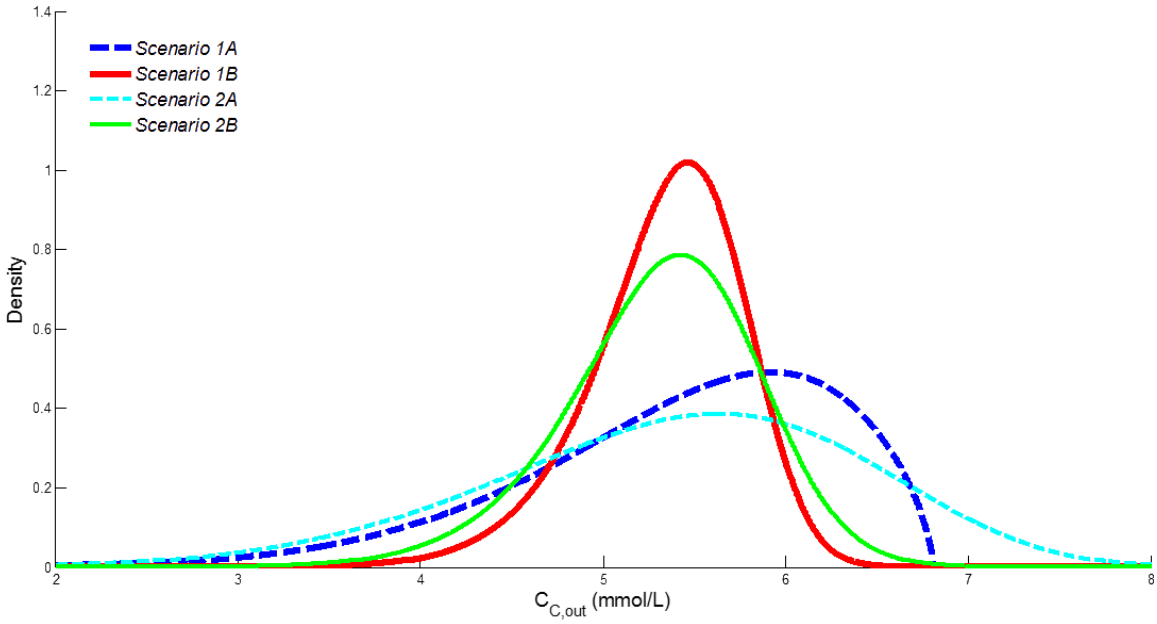

Figure 6-5. Predicted reactor performance and uncertainty variation in the outlet product concentration $C_{C,out}$ at the specific design and operating conditions that maximize the expected value of $C_{C,out}$ (*maxProd*) subject to the following uncertainty distributions: a) *Scenario 1A*, b) *Scenario 1B*, c) *Scenario 2A*, d) *Scenario 2B*

Table 6-3. Optimization results: *maxProd*

	Optimal Conditions		$\mu(C_{C,out})$ (mmol/L)	$\sigma^2(C_{C,out})$ (mmol²/L²)	$C_{C,out}^{up}$ (mmol/L)	$C_{C,out}^{lw}$ (mmol/L)
Scenario 1A	***T* (K)**	480.3	5.410922	0.7133601	6.827551	2.827122
	***v* (mm/s)**	6.0				
	***ρ* (nm)**	6.0				
Scenario 1B	***T* (K)**	480.8	5.349082	0.18956324	6.202265	4.12735
	***v* (mm/s)**	6.0				
	***ρ* (nm)**	6.0				
Scenario 2A	***T* (K)**	480.5	5.376998	1.19838621	7.428064	2.298057
	***v* (mm/s)**	6.0				
	***ρ* (nm)**	6.0				
Scenario 2B	***T* (K)**	480.9	5.316916	0.27437001	6.442276	3.96698
	***v* (mm/s)**	6.0				
	***ρ* (nm)**	6.0				

conditions for all four uncertainty distributions occur at the slowest fluid velocities, the smallest pore radii, and at moderately-high temperature values around 480 K. These results are in agreement with the findings in Chapter 5. The results in Figure 6-5 and Table 6-3 additionally demonstrate the impact of spatially-varying uncertainty descriptions on the catalytic reactor behaviour. Figure 6-5 illustrates that under the optimal conditions, there are significant differences in the PDF shape when spatially-constant and spatially-varying uncertainty descriptions are applied. Similarly, Table 6-3 shows that under optimal conditions, the expected values, variances, and upper and lower bounds differ by 1.14%, 73.4%, 9.16%, and 46.0% respectively between *Scenario 1B* and *Scenario 1A*. Similarly, the means, variances, and upper and lower bounds differ by 1.11%, 77.1%, 13.3%, and 72.6% respectively between *Scenario 2B* and *Scenario 2A* under the optimal conditions. These results demonstrate that spatially-varying parametric uncertainty can have significant impact on the optimal reactor performance and must be accounted for in order to minimize model-plant mismatch.

The second optimization scenario, *minImpact*, aims to minimize the impact of parametric uncertainty on the catalytic reactor model, as described previously. This is accomplished by maximizing the reactor

productivity subject to parametric uncertainty while minimizing the variability in the outlet product concentration. This robust optimization formulation can be expressed as follows:

$$\max_{T,v,\rho}\left[\Lambda C_{C,out}^{lw} - (1-\Lambda)\left(C_{C,out}^{up} - C_{C,out}^{lw}\right)\right]$$

Subject to:

Parametric Uncertainty, Equations (6-1)-(6-4)

DDMs, Equation (6-6)

$$\mu\left(C_{C,out}\right) \geq \mu^{*}\left(C_{C,out}\right)$$

$$T_{min} \leq T \leq T_{max}$$

$$v_{min} \leq v \leq v_{max}$$

$$\rho_{min} \leq \rho \leq \rho_{max} \qquad (6\text{-}8)$$

where $\mu^{*}\left(C_{C,out}\right)$ denotes the minimum acceptable mean value of the outlet product concentration, $C_{C,out}$, which was set to $\mu^{*}\left(C_{C,out}\right) = 3$mmol/L for this optimization formulation. Similarly, the significance of the output variability and the lower bound on the reactor optimization is controlled through the weight term, Λ, which was assigned a value of $\Lambda = 0.25$.

The optimization study results subject to each uncertainty distribution are listed in Table 6-4. Furthermore, Figure 6-6 provides a graphical illustration of the variation in $C_{C,out}$ at the optimal conditions for each of the uncertainty descriptions considered. The results in Figure 6-6 illustrates that under the optimal conditions, there are significant differences in the PDF shape when spatially-constant and spatially-varying uncertainty descriptions are applied. This is most notable in the graphical differences between the PDFs for *Scenario 1A* and *Scenario 1B*, which exhibits the same distinct differences under optimal conditions that were observed under nominal conditions as detailed in Section 6.1. The results in Table 6-4 demonstrate that the optimal region occurs at moderate temperatures between $T = 474$K and $T = 481$K, low fluid velocities between $v = 6$mm/s and $v = 9$mm/s, and intermediate pore radius sizes between $\rho = 7$nm and $\rho = 11$nm. The optimal results for the spatially-varying uncertainty distributions (*Scenario 1B* and *Scenario 2B*) can be found at higher temperatures, lower fluid velocities, and larger pore radii than the optimal results for their constant uncertainty counterparts (*Scenario 1A* and *Scenario 2A*). In addition, the results in Table 6-4 indicate that the reactor output variability for the spatially-varying uncertainty descriptions are smaller than those observed for spatially-constant uncertainty profiles under optimal conditions. In particular, there is a 0.003% decrease, 73.3% decrease, 8.35% decrease, and 37.7% increase

Table 6-4. Optimization results: *minImpact*

	Optimal Conditions		$\mu(C_{C,out})$ (mmol/L)	$\sigma^2(C_{C,out})$ (mmol²/L²)	$C_{C,out}^{up}$ (mmol/L)	$C_{C,out}^{lw}$ (mmol/L)
Scenario 1A	***T* (K)**	474.30	3.000192	0.235622	3.789694	1.6826
	***v* (mm/s)**	8.68				
	***ρ* (nm)**	7.44				
Scenario 1B	***T* (K)**	475.00	3.000113	0.06295	3.473385	2.316576
	***v* (mm/s)**	6.00				
	***ρ* (nm)**	10.64				
Scenario 2A	***T* (K)**	480.20	3.000809	0.381307	4.113448	1.313281
	***v* (mm/s)**	6.52				
	***ρ* (nm)**	9.88				
Scenario 2B	***T* (K)**	481.70	3.00216	0.09045	3.63878	2.23217
	***v* (mm/s)**	6.00				
	***ρ* (nm)**	10.64				

in the expected value, variance, and upper and lower bounds respectively between the results for *Scenario 1B* and *Scenario 1A*. Similarly, the optimal statistical parameters for *Scenario 2A* and *Scenario 2B* differ by 0.045%, 76.3%, 11.5%, and 70.0% respectively. In total, approximately 7.7s were needed to run each robust optimization scenario for each of the uncertainty descriptions considered in this work. However, the computational costs to determine a single optimization operating point using PCE is orders of magnitude higher (1.20h, 2.39h, 1.19h, and 4.18h for *Scenarios 1A*, *1B*, *2A*, and *2B*, respectively), and consequently the computational cost to perform robust optimization using PCE would be several orders of magnitude larger (approximately 5 orders of magnitude larger for the reactor system considered in this work) than the cost for robust optimization using the DDMs, hence the significance and motivation to develop DDMs in the present analysis.

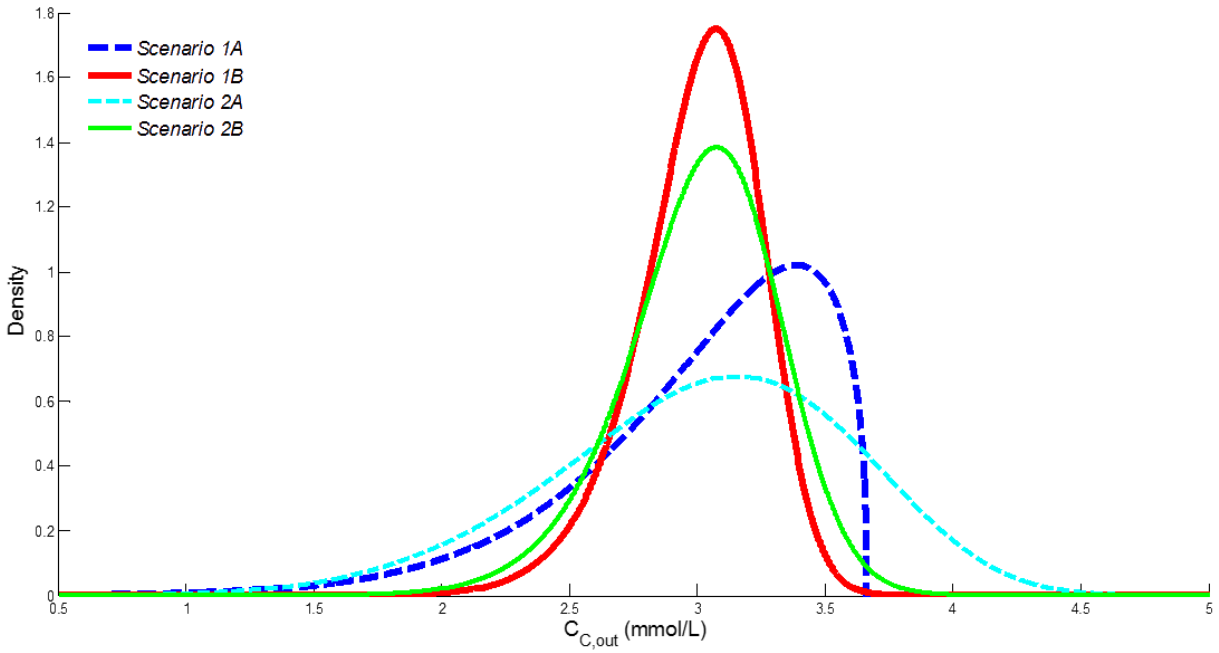

Figure 6-6. Predicted reactor performance and uncertainty variation in the outlet product concentration $C_{C,out}$ at the specific design and operating conditions that minimize the impact of parametric uncertainty on $C_{C,out}$ (*minImpact*) subject to the following uncertainty distributions: a) *Scenario 1A*, b) *Scenario 1B*, c) *Scenario 2A*, d) *Scenario 2B*

6.3 Summary

The objective of this chapter was to perform robust optimization on a multiscale catalytic flow reactor system that was subject to an unknown degree of catalyst deactivation due to poisoning and fouling. The effects of the poisoning and fouling mechanisms on the catalytic reactor performance were captured by assigning parametric uncertainty to key catalytic parameters (activation energies of desorption for species A, $E_{d,A}$ and reaction, E_r) in order to approximate the effects of catalytic deactivation on the reactor performance. In catalytic flow reactor systems, the rates of poisoning and fouling differ along the reactor length due to variation in the fluid species concentrations. The spatial variation in the catalytic deactivation processes was captured by assigning unique uncertainty descriptions to each of the key catalytic parameters at each tooth in the multiscale catalytic reactor model.

In this chapter, PCE expressions were constructed to efficiently propagate the catalytic parametric uncertainty through the multiscale reactor model. These formulations were used to perform uncertainty analysis on the multiscale reactor and to compare the effects of spatially-varying uncertainty due to catalyst

deactivation against spatially-uniform uncertainty descriptions. These results revealed that spatially-varying uncertainty has a substantial impact on the shape and the statistical parameters of the output variability. Subsequently, the spatially-varying uncertainty descriptions were implemented into a robust optimization formulation designed to maximize the productivity and minimize the impact of variability on the catalytic reactor system. In order to minimize the computational burden of calculating a PCE model with a large number of uncertainty realizations for each of the operating conditions considered in the optimization study, low-order statistical DDMs were developed to efficiently calculate the key statistics of the output variability over a range of values in the operating parameters. These DDMs enabled the robust optimization to perform orders of magnitude faster than if PCE had been used. The results from this study show that spatially-varying parametric uncertainty can have significant impact on the reactor productivity, and therefore, if it is not taken into consideration, can result in significant deviations in optimization studies.

Chapter 7
Distributional Uncertainty Analysis and Dynamic Optimization in Transient Multiscale Catalytic Reactors‡

The development and implementation of steady-state multiscale catalytic reactor models in the studies described in Chapters 5 and 6 were motivated by the fact that the operation of catalytic reactor systems is typically done under continuous conditions. These models provide efficient descriptions of the catalytic reactor performance through negligence of the transient reactor behaviour. Catalytic flow reactors, however, are time-dependent processes that are sensitive to dynamic variations in the system. The characteristics of a catalytic reaction mechanism can vary significantly between the initial system behaviour and the system behaviour at steady state.[144] In addition, model-based dynamic optimization and control studies require transient models that can capture the dynamic system behaviour subject to changes in the operating parameters. Therefore, it is necessary to evaluate the transient behaviour of the multiscale catalytic reactor system subject to dynamic system changes in addition to parametric uncertainty.

The objective of this chapter is to implement the transient multiscale single-pore reactor model described in Chapter 3 in order to perform dynamic analysis on the catalytic flow reactor system. To that extent, PSE is used to perform uncertainty analysis on the transient multiscale catalytic reactor model. This analysis is extended to observe the behaviour of the uncertain multiscale reactor model subject to dynamic changes in the system temperature. Furthermore, PCE is implemented to perform a pair of dynamic optimization studies designed to enhance the reactor productivity subject to parametric uncertainty. In the first study, dynamic optimization is applied to determine the optimal temperature profiles that maximize the reactor performance under uncertainty; while the second study seeks the optimal design and operating policies to achieve targeted performance specifications within a level of confidence subject to uncertainty.

This chapter is organized as follows. In Section 7.1, uncertainty analysis is performed in order to assess the spatial and temporal effects of parametric uncertainty in key system parameters on the transient multiscale catalytic reactor model. This section additionally considers the response of the multiscale catalytic reactor system under uncertainty subject to transient changes in the reactor temperature. Section 7.2 then presents the two different dynamic optimization case studies that were performed on the transient reactor system.

‡ The contents of the first half of this chapter have been previously presented at the 11th IFAC Symposion of Dynamics and Control of Process Systems, including Biosystems (DYCOPS-CAB 2016),[27] and the contents of the second half of this chapter has been accepted for publication by the Journal of Process Control (JPC).[28]

7.1 Spatial and Transient Uncertainty Analysis using Power Series Expansions

The behaviour of a catalytic reactor system at steady state can differ significantly from the initial reactor behaviour. Thus, it is important to study the effects of parametric uncertainty on the catalytic reactor system as a function of time and space in order to understand its transient effects on the reactor performance. For this analysis, uncertainty was propagated through the multiscale catalytic reactor model using the PSE approach described in Chapter 4. Uncertainty was applied to key kinetic parameters $k_{a,B}$, $E_{d,B}$, and E_r as well as to the axial fluid velocity, v. These uncertainties were assigned normal distributions with the following mean (nominal) values:

$$\left[\mu\left(k_{a,B}\right), \mu\left(E_{d,B}\right), \mu(E_r), \mu(v)\right] = [1;\ 100;\ 57;\ 0.01] \tag{7-1}$$

The covariance matrix for these parameters is as follows:

$$\sigma^2\left(k_{a,A}, E_{d,A}, E_r, u\right) = \begin{bmatrix} 0.04 & 0.002 & 0.002 & 0 \\ 0.002 & 16 & 2.5992 & 0 \\ 0.002 & 2.5992 & 5.1984 & 0 \\ 0 & 0 & 0 & 4 \times 10^{-6} \end{bmatrix} \tag{7-2}$$

Second-order PSEs were used to propagate the parametric uncertainty into the concentrations of product species C at multiple points both in time and along the spatial domains in the reactor. Preliminary simulations showed that this order in the PSE approximation is suitable to capture the uncertain effects considered in this analysis. Finite difference approximations were used to determine the sensitivities $\mathbf{J}(x, y, t)$ and $\mathbf{M}(x, y, t)$ for the PSE models using averaged results obtained from multiple independent simulations of the primary multiscale reactor model using a 30x30 kMC lattice size. For this analysis, the catalyst surface domain was subdivided by the gap-tooth method into eight equidistantly-spaced teeth; increasing the number of teeth in the model discretization did not significantly improve the accuracy in the results. The probabilistic bounds for the variation in the concentration of species C were generated from the PSE models at a confidence interval of $\alpha = 0.27\%$, which corresponds to the bounds of the third standard deviation for a normal PDF.

7.1.1 Uncertainty Analysis at Constant Temperature

The effects of parameter uncertainty were analysed for the single-pore catalytic flow reactor at a temperature of $T = 425$K. The time-dependent reactor performance was evaluated through the product (species C) concentration at the pore outlet $C_{C,out}(t)$ for a total batch time of $t_{final} = 8$s subdivided into eight different time intervals spaced 1s apart (i.e. $U = 1$, $V = 1$, and $W = 8$ in the PSE algorithm). Furthermore, the product concentration was assessed along the catalyst surface at t_{final} as a function of the axial length, i.e. $C_C(x, \rho, 8)$, where (i.e. $U = 101$, $V = 1$, and $W = 1$ in the PSE algorithm). Figure 7-1 shows the time-dependent PSE-based probabilistic bounds for $C_{C,out}(t)$ evaluated at a confidence interval of $\alpha = 0.27\%$. This result shows that the concentration of species C rapidly increases at the beginning of the reaction before slowing down and reaching steady-state at around 4s. Additionally, the deviation between the upper and lower probabilistic bounds demonstrates the significant effect of parametric uncertainty on the overall reactor performance, as the product concentration varies from 0.4mmol/L to 3.5mmol/L at steady-state. Figure 7-1 also shows the concentration profiles for 500 random MC simulations sampled from the uncertain parameter distributions, as well as the nominal parameter concentration profile, using the primary multiscale model. As demonstrated, the PSE-based bounds at $\alpha = 0.27\%$ are able to adequately envelop the variation in product concentrations that exist as a result of parameter uncertainty.

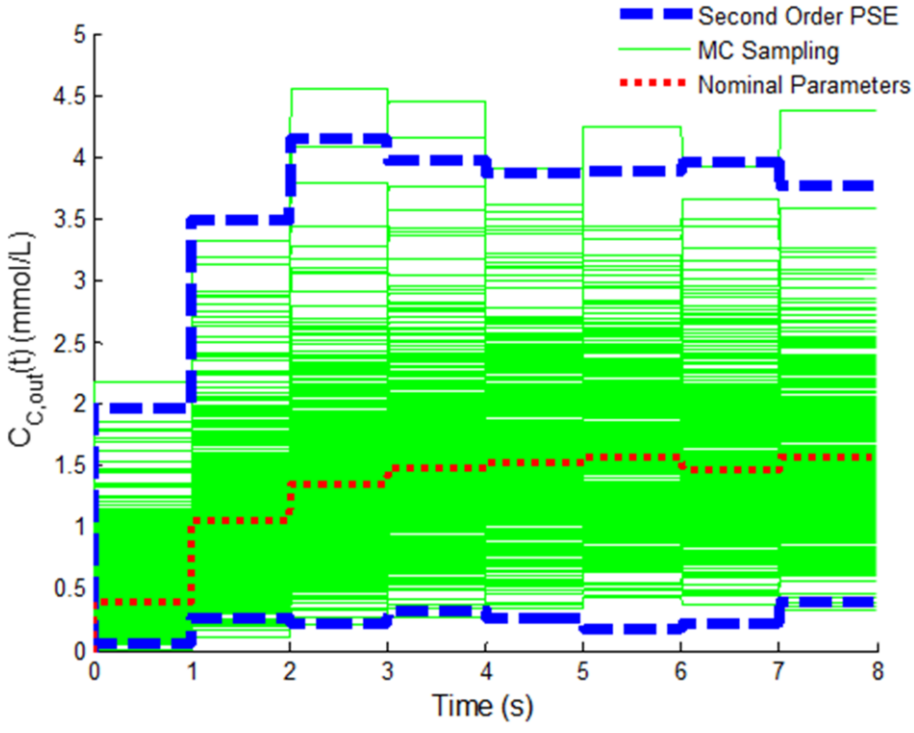

Figure 7-1. Bounds on the concentration of species C, $C_{C.out}(t)$, estimated from second-order PSEs.

This shows that, when compared to the primary reactor model, the second-order PSE is capable of providing sufficiently accurate bounds. The uncertainty analysis using 500 MC simulations of the primary model required approximately 790s of CPU time. Following the determination of the PSE model, the PSE simulation required 2s to compute the bounds; thus, demonstrating its superiority over the standard MC sampling method using the primary model.

Figure 7-2 presents the PSE-based probabilistic bounds for the axial concentration profiles of product C along the catalyst surface at the final batch time. This figure also shows the concentration profiles for 500 random MC simulations sampled from the uncertain parameter distributions in addition to the nominal parameter concentration profile. As demonstrated in the plot, the concentration profiles are adequately covered by the PSE-based probabilistic bounds similar to Figure 7-1. By inspecting the temporal and spatial evolution of product C from Figures 7-1 and 7-2 using only nominal (mean) values in the uncertain parameters (red dotted lines in the Figures), it is clear that parameter uncertainty has a nonlinear effect on this output. This is expected due to the Arrhenius relationship between the rates of desorption/reaction and the uncertain activation energies. Fig. 7-2 also demonstrates the propagation of the effects of parametric uncertainty along the reactor length, which results in substantially wider variation of the product

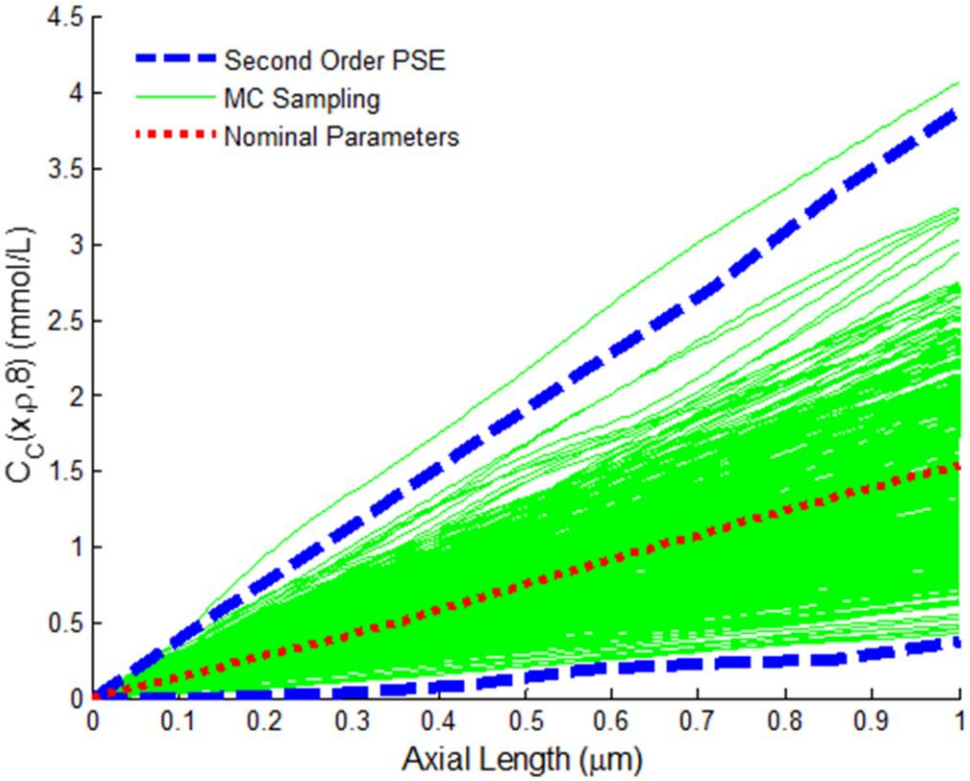

Figure 7-2. Bounds on the concentration of species C, $C_C(x,\rho,8)$, estimated from second-order PSEs.

concentration at the pore outlet than at the pore inlet. Fig. 7-1 demonstrates a similar trend, where the effects of uncertainty result in significantly wider variation in concentrations of product C.

7.1.2 Uncertainty Analysis using Step Changes in Temperature

The aim of this section is to analyse the effect of temperature changes on the present catalyst reactor multiscale model. Accordingly, uncertainty analysis was performed on a single-pore catalytic flow reactor under step changes in temperature. Note that due to the absence of the heat transport equation, the catalytic reaction model would not be able to account for the thermal lag that would occur when the temperature was changed. Consequently, changes in the system temperature were only considered along the catalyst surface, such that the fluid phase of the catalytic reactor could be assumed isothermal. This assumption was made in order to reduce the computational cost of the optimization. The temperature was initialized at $T = 425\text{K}$; at times $t = 8\text{s}$ and $t = 17\text{s}$, the reactor temperature was changed to $T = 375\text{K}$ and $T = 475\text{K}$, respectively. Note that the large change in temperature was utilized for the purpose of illustrating the effects on the output concentration; however, smaller temperature changes would be expected to occur during normal operation. The temperature changes were implemented once the reactor had reached steady-state. The reactor's performance under these changes was evaluated every second for a total batch time of $t_{final} = 30\text{s}$, therefore $U = 1$, $V = 1$, and $W = 30$ in the PSE algorithm.

Figure 7-3 presents the PSE-based probabilistic bounds evaluated at $\alpha = 0.27\%$ for the concentration of species C at the reactor outlet as a function of time. As expected, the variation in the concentration due to parametric uncertainty is directly correlated to the quantity of species C produced in the reactor, i.e. wider variability is observed when large amounts of product C are produced and vice-versa. Furthermore, the concentration of the product increases in a nonlinear fashion for higher reactor temperatures, which can be attributed to its role in the Arrhenius expressions in the rates of desorption and reaction. Note that when the temperature is raised, there is an initial substantial increase in the product concentration, followed by a decrease to a new steady-state value. In order to investigate this behaviour, the quantity of surface reactant ensembles was examined for each kMC surface lattice at three different intervals: before, during, and after the temperature increase. Before the temperature increase (i.e. at $T = 375\text{K}$), the rate of reaction is relatively small, and as a consequence, there are a large number of possible surface reactant ensembles available. When the temperature is increased (i.e. from 375K to 475K), the rate of reaction increases accordingly, and due to the large number of surface reactant ensembles, the rate of production of species C increases substantially. The number of surface reactant ensembles is quickly diminished due to the high reaction rates, reducing the production of species C until the reactor attains the new steady-state. The opposite behaviour was observed when the temperature is decreased. Figure 7-3 also shows the concentration

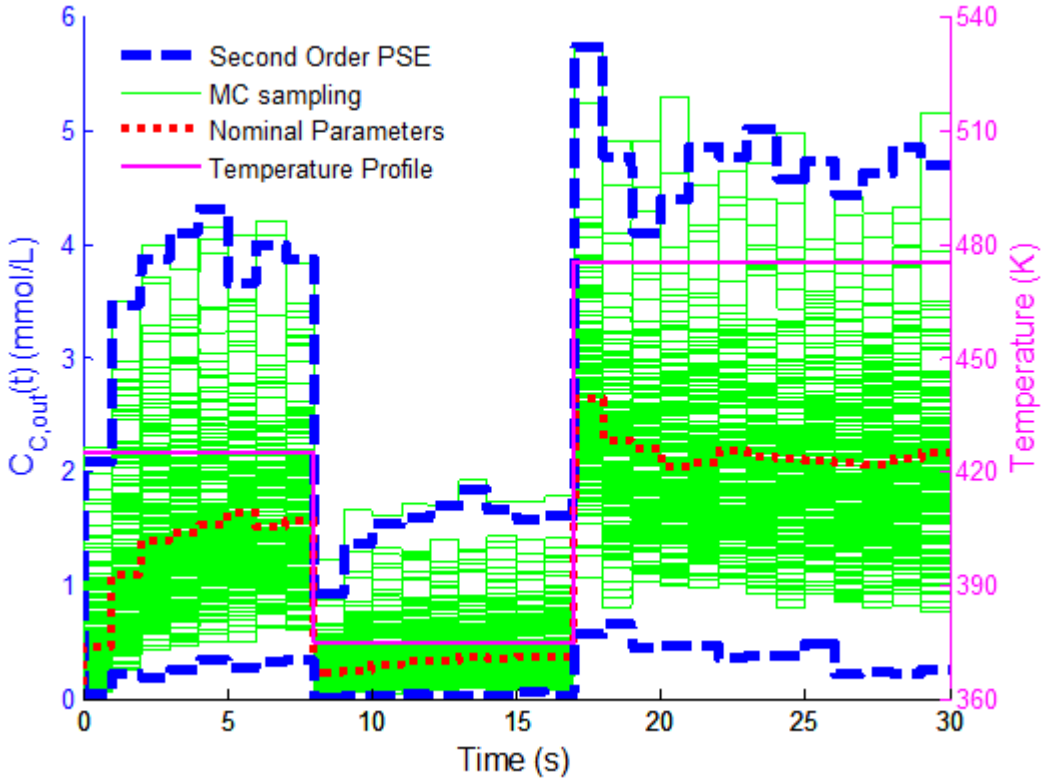

Figure 7-3. Bounds on the concentration of species C, $C_{C,out}(t)$, estimated from second-order PSE.

profiles for 500 random MC simulations sampled from the uncertain parameter distributions, as well as the nominal parameter concentration profile, using the primary model. This uncertainty propagation approach required a CPU time of 3,600s whereas the PSE bounds were computed in significantly less time, requiring only 6s of CPU time. As shown in Figure 7-3, the PSE bounds are able to cover the variation in the MC sampling concentration profiles. Note that the concentration profiles are shifted substantially closer to the upper bound, demonstrating the nonlinearity of the system.

Figure 7-4 displays the PSE-based PDFs for the effects of parametric uncertainty on the axial concentration profiles for product C at different time intervals, i.e. $C_C(x, \rho, t_{SS})$. Here, $t_{SS} \in \{6\text{s}, 15\text{s}, 30\text{s}\}$ corresponds to steady state batch times for temperatures $T = 425\text{K}$, $T = 375\text{K}$, and $T = 475\text{K}$, respectively. For this analysis, $U = 8$, $V = 1$, and $W = 3$ in the PSE algorithm. As shown in this figure, the effects of uncertainty propagate along the axial reactor length as the product concentration increases. Furthermore, the distributions in the output are notably different for the different axial lengths and temperatures considered; in addition, the PDFs become wider as more species C is produced.

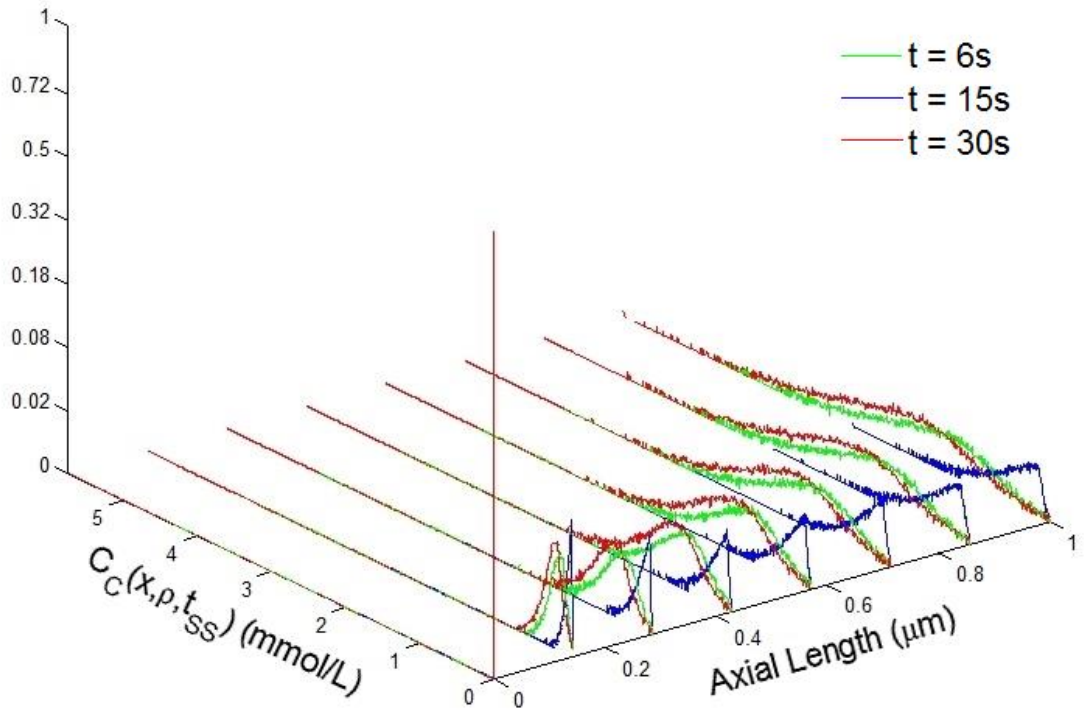

Figure 7-4. PDF of the axial concentration profiles for species C, $C_C(x, \rho, t_{SS})$.

7.2 Dynamic Optimization Studies

The behaviour of the single-pore catalytic flow reactor is subject to a number of design and operational parameters that can be adjusted *a priori* or online respectively in order to improve reactor's performance. The aim of this section is to present a set of dynamic optimization studies that illustrate the benefits of implementing suitable operating policies and proper selection of design parameters for improvement of spatially-dependent multiscale systems under uncertainty. For both case studies, second-order PCE was implemented to propagate uncertainty to the reactor outlet product concentrations. Uncertainty was considered in the activation energy of desorption for species A, $E_{d,A}$) and the pore radius, ρ. The uncertainty in the activation energy, $E_{d,A}$, was assumed to vary along the reactor length due to catalyst deactivation from poisoning and fouling. Subsequently, unique uncertainty profiles were applied to $E_{d,A}$ at each tooth considered in the gap-tooth model. For these case studies, the reactor was sub-divided into seven teeth ($n_{teeth} = 7$), therefore $I = 7$ and $J = 1$ for the PCE model. The uncertainty was assumed to remain constant as a function of time, and consequently $K = 1$. For both case studies, the uncertainty in each parameter was assumed normally-distributed as described in Equation (4-15) of Chapter 4. The dynamic optimization case studies are described below.

7.2.1 Case Study 1: Optimal Operating Policies

The performance of a catalytic reactor is significantly affected by the temperature changes imposed on the reactor system. Thus, adjusting this variable on-line can result in attractive operating policies that can maximize reactor productivity. In addition, product variability due to parametric uncertainty needs to be considered to produce robust operating strategies that can account for this phenomena. The aim of this case study is to perform dynamic optimization on the single-pore catalytic flow reactor model to search for the temperature profile that enhances reactor productivity while accounting for uncertainty in the multiscale model parameters. The dynamic optimization formulation proposed in this work to identify the optimal temperature profiles is as follows:

$$\max_{T\in\mathbf{T}} \mu\left(C_{C,out}(t_{final})\right)$$

s.t.

Multiscale model, Eqs. (3-1)-(3-24)

Uncertain parameter descriptions, Eq. (4-15)

PCE model, Eq. (4-14)

$$T_{min} < \mathbf{T} < T_{max}$$

$$\mathbf{T} = [T(\Delta t_T), \dots, T(N_T \Delta t_T)]$$

$$t \in [0, \Delta t_T, 2\Delta t_T, 3\Delta t_T, \dots N_T \Delta t_T]$$

$$t_{final} = N_T \Delta t_T \quad (7\text{-}3)$$

As shown above, parametric uncertainty was propagated in the activation energy of desorption for species A as a function of the axial length ($E_{d,A}(x_{ud,i}, \rho)$) and in the pore radius (ρ) using the uncertainty descriptions shown in Eq. (4-15). Thus, a set of eight uncertainty descriptions were considered in this analysis (seven uncertainty descriptions for $E_{d,A}(x_{ud,i}, \rho)$ and one uncertainty description for ρ). The reactor performance was evaluated solely through the expected outlet concentration of product species C, $\mu\left(c_{C,out}(t_{final})\right)$, after a total reaction time of $t_{final} = 12$s. The temperature was allowed to vary at time intervals of $\Delta t_T = 3$s. For consistency and for the sake of comparison between the different temperature profiles implemented, the reactor temperature was set at the nominal value $T = 460$K for 3s so that the system would be initialized from the same operating condition before the temperature was allowed to vary. Note that varying the initial reactor temperature would provide meaningful information on the effects of the initial temperature on the reactor behaviour, however this is beyond the scope of this work.

Subsequently, the system temperature was allowed to change three different times for each scenario for a total reaction time of $t_{final} = 12$s, thus for this analysis, $N_T = 4$ in Eq. (7-3). Increasing the total reaction time did not improve the results significantly but rather produced unnecessary additional computational costs. In addition, the temperature was constrained between upper and lower bounds of $T_{max} = 480$K and $T_{min} = 440$K, respectively. The results obtained from the dynamic optimization formulation in Eq. (7-3) were contrasted with the reactor performance under a constant temperature profile of $T = 460$K (*constTemp*). In order to reduce the computational burden associated with dynamic optimization schemes applied to multiscale systems, the PCE scheme discussed in Chapter 4 was applied for uncertainty quantification as depicted in Eq. (7-3). That is, for each temperature profile tested by the dynamic optimization algorithm, a second-order PCE model was developed and implemented to evaluate $\mu\left(C_{C,out}(t_{final})\right)$. Additionally, the temperature was limited to a discrete number of temperature values between T_{min} and T_{max} to further decrease the computational costs.

Table 7-1 compares the statistical properties and probabilistic bounds evaluated at $\alpha = 2\%$ confidence between a constant temperature profile (*constTemp*) and the optimal temperature profile (*meanConc*) obtained from the solution of Eq. (7-3). The actual temperature profile obtained from the dynamic

Table 7-1. Case Study 1: Results

Scenarios	**Temperature Profile**	$\mu\left(C_{C,out}(t_{final})\right)$ **(mM)**	$\sigma^2\left(C_{C,out}(t_{final})\right)$ **(mM^2)**	$C^{up}_{C,out}(t_{final})$ **(mM)**	$C^{lw}_{C,out}(t_{final})$ **(mM)**
Constant Temperature (constTemp)	$T = 460K$	2.0483	0.2442	3.6223	1.2654
Maximum Temperature (maxTemp)	$T = 460K$ $\rightarrow 480K$	2.0839	0.2202	3.4578	1.3029
Dynamic Optimization (meanConc)	$T = 460K$ $\rightarrow 480K$ $\rightarrow 440K$ $\rightarrow 480K$	2.1217	0.2697	3.8859	1.3476
Dynamic Optimization (minVar)	$T = 460K$ $\rightarrow 440K$ $\rightarrow 460K$ $\rightarrow 440K$	1.7473	0.1493	2.9071	1.1207

optimization problem presented in Eq. (7-3) is also described in Table 7-1. Additionally, the uncertainty effects on the outlet product concentration as determined through PCE and MC sampling over 5,000 points are shown in Figure 7-5a and 7-5b using the *meanConc* and *constTemp* temperature profiles, respectively. As shown in these panels, PCE is capable of accurately capturing the outlet variation due to uncertainty using a constant or a time-dependent temperature profile. As illustrated by the results in Table 7-1, the temperature profile that needs to be implemented on-line to maximize the expected product concentration alternates between the highest and the lowest temperature values ($T = 480\text{K}$ and $T = 440\text{K}$, respectively), ending on the maximum temperature of $T = 480\text{K}$. It is expected that up to a certain temperature value, higher reactor temperatures would produce higher product concentrations, as discussed in Chapter 5. Note that the optimal temperature profile invokes on-line changes in temperature, which implies that transient temperature profiles can provide improved results over a static temperature profile. To validate this observation, Table 7-1 includes the statistical parameters obtained when the reactor temperature profile was held constant at the maximum temperature, $T = 480\text{K}$ (*maxTemp*). Figure 7-5c illustrates the variation in the outlet product concentration due to uncertainty for the *maxTemp* condition, which demonstrates that PCE is able to capture the output response under uncertainty with reasonable accuracy. Furthermore, Figure 7-6 compares the PDFs obtained from the *constTemp*, *maxTemp*, and *meanConc* temperature profiles as well as their expected values and probabilistic bounds ($\alpha = 2\%$). As shown in Table 7-1 and Figure 7-6,

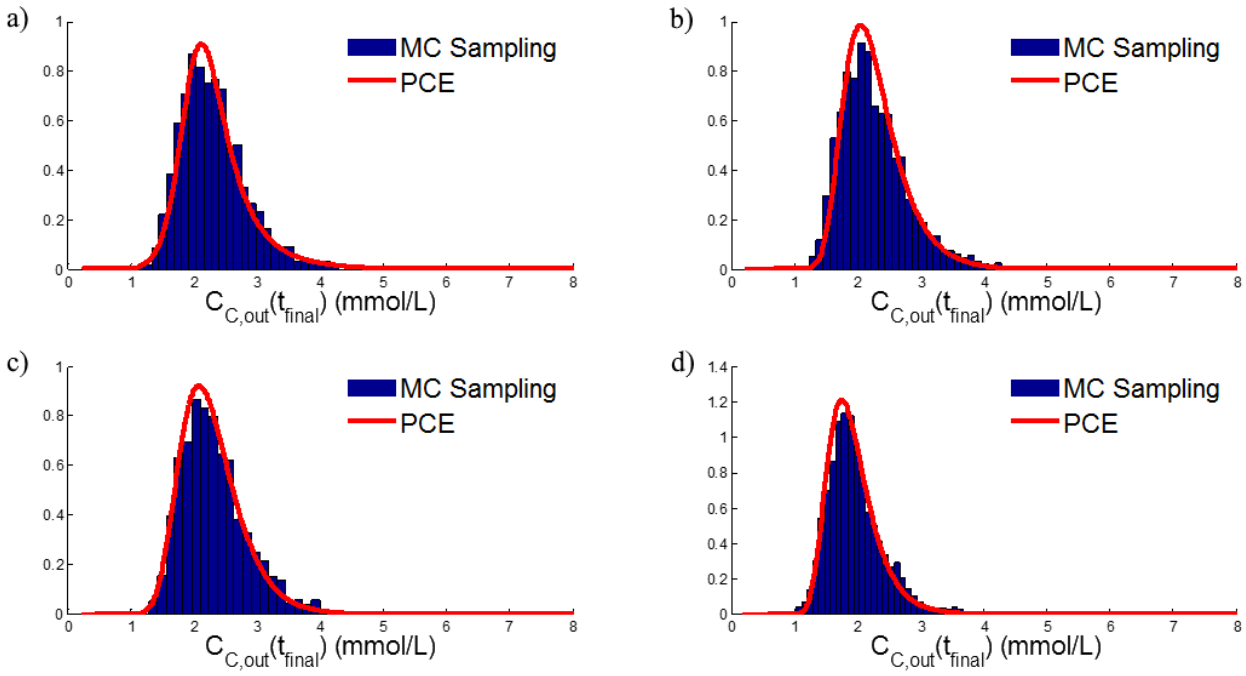

Figure 7-5. PDFs of the concentration of species C at the reactor outlet ($x = L, y = 0$), $t_{final} = 12s$: for (a) *meanConc*; (b) *constTemp*; (c) *maxTemp*; and (d) *minVariate*.

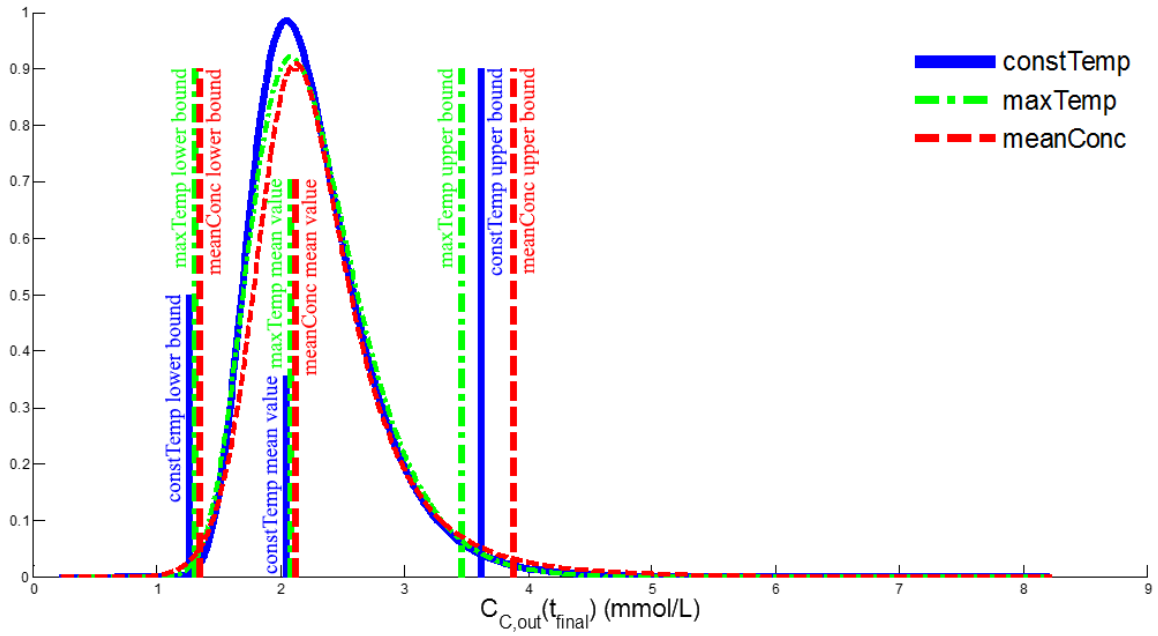

Figure 7-6. PDFs and probabilistic bounds of the concentration of species C at the reactor outlet $(x = L, y = 0)$ at $t_{final} = 12s$ for *meanConc* (red), *constTemp* (blue), and *maxTemp* (green).

the *meanConc* temperature profile offers improvements in the expected value of the outlet product concentration over the static temperature profiles. Specifically, there is a 4% increase in the expected concentration of product C over the nominal profile ($T = 460$K), and a 2% increase over the static high-temperature profile ($T = 480$K). Table 7-1 and Figure 7-6 reveal that the differences are most noticeable in the upper bounds, where the *meanConc* profile provides a 7% increase over the *constTemp* profile, and a 12% increase over the *maxTemp* profile. These results demonstrate that the productivity of the single-pore catalytic flow reactor can be optimized by performing on-line adjustments of the system temperature while taking parameter uncertainty into account.

To properly explain the benefits of performing on-line temperature adjustments on the reactor production rates, it is necessary to understand the impact of the changing temperature on the catalyst kinetic behaviour. In the previous section, it was observed that when the temperature is altered, there is a sharp change in the reactor concentration before the system returns to its new steady state. These sharp changes are due to the state of the catalyst surface under the various temperatures. Although this initial spike in concentration does reduce as the catalyst surface approaches the new steady state, the rate of reaction following the temperature change remains larger than the rate of reaction from a constant temperature profile if the system was initialized at the same temperature. The opposite behaviour is observed when the temperature is lowered. This analysis demonstrates that toggling the system temperature to a lower value will populate the catalyst surface with a larger number of surface reactant ensembles, which results in an

overall increase in the rate of production once the temperature is raised once again. The results in Table 7-1 also indicate that higher expected product concentrations are paired with larger product variability due to uncertainty. For instance, the outlet product concentration of the reactor under *meanConc* conditions has a 10% larger variance than the outlet product concentration of the reactor under the *constTemp* profile, as illustrated in Table 7-1. To further explore this behaviour, an additional dynamic optimization study was performed to determine the temperature profile that minimizes the variability in the product concentrations, and therefore decreases the impact of parametric uncertainty on the reactor productivity. This optimization problem is as follows:

$$\min_{T \in \mathbf{T}} \sigma^2 \left(C_{C,out}(t_{final}) \right)$$

s.t.

Multiscale model, Eqs. (3-1)-(3-24)

Uncertain parameter descriptions, Eq. (4-15)

PCE model, Eq. (4-14)

$$T_{min} < \mathbf{T} < T_{max}$$

$$\mathbf{T} = [T(\Delta t_T), \dots, T(N_T \Delta t_T)]$$

$$t \in [0, \Delta t_T, 2\Delta t_T, 3\Delta t_T, \dots N_T \Delta t_T]$$

$$t_{final} = N_T \Delta t_T \tag{7-4}$$

For the formulation proposed above, the catalytic reactor model was subjected to the same parametric uncertainty descriptions and specifications considered in the problem presented in Eq. (7-3). The results for this dynamic optimization problem (*minVar*) have been compiled in Table 7-1 and the variation in the outlet product concentration is illustrated in Figure 7-5d. As shown in Table 7-1 (*minVar*), minimal variation in the product concentrations due to uncertainty can be achieved by implementing the lowest possible temperature, raising it, and then lowering it to the lowest value once again. Implementation of this temperature profile produced a 39% decrease in the variation of the outlet product concentration over the *ConstTemp* results and a 45% decrease in the variation of the outlet product concentration over the *meanConc* results, as shown in Table 7-1. Additionally, implementing the *minVar* temperature profile results in an 18% decrease in the expected value of the outlet product concentration as compared to the *meanConc* results. These results reflect that the effects of uncertainty are minimized when the outlet product concentration is minimized. Additionally, they confirm that decreasing the reactor temperature produces a net decrease in the expected product concentration, therefore producing minimal variance. Additional

optimization formulations that weights the mean and variance in the output concentration can be implemented similar to the steady-state case studies implemented in Chapters 5 and 6, but they were not implemented on the transient multiscale model for brevity.

7.2.2 Case Study 2: Optimal design and operating policies

The production of chemical species within a catalytic flow reactor requires precise on-line control of the fine-scale events to attain desired product specifications. Additionally, the reactor design is also relevant to ensure that the reactor is capable of achieving targeted product concentrations. The aim of this case study is to illustrate the benefits of performing simultaneous design and on-line control for a multiscale system under uncertainty. In particular, this case study aims to simultaneously identify the optimal design parameter and operating policies on the catalytic reactor multiscale system that complies with a product target concentration under uncertainty. The problem under consideration can be stated as follows:

$$\min_{T\in\mathbf{T},L} \text{Length } (L)$$

s.t.

$$C_{C,out}^{lw}\left(t_{final}\right) \geq C_{C,out}^{*}$$

Multiscale model, Eqs. (3-1)-(3-24)

Uncertain parameter descriptions, Eq. (4-15)

PCE model, Eq. (4-14)

$$T_{min} < \mathbf{T} < T_{max}$$

$$\mathbf{T} = [T(\Delta t_T), \dots, T(N_T \Delta t_T)]$$

$$t \in [0, \Delta t_T, 2\Delta t_T, 3\Delta t_T, \dots N_T \Delta t_T]$$

$$t_{final} = N_T \Delta t_T \qquad (7\text{-}5)$$

where $C_{C,out}^{lw}(t_{final})$ is determined at 99% confidence ($\alpha = 2\%$ such that $P\left(C_{C,out} \geq C_{C,out}^{*}\right) = 0.99$) and $C_{C,out}^{*}$ denotes the targeted set point for the outlet product species concentration. As shown in Eq. (7-5), the dynamic performance of the reactor was realized through on-line adjustments of the reactor temperature at specific time points akin to the previous case study. Additionally, reactor design was simultaneously performed by searching for the optimal pore length *L* to use during reactor assembly. As in the previous case study, the variation in temperature was limited to discrete intervals between $T_{min} = 440$K

and $T_{max} = 480$K and the temperature was allowed to change every $\Delta t_T = 3$s for a total reaction time of $t_{final} = 12$s (thus $N_T = 4$ in Eq. (7-5) for this analysis). Additionally, the uncertainty descriptions considered in this case study are the same as those considered previously (Section 7.2.1) and were similarly propagated using second-order PCE. Note that the uncertainty in $E_{d,A}$ was still considered to vary axially at each of the seven teeth implemented in the gap-tooth model, and that the number of teeth was not changed for the differing reactor pore lengths. Alternatively, the gap spacing was modified so that the seven teeth remained equidistantly spaced and yet still spanned the entire length of the reactor pore.

The present case study considers two different scenarios with set points of $C^*_{C,out} = 1.3$mmol/L (scenario 1) and $C^*_{C,out} = 2.7$mmol/L (scenario 2), respectively. The optimal temperature profiles and pore lengths obtained for each scenario are presented in Table 7-2. The table also lists the statistical parameters for both scenarios, i.e. mean, variance, and bounds at a 2% confidence level. In addition, the red circles (o) in Figure 7-7a and Figure 7-7b compare the variation in the product concentration over 100 random realizations of the multiscale model using the optimal design and operating policies obtained for scenario 1 (*s1_Opt*) and scenario 2 (*s2_Opt*), respectively. As shown in Figure 7-7, the identified conditions for both scenarios only violate their respective set points one time out of 100, which validates the specifications outlined in the dynamic optimization problem. To further investigate the advantages of the simultaneous

Table 7-2. Case Study 2: Results

Scenarios	**Temperature Profile**	**Pore Length**	$\mu\left(C_{C,out}(t_{final})\right)$ **(mmol/L)**	$\sigma^2\left(C_{C,out}(t_{final})\right)$ **(mmol/L²/L²)**	$C^{up}_{C,out}(t_{final})$ **(mmol/L)**	$C^{lw}_{C,out}(t_{final})$ **(mmol/L)**
s1_Opt ($C^*_{C,out} = 1.3$ mM)	$T = 460K$ → $460K$ → $440K$ → $480K$	1 μm	2.1043	0.2370	3.5367	1.2974
s1_constT ($C^*_{C,out} = 1.3$ mM)	$T = 460K$ → $480K$	1 μm	2.0541	0.2367	3.4890	1.2220
s2_Opt ($C^*_{C,out} = 2.7$ mM)	$T = 460K$ → $440K$ → $460K$ → $480K$	2 μm	4.2064	1.0742	7.5002	2.6824
s2_constT ($C^*_{C,out} = 2.7$ mM)	$T = 460K$ → $480K$	2 μm	4.1879	1.0026	7.2534	2.4940
nomParams	$T = 460K$	1 μm	2.0483	0.2442	3.6223	1.2654

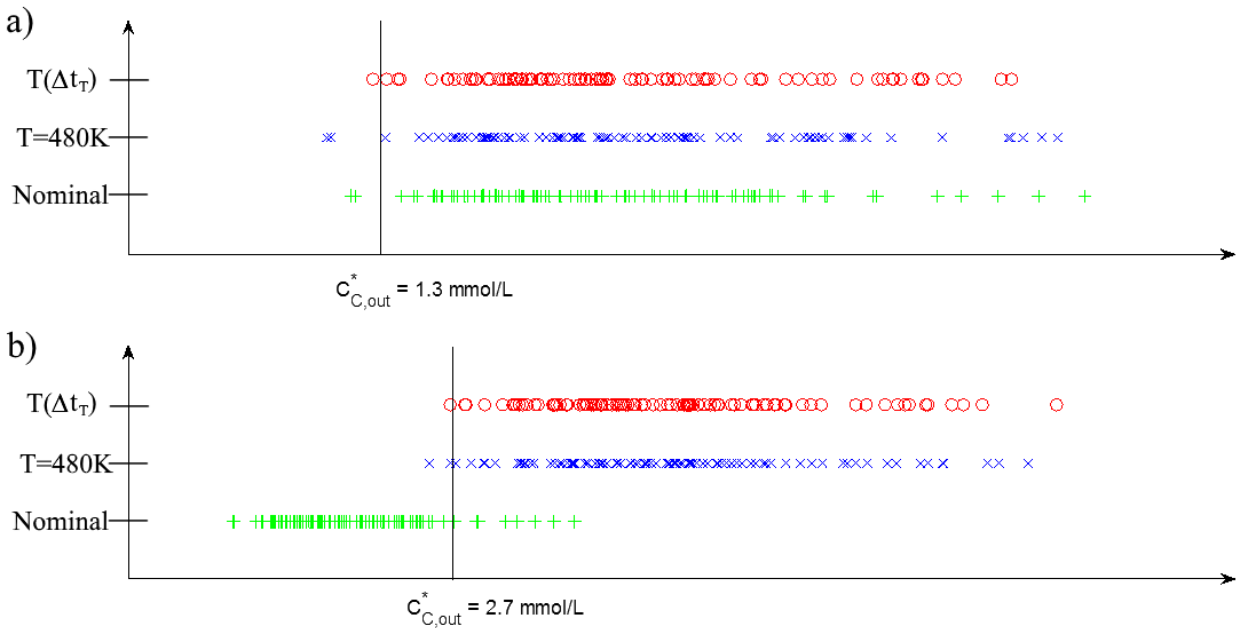

Figure 7-7. Validation of the reactor outlet product concentrations C due to parametric uncertainty: (a) Scenario 1 ($C^*_{C,out} = 1.3\ mM$); (b) Scenario 2 ($C^*_{C,out} = 2.7\ mM$). o: *s1_Opt*, *s2_Opt*; x: *s1_constT*, *s2_constT*; +: *nomParams*.

design and on-line control approach, the behaviour of the reactor was tested under a constant temperature profile $T = 480$K using the pore lengths determined from the results of *s1_Opt* and *s2_Opt*. That is, for the first and second scenario under constant temperature (*s1_constT* and *s2_constT*), the reactor's length (L) was set to 1 μm and 2 μm, respectively, as shown in Table 7-2. Additionally, the reactor behaviour was investigated under the nominal conditions reported in Table 3-1 (*nomParams*). As shown in Figure 7-7a and Figure 7-7b, the *s1_constT* and *s2_constT* results violate the set points two times out of 100 on average. In contrast, the *nomParams* results violate the set points 2% of the time for scenario 1, and 92% of the time for scenario 2. Table 7-2 shows a 6% smaller lower bound ($C^{lw}_{C,out}(t_{final})$) between *s1_opt* and *s1_constT* as well as an 8% smaller lower bound between *s2_opt* and *s2_constT*. The lower bounds obtained from *s1_Opt* and *s2_Opt* furthermore differ by 3% and 112% respectively from the lower bounds obtained in the *nomParams* scenario. These results further demonstrate the benefits of searching for an optimal design and temperature profile scheme for process improvement.

7.3 Summary

This chapter explored the effects of parametric uncertainty on the transient behaviour of the catalytic reactor system and implemented these effects into dynamic optimization studies. To that extent, uncertainty

analysis was performed on the dynamic multiscale catalytic flow reactor model using PSE to propagate key system parameter uncertainty to the model outputs as a function of time and space. These results illustrated that uncertainty has a substantial effect on the predicted reactor behaviour as it evolves in time and in space. The uncertainty analysis was further extended to analyze the uncertainty impact on the reactor performance subject to transient changes in the local temperature along the catalyst surface. In addition to re-enforcing that parametric uncertainty can have substantial effects on the system behaviour, these results provided insight into the catalytic reactor performance under changes in the system temperature. Subsequently, the transient multiscale reactor was implemented into dynamic optimization formulations that sought to identify the optimal reactor design and operating policies that maximize the reactor performance subject to uncertainty. For these optimization studies, PCE was used to propagate spatially-varying parametric uncertainty through the transient reactor system. The first study aimed to identify the optimal temperature trajectory that would maximize the product concentration of the reactor system under uncertainty, while the second study aimed to simultaneously identify optimal operating policies and reactor design conditions that allow the reactor to meet targeted performance criterion within a certain degree of certainty. These studies revealed that by alternating the temperature profile between high and low temperature values, it was possible to improve the yield of the catalytic reactor system, thus illustrating how transient operational strategies can improve the reactor performance over steady-state based analyses. These studies additionally illustrated how the use of uncertainty implementation techniques such as PCE can be used to overcome reactor performance loss due to uncertainty.

Chapter 8
Conclusions and Recommendations

Catalytic reactor systems play a crucial role in the majority of industrial chemical production processes. This has motivated the need for robust optimization schemes to maximize the catalytic reactor productivity. These optimization processes are most readily implemented using model-based approaches, whose performances are regrettably limited by parametric uncertainty and model-plant mismatch. The objective of this research was to study the impact of parametric uncertainty on a multiscale catalytic flow reactor model and to subsequently implement uncertainty propagation techniques to perform efficient reactor optimization. The behaviour of the catalytic reactor system was captured using multiscale modeling approaches that combined continuum transport equations with kinetic models such as lattice-based kMC that simulate each of the reactor phenomena on the relevant scales on which they occur. In order to reduce the computational costs, low-order PSE and PCE series expansions were developed to efficiently propagate parametric uncertainty through the multiscale catalytic reactor model. These models were used to capture the variability and determine the key statistical parameters in the reactor system outputs that result from uncertainty in the system parameters.

8.1 Conclusions

Catalytic flow reactor models contain numerous physical and kinetic parameters subject to uncertainty due to difficulties in measuring their values from experimental results. These parametric uncertainties can cause substantial deviations between the predicted outputs of the reactor models and the practical reactor behaviour. As a result, it is crucial to study the impact of uncertainty in the system parameters on the catalytic reactor performance and to accommodate for uncertainty when performing model-based optimization and process improvement studies. In Chapter 5, a rigorous uncertainty analysis was performed in order to analyze the effects of uncertainty in a wide selection of key system parameters on the behaviour of the multiscale single-pore reactor model. This study analyzed the impact of accounting for uncertainty in an increasing number of system parameters as it affects the variability in the output species concentrations of the catalytic reactor system. The results of these analyses emphasized that uncertainty has significant effects on the catalytic reactor behaviour. Furthermore, they illustrated how parametric uncertainty propagates in space through flow-style reactor systems. The need to accommodate for all uncertain parameters in model-based reactor studies was illustrated by the continued significance of uncertainty as the number of uncertain parameters was increased.

It can be computationally challenging, however, to propagate uncertainty through each uncertain system parameter when performing optimization and process improvement studies. Consequently, the results of the uncertainty analyses in Chapter 5 can be used to identify the key uncertain system parameters that have the largest impact on the output variability. These uncertainty descriptions were subsequently implemented into a robust optimization formulation that sought to maximize the catalytic reactor performance subject to uncertainty in the most sensitive key system parameters. The results from the robust optimization studies demonstrated that taking parametric uncertainty into account can substantially impact the operating conditions that produce the most optimal catalytic reactor performance. Furthermore, the optimization studies revealed that the variability in the reactor product concentrations could be reduced at the cost of lower reactor productivity.

Catalytic reactor systems are challenged by catalyst deactivation due to fouling and poisoning. These processes physically block catalyst sites and chemically interact with the catalyst to decrease its productivity. Catalyst fouling and poisoning is primarily known to affect the number of available catalyst surface sites, however it is difficult to account for catalyst deactivation through this parameter without directly simulating the kinetic deactivation events within the catalyst surface model. Alternatively, the effects of catalytic deactivation on the behaviour of a catalytic reactor system can be captured by propagating parametric uncertainty through alternative catalytic parameters such as the activation energies. In catalytic flow reactor systems, the effects of catalyst poisoning and fouling can vary in space, and thus, the uncertainty due to catalyst deactivation cannot be adequately captured using a single uncertainty description. Uncertainty analyses were therefore performed in Chapter 6 to analyze the effects of spatially-varying uncertainty due to catalyst deactivation on the single-pore catalytic reactor performance. Furthermore, robust optimization was performed on the multiscale catalytic reactor system subject to spatially-constant and spatially-varying uncertainty descriptions. Due to the large number of uncertainty realizations required to capture the effects of spatially-varying uncertainty, low-order statistical DDMs were developed to efficiently approximate key statistical values in the reactor output variability under uncertainty as a function of the key design and operational parameters. These DDMs were implemented into robust optimization schemes in order to perform efficient optimization on the multiscale catalytic reactor model subject to spatially-constant and spatially-varying uncertainty. As a result, the computational costs for these DDM-based optimization studies were orders of magnitude lower than the computational costs of performing robust optimization using PCE. The results from these studies emphasized that spatially-varying parametric uncertainty can have significant impact on the reactor productivity and can result in significant deviations in optimization studies if it is not taken into consideration.

Catalytic reactor systems are typically operated under continuous conditions, which encourages the use of steady-state reactor models for model-based optimization and design schemes. These approaches,

however, neglect the dynamic reactor behaviour and cannot be used to accommodate for transient changes in the system parameters. Motivated by this, a transient single-pore catalytic reactor model was implemented in Chapter 7 to perform dynamic optimization and simultaneous design and operation control studies on the catalytic reactor subject to parametric uncertainty. PSE was initially used to perform uncertainty analysis on the transient multiscale reactor model in order to evaluate the effects of parametric uncertainty on the reactor behaviour as a function of time and space. In addition, uncertainty analysis was performed on a catalytic reactor system subject to transient changes in the system temperatures. These findings illustrated that changes in the system temperature produce spikes in the species concentrations as the state of the catalyst surface adapts to the changes in the kinetic rates. These observations were subsequently used to design a series of dynamic optimization formulations aiming to identify optimal operating policies. Further dynamic optimization studies were performed to simultaneously identify the optimal reactor design parameters and operating policies that can maximize reactor productivity under uncertainty in the multiscale model parameters. These studies illustrate that optimal time-dependent operating strategies can provide improvements in the reactor performance over static temperature profiles in the multiscale catalytic system.

8.2 Recommendations

The research presented in this work analyzed the impact of parametric uncertainty on the performance of a multiscale catalytic flow reactor system and subsequently implemented uncertainty propagation techniques to perform efficient robust and dynamic optimization studies on the reactor system. There still remain, however, a number of different avenues of potential research in this field. Thus, the following recommendations are made to further extend this research in the future.

Accommodate for time-varying uncertainty in the catalytic reactor performance: Poisoning and fouling are dynamic mechanisms that continually deactivate the catalyst surface over time. As a result, the catalyst parameters affected by catalytic deactivation would be continuously altered in time as the accumulation of poisons and foulants on the catalyst surface increases. It is therefore necessary to expand the uncertainty propagation methods implemented within this work to study the effects of time-varying uncertainty descriptions on the multiscale catalytic reactor performance and to implement transient uncertainty due to catalyst deactivation into dynamic optimization and control processes.

Implement the poisoning/fouling reaction mechanisms into the catalytic reactor model: The research presented in Chapter 6 assumed that the state of catalyst deactivation was unknown, and consequently, uncertainty was propagated through the catalytic parameters to account for the effects of uncertainty. However, the reaction mechanisms for catalyst poisoning and fouling can be directly incorporated into the

lattice-based kMC model, assuming that the kinetic parameters for these events are known. This would allow for the development of dynamic operating policies that can minimize catalyst deactivation in the presence of uncertainty on a multiscale catalytic reactor system.

Extend the kMC model to accommodate for surface diffusion: The present research assumed that the diffusion of adsorbates on the catalyst surface was sufficiently slow for the reaction mechanism considered; and as a result, surface diffusion could be ignored. Complicated heterogeneously-catalyzed reactions, however, often require moderate surface diffusion in order to allow the adsorbed reactants to move within close enough proximity to react. There are several kinetic models for surface diffusion that have been readily implemented into lattice-based kMC models for applications in other fields such as thin film deposition.[53,83] Consequently, surface diffusion should be incorporated into the multiscale catalytic reactor model so that it can accommodate for a wider range of reaction mechanisms.

Extend the techniques to practical catalytic reaction mechanisms: The studies performed in this research were applied to a general bimolecular reaction mechanism between two unspecified reactants A and B to form a gas-phase product C. However, the catalytic reaction mechanisms encountered in typical industrial applications are more complex and involve a substantially larger number of elementary reaction steps. To illustrate the potential for the uncertainty propagation techniques and optimization methodologies assembled in this research, the multiscale catalytic reactor model can be expanded to accommodate a practical industrial example using real experimental data.

Implement coarse-graining techniques to reduce computational cost: The continuum-kMC based multiscale model used in this research can be computationally-intensive to implement, due to the number of individual kinetic events executed during each cycle of the kMC model. There exist numerous spatial and temporal coarse-graining techniques that can be used to reduce the computational cost of the kMC method. In addition, the kinetic events can also be kinetically coarse-grained. In this process, forward and reverse events (i.e. adsorption and desorption of a single species) are combined, based on the difference between their kinetic rates (i.e. $W_{a,s} - W_{d,s}$), such that only the most probable of the two events is considered at each kMC cycle. The considered event would have a modified rate of occurrence based on the difference between the individual event rates, and as a result, fewer events would be required to reach the multiscale trade-off time, Δt_{MST}, reducing the overall computational cost.

Expand the MF approach to accommodate for lateral surface interactions: The MF approach is a substantially faster kinetic surface model as compared to lattice-based kMC; however, it cannot account for lateral interactions between adsorbates on the catalyst surface. Nevertheless, if the MF approach were adapted to accommodate for spatially-dependent interactions, it could provide substantial improvements to the computational cost of the multiscale catalytic reactor model. In addition, the MF approach is closed-

form, and therefore intrusive uncertainty propagation techniques such as Galerkin projection PCE can be applied to efficiently propagate parametric uncertainty at lower computational costs. The MF approach can be modified by developing low-order stochastic models to approximate the rate of events that require lateral interactions (i.e. bimolecular reactions). These low-order models can be developed based on the surface coverages of the interacting species using lattice-based kMC, and they can be implemented into the MF equations to form SDEs that can approximate the lateral catalyst surface interactions and improve the results of the MF approach.

Letter of Copyright Permission

JOHN WILEY AND SONS LICENSE TERMS AND CONDITIONS

Jul 09, 2017

This Agreement between Donovan R.G. Chaffart ("You") and John Wiley and Sons ("John Wiley and Sons") consists of your license details and the terms and conditions provided by John Wiley and Sons and Copyright Clearance Center.

License Number	4144840657691
License date	Jul 09, 2017
Licensed Content Publisher	John Wiley and Sons
Licensed Content Publication	AIChE Journal
Licensed Content Title	Distributional uncertainty analysis and robust optimization in spatially heterogeneous multiscale process systems
Licensed Content Author	Donovan Chaffart,Shabnam Rasoulian,Luis A. Ricardez-Sandoval
Licensed Content Date	Mar 15, 2016
Licensed Content Pages	17
Type of use	Dissertation/Thesis
Requestor type	Author of this Wiley article
Format	Print and electronic
Portion	Full article
Will you be translating?	No
Title of your thesis / dissertation	Uncertainty Analysis and Robust Optimization of Catalytic Flow Reactor Systems
Expected completion date	Jul 2017
Expected size (number of pages)	150
Requestor Location	Donovan R.G. Chaffart 300 Doans Ridge Road Welland, ON L3B 5N7 Canada Attn: Donovan R.G. Chaffart
Publisher Tax ID	EU826007151
Billing Type	Invoice
Billing Address	Donovan R.G. Chaffart 300 Doans Ridge Road Welland, ON L3B 5N7 Canada Attn: Donovan R.G. Chaffart
Total	0.00 CAD
Terms and Conditions	

TERMS AND CONDITIONS

References

1. Bartholomew CH, Farrauto RJ. *Fundamentals of Industrial Catalytic Processes*. 2nd ed. Hoboken, New Jersey: John Wiley & Sons; 2006.

2. Thomas JM, Thomas WJ. *Principles and Practice of Heterogeneous Catalysis*. 2nd ed. Weinheim, Germany: Wiley-VCH; 2015.

3. World Catalysts - Industry Market Research, Market Share, Market Size, Sales, Demand Forecast, Market Leaders, Company Profiles, Industry Trends and Companies including BASF, WR Grace, and Johnson Matthey. Freedonia Group. December 2014.

4. Nauman EB. *Chemical Reactor Design, Optimization, and Scaleup*. 2nd ed. Hoboken, New Jersey: John Wiley & Sons, Inc.; 2008.

5. Senkan SM, Ozturk S. Discovery and optimization of heterogeneous catalysts by using combinatorial chemistry. *Angew Chem Int Ed*. 1999;38(6):791-795.

6. Elnashaie SSEH, Elshishini SS. *Modelling, Simulation and Optimization of Industrial Fixed Bed Catalytic Reactors*. Amsterdam, Netherlands: Gordon and Breach Science Publishers; 1993.

7. Ulissi ZW, Strano MS, Braatz RD. Control of nano and microchemical systems. *Comput Chem Eng*. 2013;51:149-156.

8. Vlachos DG. Multiscale integration hybrid algorithms for homogeneous–heterogeneous reactors. *AIChE J*. 1997;43(11):3031–3041.

9. Raimondeau S, Vlachos DG. Recent developments on multiscale, hierarchical modeling of chemical reactors. *Chem Eng J*. 2002;90(1–2):3-23.

10. Ricardez-Sandoval LA. Current challenges in the design and control of multiscale systems. *Can J Chem Eng*. 2011;89(6):1324-1341.

11. Vlachos DG. Multiscale modeling for emergent behavior, complexity, and combinatorial explosion. *AIChE J*. 2012;58(5):1314-1325.

12. Salciccioli M, Stamatakis M, Caratzoulas S, Vlachos DG. A review of multiscale modeling of metal-catalyzed reactions: Mechanism development for complexity and emergent behavior. *Chem Eng Sci*. 2011;66(19):4319-4355.

13. Lou Y, Christofides PD. Feedback control of growth rate and surface roughness in thin film growth. *AIChE J*. 2003;49(8):2099-2113.

14. Majumder D, Broadbelt LJ. A multiscale scheme for modeling catalytic flow reactors. *AIChE J*. 2006;52(12):4214-4228.

15. Braatz RD, Alkire RC, Seebauer E, et al. Perspectives on the design and control of multiscale systems. *J Process Control*. 2006;16(3):193-204.

16. Prasad V, Karim AM, Arya A, Vlachos DG. Assessment of Overall Rate Expressions and Multiscale, Microkinetic Model Uniqueness via Experimental Data Injection: Ammonia Decomposition on Ru/γ-Al2O3 for Hydrogen Production. *Ind Eng Chem Res*. 2009;48(11):5255-5265.

17. Ulissi Z, Prasad V, Vlachos DG. Effect of multiscale model uncertainty on identification of optimal catalyst properties. *J Catal*. 2011;281(2):339-344.

18. Butt JB, Petersen EE. *Activation, Deactivation, and Poisoning of Catalysts*. San Diego, California: Academic Press, Inc.; 1988.

19. Oudar J, Wise H. *Deactivation and Poisoning of Catalysts*. New York, New York: Marcel Dekker, Inc; 1985.

20. Froment GF, Bischoff KB. Kinetic data and product distributions from fixed bed catalytic reactors subject to catalyst fouling. *Chem Eng Sci*. 1962;17(2):105-114.

21. Patwardhan RS, Shah SL. Issues in performance diagnostics of model-based controllers. *J Process Control*. 2002;12(3):413-427.

22. Patwardhan RS, Shah SL, Qi KZ. Assessing the Performance of Model Predictive Controllers. *Can J Chem Eng*. 2002;80(5):954-966.

23. Selvanathan S, Tangirala AK. Diagnosis of Poor Control Loop Performance Due to Model−Plant Mismatch. *Ind Eng Chem Res*. 2010;49(9):4210-4229.

24. Prasad V, Vlachos DG. Multiscale Model and Informatics-Based Optimal Design of Experiments: Application to the Catalytic Decomposition of Ammonia on Ruthenium. *Ind Eng Chem Res*. 2008;47(17):6555-6567.

25. Chaffart D, Rasoulian S, Ricardez-Sandoval LA. Distributional uncertainty analysis and robust optimization in spatially heterogeneous multiscale process systems. *AIChE J*. 2016;62(7):2374-2390.

26. Chaffart D, Ricardez-Sandoval LA. Robust Optimization of a Multiscale Catalytic Reactor System with Spatially-Varying Uncertainty Descriptions using Polynomial Chaos Expansions. Can J Chem Eng. In Press.

27. Chaffart DR, Ricardez-Sandoval LA. Distributional Uncertainty Analysis in Transient Heterogeneous Multiscale Catalytic Flow Reactors. 11th IFAC Symposium on Dynamics and Control of Process Systems, Trondheim, Sweden, 6-8 June 2016:436-441.

28. Chaffart D, Ricardez-Sandoval LA. Robust dynamic optimization in heterogeneous multiscale catalytic flow reactors using polynomial chaos expansion. *J Process Control*. 2017. http://dx.doi.org/10.1016/j.jprocont.2017.07.002

29. Bournay L, Casanave D, Delfort B, Hillion G, Chodorge JA. New heterogeneous process for biodiesel production: A way to improve the quality and the value of the crude glycerin produced by biodiesel plants. *Catal Today*. 2005;106(1–4):190-192.

30. Chen B, Parker G, Han J, Meyyappan M, Cassell AM. Heterogeneous single-walled carbon nanotube catalyst discovery and optimization. *Chem Mater*. 2002;14(4):1891-1896.

31. Vlachos DG, Mhadeshwar AB, Kaisare NS. Hierarchical multiscale model-based design of experiments, catalysts, and reactors for fuel processing. *Comput Chem Eng*. 2006;30(10–12):1712-1724.

32. Bhaduri S, Mukesh D. *Homogeneous Catalysis: Mechanisms and Industrial Applications*. 2nd ed. Hoboken, New Jersey: Wiley; 2014.

33. Bertini I. *Inorganic and Bio-Inorganic Chemistry - Volume II*. Oxford, United Kingdom: EOLSS Publications; 2009.

34. Le Page AJF. *Catalyse de Contact. Conception, Préparation et Mise en Œuvre des Catalyseurs Industriels*. Paris, France: Éditions Technip; 1978.

35. Jae J, Tompsett GA, Foster AJ, et al. Investigation into the shape selectivity of zeolite catalysts for biomass conversion. *J Catal*. 2011;279(2):257-268.

36. Bartholomew CH. Mechanisms of catalyst deactivation. *Appl Catal Gen*. 2001;212(1-2):17-60.

37. Alenazey F, Cooper CG, Dave CB, Elnashaie SSEH, Susu AA, Adesina AA. Coke removal from deactivated Co–Ni steam reforming catalyst using different gasifying agents: An analysis of the gas–solid reaction kinetics. *Catal Commun*. 2009;10(4):406-411.

38. Trimm DL. The regeneration or disposal of deactivated heterogeneous catalysts. *Appl Catal Gen*. 2001;212(1):153-160.

39. Moulijn J., van Diepen A., Kapteijn F. Catalyst deactivation: is it predictable? *Appl Catal Gen*. 2001;212(1-2):3-16.

40. Argyle MD, Bartholomew CH. Heterogeneous Catalyst Deactivation and Regeneration: A Review. *Catalysts*. 2015;5(1):145-269.

41. Rocha TCR, Hävecker M, Knop-Gericke A, Schlögl R. Promoters in heterogeneous catalysis: The role of Cl on ethylene epoxidation over Ag. *J Catal*. 2014;312:12-16.

42. Sheldon RA, Bekkum H van. *Fine Chemicals through Heterogeneous Catalysis*. Weinheim, Germany: Wiley-VCH; 2001.

43. Kirschning A, Solodenko W, Mennecke K. Combining Enabling Techniques in Organic Synthesis: Continuous Flow Processes with Heterogenized Catalysts. *Chem – Eur J*. 2006;12(23):5972-5990.

44. Leung S-A, Winkle RF, Wootton RCR, deMello AJ. A method for rapid reaction optimisation in continuous-flow microfluidic reactors using online Raman spectroscopic detection. *Analyst*. 2005;130(1):46-51.

45. He BB, Singh AP, Thompson JC. Experimental optimization of a continuous-flow reactive distillation reactor for biodiesel production. *Trans ASAE*. 2005;48(6):2237–2243.

46. Ganley JC, Riechmann KL, Seebauer EG, Masel RI. Porous anodic alumina optimized as a catalyst support for microreactors. *J Catal*. 2004;227(1):26-32.

47. Jirát J, Kubíček M, Marek M. Mathematical modelling of catalytic monolithic reactors with storage of reaction components on the catalyst surface. *Catal Today*. 1999;53(4):583-596.

48. Champagnie AM, Tsotsis TT, Minet RG, Wagner E. The study of ethane dehydrogenation in a catalytic membrane reactor. *J Catal*. 1992;134(2):713-730.

49. Hayes RE, Kolaczkowski ST, Thomas WJ. Finite-element model for a catalytic monolith reactor. *Comput Chem Eng*. 1992;16(7):645-657.

50. Rawlston JA, Schork FJ, Grover MA. Multiscale Modeling of Branch Length in Butyl Acrylate Solution Polymerization. *Macromol Theory Simul*. 2010;19(6):309-322.

51. Rawlston JA, Schork FJ, Grover MA. Multiscale Modeling of Branch Length in Butyl Acrylate Solution Polymerization: Molecular Versus Continuum Kinetics. *Macromol Theory Simul*. 2011;20(8):645-659.

52. Christofides PD, Armaou A. Control and optimization of multiscale process systems. *Comput Chem Eng*. 2006;30(10-12):1670-1686.

53. Christofides PD, Armaou A, Lou Y, Varshney A. *Control and Optimization of Multiscale Process Systems*. Boston, Massachusetts: Birkhäuser; 2009.

54. Kwon JS-I, Nayhouse M, Orkoulas G, Ni D, Christofides PD. Run-to-Run-Based Model Predictive Control of Protein Crystal Shape in Batch Crystallization. *Ind Eng Chem Res*. 2015;54(16):4293-4302.

55. Kwon JS-I, Nayhouse M, Christofides PD. Detection and Isolation of Batch-to-Batch Parametric Drift in Crystallization Using In-Batch and Post-Batch Measurements. *Ind Eng Chem Res*. 2015;54(20):5514-5526.

56. Matera S, Reuter K. Transport limitations and bistability for *in situ* CO oxidation at RuO 2 (110) : First-principles based multiscale modeling. *Phys Rev B*. 2010;82(8):085446.

57. Schaefer C, Jansen APJ. Coupling of kinetic Monte Carlo simulations of surface reactions to transport in a fluid for heterogeneous catalytic reactor modeling. *J Chem Phys*. 2013;138(5):054102.

58. Nieminen RM. From atomistic simulation towards multiscale modelling of materials. *J Phys Condens Matter*. 2002;14(11):2859.

59. Batchelor GK. *An Introduction to Fluid Dynamics*. Cambridge, United Kingdom: Cambridge University Press; 2000.

60. Smith GD. *Numerical Solution of Partial Differential Equations: Finite Difference Methods*. Oxford, United Kingdom: Oxford University Press; 1985.

61. Szabo BA, Babuška I. *Finite Element Analysis*. John Wiley & Sons; 1991.

62. Keil FJ. Multiscale Modelling in Computational Heterogeneous Catalysis. In: Kirchner B, Vrabec J, eds. *Multiscale Molecular Methods in Applied Chemistry*. Topics in Current Chemistry. Springer-Verlag; 2012:69-107.

63. Hansen N, Krishna R, van Baten JM, Bell AT, Keil FJ. Analysis of Diffusion Limitation in the Alkylation of Benzene over H-ZSM-5 by Combining Quantum Chemical Calculations, Molecular Simulations, and a Continuum Approach. *J Phys Chem C*. 2009;113(1):235-246.

64. Vlachos DG, Schmidt LD, Aris R. The effect of phase transitions, surface diffusion, and defects on heterogeneous reactions: multiplicities and fluctuations. *Surf Sci*. 1991;249(1):248-264.

65. Raimondeau S, Vlachos DG. The role of adsorbate-layer nonuniformities in catalytic reactor design: multiscale simulations for CO oxidation on Pt. *Comput Chem Eng*. 2002;26(7–8):965-980.

66. Dooling DJ, Broadbelt LJ. Generic Monte Carlo Tool for Kinetic Modeling. *Ind Eng Chem Res*. 2001;40(2):522-529.

67. Gillespie DT. Approximate accelerated stochastic simulation of chemically reacting systems. *J Chem Phys*. 2001;115(4):1716–1733.

68. Voter AF. INTRODUCTION TO THE KINETIC MONTE CARLO METHOD. In: *Radiation Effects in Solids*. NATO Science Series. Dordrecht, Netherlands: Springer; 2007:1-23.

69. Makeev AG, Maroudas D, Panagiotopoulos AZ, Kevrekidis IG. Coarse bifurcation analysis of kinetic Monte Carlo simulations: A lattice-gas model with lateral interactions. *J Chem Phys*. 2002;117(18):8229.

70. Ovesson S, Lundqvist BI, Schneider WF, Bogicevic A. NO oxidation properties of Pt(111) revealed by *ab initio* kinetic simulations. *Phys Rev B*. 2005;71(11).

71. Schulze TP. Efficient kinetic Monte Carlo simulation. *J Comput Phys*. 2008;227(4):2455-2462.

72. Armaou A, I Siettos C, G Kevrekidis I. Time-steppers and “coarse”control of distributed microscopic processes. *Int J Robust Nonlinear Control*. 2004;14(2):89–111.

73. Katsoulakis MA, Majda AJ, Vlachos DG. Coarse-grained stochastic processes and Monte Carlo simulations in lattice systems. *J Comput Phys*. 2003;186(1):250-278.

74. Mandreoli L, Neugebauer J, Kunert R, Schöll E. Adatom density kinetic Monte Carlo: A hybrid approach to perform epitaxial growth simulations. *Phys Rev B*. 2003;68(15).

74. Tsalikis D, Baig C, Mavrantzas VG, Amanatides E, Mataras D. Hierarchical simulation of microcrystalline PECVD silicon thin film growth and structure. 13th International Conference on Plasma Surface Engineering, Garmisch-Partenkirchen, Germany, 10-14 September 2012:22-25

76. Katsoulakis MA, Vlachos DG. Coarse-grained stochastic processes and kinetic Monte Carlo simulators for the diffusion of interacting particles. *J Chem Phys*. 2003;119(18):9412-9427.

77. Drews TO, Braatz RD, Alkire RC. Coarse-Grained Kinetic Monte Carlo Simulation of Copper Electrodeposition with Additives. *Int J Multiscale Comput Eng*. 2004;2(2).

78. Chatterjee A, Vlachos DG. Temporal acceleration of spatially distributed kinetic Monte Carlo simulations. *J Comput Phys*. 2006;211(2):596-615.

79. Vlachos DG. Temporal coarse-graining of microscopic-lattice kinetic Monte Carlo simulations via $\ensuremath{\tau}$ leaping. *Phys Rev E*. 2008;78(4):046713.

80. Siettos CI, Armaou A, Makeev AG, Kevrekidis IG. Microscopic/stochastic timesteppers and “coarse” control: A KMC example. *AIChE J*. 2003;49(7):1922-1926.

81. Kevrekidis IG, Gear CW, Hummer G. Equation-free: The computer-aided analysis of complex multiscale systems. *AIChE J*. 2004;50(7):1346-1355.

82. Makov G, Payne MC. Periodic boundary conditions in ab initio calculations. *Phys Rev B*. 1995;51(7):4014-4022.

83. Rasoulian S, Ricardez-Sandoval LA. Uncertainty analysis and robust optimization of multiscale process systems with application to epitaxial thin film growth. *Chem Eng Sci*. 2014;116:590-600.

84. Kwon JS-I, Nayhouse MJ, Christofides PD. Multiscale, multidomain modeling and parallel computation: application to crystal shape evolution in crystallization. *Ind Eng Chem Res*. November 2015.

85. Lou Y, Christofides PD. Estimation and control of surface roughness in thin film growth using kinetic Monte-Carlo models. *Chem Eng Sci*. 2003;58(14):3115-3129.

86. Rusli E, Drews TO, Braatz RD. Systems analysis and design of dynamically coupled multiscale reactor simulation codes. *Chem Eng Sci*. 2004;59(22):5607-5613.

87. Drews TO, Webb EG, Ma DL, Alameda J, Braatz RD, Alkire RC. Coupled mesoscale—continuum simulations of copper electrodeposition in a trench. *AIChE J*. 2004;50(1):226–240.

88. Rusli E, Drews TO, Ma DL, Alkire RC, Braatz RD. Robust nonlinear feedback–feedforward control of a coupled kinetic Monte Carlo–finite difference simulation. *J Process Control*. 2006;16(4):409-417.

89. Vlachos DG. A Review of Multiscale Analysis: Examples from Systems Biology, Materials Engineering, and Other Fluid–Surface Interacting Systems. In: Marin GB, ed. *Advances in Chemical Engineering*. Vol 30. Advances in Chemical Engineering: Multiscale Analysis. San Diego, California: Elsevier; 2005:1-61.

90. Crose M, Sang-Il Kwon J, Nayhouse M, Ni D, Christofides PD. Multiscale modeling and operation of PECVD of thin film solar cells. *Chem Eng Sci*.

91. Gear CW, Li J, Kevrekidis IG. The gap-tooth method in particle simulations. *Phys Lett A*. 2003;316(3-4):190-195.

92. Kevrekidis IG, Gear CW, Hyman JM, et al. Equation-free, coarse-grained multiscale computation: Enabling mocroscopic simulators to perform system-level analysis. *Commun Math Sci*. 2003;1(4):715–762.

93. Armaou A, Kevrekidis IG, Theodoropoulos C. Equation-free gaptooth-based controller design for distributed complex/multiscale processes. *Comput Chem Eng*. 2005;29(4):731-740.

94. Samaey G, Roose D, Kevrekidis IG. The gap-tooth scheme for homogenization problems. *Multiscale Model Simul*. 2005;4(1):278–306.

95. Roberts AJ, Kevrekidis IG. Higher order accuracy in the gap-tooth scheme for large-scale dynamics using microscopic simulators. *ANZIAM J*. 2005;46(0):637-657.

96. Allen JK, Seepersad C, Choi H, Mistree F. Robust design for multiscale and multidisciplinary applications. *J Mech Des*. 2006;128(4):832–843.

97. Maria G, Dan A. Setting Safety Limits and Operating Policies under Parametric Uncertainty for a Semi-batch Catalytic Reactor of High Thermal Sensitivity. *Rev Chim*. 2011;62(4):469-478.

98. Evans RD, Ricardez-Sandoval LA. Multi-scenario modelling of uncertainty in stochastic chemical systems. *J Comput Phys*. 2014;273:374-392.

99. Yao KZ, Shaw BM, Kou B, McAuley KB, Bacon DW. Modeling Ethylene/Butene Copolymerization with Multi-site Catalysts: Parameter Estimability and Experimental Design. *Polym React Eng*. 2003;11(3):563-588.

100. Li J, Croiset E, Ricardez–Sandoval L. Effect of carbon on the Ni catalyzed methane cracking reaction: A DFT study. *Appl Surf Sci*. 2014;311:435-442.

101. Li J, Croiset E, Ricardez-Sandoval L. Carbon nanotube growth: First-principles-based kinetic Monte Carlo model. *J Catal*. 2015;326:15-25.

102. Schuch N, Verstraete F. Computational complexity of interacting electrons and fundamental limitations of density functional theory. *Nat Phys*. 2009;5(10):732-735.

103. Forzatti P, Lietti L. Catalyst deactivation. *Catal Today*. 1999;52(2–3):165-181.

104. Wolf EE, Alfani F. Catalysts Deactivation by Coking. *Catal Rev*. 1982;24(3):329-371.

105. Xu M, Shi C, Yang X. Effect of Carbon Dioxide on the Activation Energy for Methyl Radical Generation Over Li/Mgo Catalysts. *J Phys Chem*. 1992;96(15).

106. Yu T-C, Shaw H. The effect of sulfur poisoning on methane oxidation over palladium supported on γ-alumina catalysts. *Appl Catal B Environ*. 1998;18(1–2):105-114.

107. Lisi L, Lasorella G, Malloggi S, Russo G. Single and combined deactivating effect of alkali metals and HCl on commercial SCR catalysts. *Appl Catal B Environ*. 2004;50(4):251-258.

108. Froment GF, Bischoff KB. Non-steady state behaviour of fixed bed catalytic reactors due to catalyst fouling. *Chem Eng Sci*. 1961;16(3):189-201.

109. Cheah KY, Chiaranussati N, Hollewand MP, Gladden LF. Coke profiles in deactivated alumina pellets studied by NMR imaging. *Appl Catal Gen*. 1994;115(1):147-155.

110. Kwon JS-I, Nayhouse M, Orkoulas G, Ni D, Christofides PD. A method for handling batch-to-batch parametric drift using moving horizon estimation: Application to run-to-run MPC of batch crystallization. *Chem Eng Sci*. 2015;127:210-219.

111. Reuter K, Scheffler M. First-principles kinetic Monte Carlo simulations for heterogeneous catalysis: Application to the CO oxidation at Ru O 2 (110). *Phys Rev B*. 2006;73(4).

112. Hong S, Karim A, Rahman TS, Jacobi K, Ertl G. Selective oxidation of ammonia on RuO2(110): A combined DFT and KMC study. *J Catal*. 2010;276(2):371-381.

113. Fichthorn KA, Weinberg WH. Theoretical foundations of dynamical Monte Carlo simulations. *J Chem Phys*. 1991;95(2):1090-1096.

114. Rooney WC, Biegler LT. Incorporating joint confidence regions into design under uncertainty. *Comput Chem Eng*. 1999;23(10):1563-1575.

115. Halemane KP, Grossmann IE. Optimal process design under uncertainty. *AIChE J*. 1983;29(3):425-433.

116. Karimi H, McAuley KB. An approximate expectation maximisation algorithm for estimating parameters in nonlinear dynamic models with process disturbances. *Can J Chem Eng*. 2014;92(5):835-850.

117. Karimi H, McAuley KB. An Approximate Expectation Maximization Algorithm for Estimating Parameters, Noise Variances, and Stochastic Disturbance Intensities in Nonlinear Dynamic Models. *Ind Eng Chem Res*. 2013;52(51):18303-18323.

118. Karimi H, McAuley KB. A maximum-likelihood method for estimating parameters, stochastic disturbance intensities and measurement noise variances in nonlinear dynamic models with process disturbances. *Comput Chem Eng*. 2014;67:178-198.

118. Nagy ZK, Braatz RD. Distributional uncertainty analysis of a batch crystallization process using power series and polynomial chaos expansions. Proceedings of the 8th IFAC Symposium on Advanced Control of Chemical Processes, Grandamo, Brazil, 2-5 April 2006:655–660.

120. Nagy ZK, Braatz RD. Distributional uncertainty analysis using power series and polynomial chaos expansions. *J Process Control*. 2007;17(3):229-240.

121. Herzog M, Gilg A, Paffrath M, Rentrop P, Wever U. Intrusive versus non-intrusive methods for stochastic finite elements. In: *From Nano to Space*. Springer-Verlag; 2008:161–174.

121. Eldred MS. Recent advances in non-intrusive polynomial chaos and stochastic collocation methods for uncertainty analysis and design. 50th AIAA/ASME/ASCE/AHS/ASC Structures, Structural Dynamics, and Materials Conference, Palm Springs, California, 4-7 May 2009.

123. Xiu D. *Numerical Methods for Stochastic Computations: A Spectral Method Approach*. Princeton, N.J: Princeton University Press; 2010.

124. Mehta S, Ricardez-Sandoval LA. Integration of Design and Control of Dynamic Systems under Uncertainty: A New Back-Off Approach. *Ind Eng Chem Res*. 2016;55(2):485-498.

124. Xiong F, Xue B, Yan Z, Yang S. Polynomial chaos expansion based robust design optimization. 2011 International Conference on Quality, Reliability, Risk, Maintenance, and Safety Engineering, Xi'an, China, 17-19 June 2011:868-873.

126. Dodson M, Parks GT. Robust Aerodynamic Design Optimization Using Polynomial Chaos. *J Aircr*. 2009;46(2):635-646.

127. Rasoulian S, Ricardez-Sandoval LA. A robust nonlinear model predictive controller for a multiscale thin film deposition process. *Chem Eng Sci*. 2015;136:38-49.

127. Rasoulian S, Ricardez-Sandoval LA. Worst-case and Distributional Robustness Analysis of a Thin Film Deposition Process. 9th International Symposium on Advanced Control of Chemical Processes, Whistler, Canada, 7-10 June 2015: 1126-1131

129. Rasoulian S, Ricardez-Sandoval LA. Robust multivariable estimation and control in an epitaxial thin film growth process under uncertainty. *J Process Control*. 2015;34:70-81.

130. Rasoulian S, Ricardez-Sandoval LA. Stochastic nonlinear model predictive control applied to a thin film deposition process under uncertainty. *Chem Eng Sci*. 2016;140:90-103.

131. Rafiei-Shishavan M, Mehta S, Ricardez-Sandoval LA. Simultaneous design and control under uncertainty: A back-off approach using power series expansions. *Comput Chem Eng*. 2017;99:66-81.

132. Bahakim SS, Rasoulian S, Ricardez-Sandoval LA. Optimal design of large-scale chemical processes under uncertainty: A ranking-based approach. *AIChE J*. 2014;60(9):3243-3257.

133. Bahakim SS, Ricardez-Sandoval LA. Optimal Design of a Postcombustion CO2 Capture Pilot-Scale Plant under Process Uncertainty: A Ranking-Based Approach. *Ind Eng Chem Res*. 2015;54(15):3879-3892.

133. Kimaev G, Ricardez-Sandoval LA. A comparison of efficient uncertainty quantification techniques for stochastic multiscale systems. AIChE J. March 2017. In Press.

135. Drews TO, Braatz RD, Alkire RC. Parameter Sensitivity Analysis of Monte Carlo Simulations of Copper Electrodeposition with Multiple Additives. *J Electrochem Soc*. 2003;150(11):C807-C812.

136. McGill JA, Ogunnaike BA, Vlachos DG. Efficient gradient estimation using finite differencing and likelihood ratios for kinetic Monte Carlo simulations. *J Comput Phys*. 2012;231(21):7170-7186.

137. Nagy ZK, Braatz RD. Robust nonlinear model predictive control of batch processes. *AIChE J*. 2003;49(7):1776-1786.

138. Ma DL, Braatz RD. Worst-case analysis of finite-time control policies. *Control Syst Technol IEEE Trans On*. 2001;9(5):766–774.

139. Varshney A, Armaou A. Reduced order modeling and dynamic optimization of multiscale PDE/kMC process systems. *Comput Chem Eng*. 2008;32(9):2136-2143.

140. Lam R, Vlachos DG. Multiscale model for epitaxial growth of films: Growth mode transition. *Phys Rev B*. 2001;64(3).

141. Crestaux T, Le Maıˆtre O, Martinez J-M. Polynomial chaos expansion for sensitivity analysis. *Reliab Eng Syst Saf*. 2009;94(7):1161-1172.

141. Paulson JA, Mesbah A, Streif S, Findeisen R, Braatz RD. Fast stochastic model predictive control of high-dimensional systems. 53rd IEEE Conference on Decision and Control, Los Angeles, California, 15-17 December 2014:2802–2809.

143. Kuang D, Charrière R, Matsapey N, Flury M, Faucheu J, Chavel P. Modeling the specular spectral reflectance of partially ordered alumina nanopores on an aluminum substrate. *Opt Express*. 2015;23(4):4506.

144. Veser G, Frauhammer J. Modelling steady state and ignition during catalytic methane oxidation in a monolith reactor. *Chem Eng Sci*. 2000;55(12):2271-2286.

Appendix A
Supplementary Material for Chapter 6

The statistical data-driven models (DDMs) implemented in the main body of this work were determined using TableCurve 3D® to fit PCE-generated statistical data to a large set of candidate models, including high-order polynomials, and rank them according to their accuracy as determined through their R-squared values. The model for each key statistical parameter was selected based on its ability to accurately capture the generated data for all of the uncertainty descriptions implemented, which was assessed by their R-squared values. The DDMs were determined to be as follows:

$$\frac{\ln\left(\mu\left(C_{AB,out},T,\nu,\rho\right)\right)}{T\nu\rho} = b_{\mu,0} + b_{\mu,1}T + b_{\mu,2}T^2 + b_{\mu,3}\sqrt{\nu} + \frac{b_{\mu,4}}{\ln\left(\frac{\nu}{1000}\right)} + b_{\mu,5}\sqrt{\rho} + \frac{b_{\mu,6}}{\ln\left(\frac{\rho}{1\times10^9}\right)} \tag{A-1}$$

$$\frac{\ln\left(\sigma^2\left(C_{AB,out},T,\nu,\rho\right)\right)}{T\nu\rho} =$$

$$b_{\sigma^2,0} + b_{\sigma^2,1}T + b_{\sigma^2,2}\mathrm{e}^{-\frac{\nu}{10}} + b_{\sigma^2,3}\mathrm{e}^{-\frac{\rho}{10}} + b_{\sigma^2,4}T\mathrm{e}^{-\frac{\nu}{10}} + b_{\sigma^2,5}T\mathrm{e}^{-\frac{\rho}{10}} + b_{\sigma^2,6}\mathrm{e}^{\frac{-\nu-\rho}{10}} + b_{\sigma^2,7}T\mathrm{e}^{\frac{-\nu-\rho}{10}} \tag{A-2}$$

$$\frac{\ln\left(C_{AB,out}^{up}(T,\nu,\rho)\right)}{T\nu\rho} = b_{up,0} + b_{up,1}T + b_{up,2}T^2 + b_{up,3}\sqrt{\nu} + \frac{b_{up,4}}{\ln\left(\frac{\nu}{1000}\right)} + b_{up,5}\sqrt{\rho} + \frac{b_{up,6}}{\ln\left(\frac{\rho}{1\times10^9}\right)} \tag{A-3}$$

$$\frac{\ln\left(C_{AB,out}^{lw}(T,\nu,\rho)\right)}{T\nu\rho} = b_{lw,0} + b_{lw,1}T + b_{lw,2}T^2 + b_{lw,3}\sqrt{\nu} + \frac{b_{lw,4}}{\ln\left(\frac{\nu}{1000}\right)} + b_{lw,5}\sqrt{\rho} + \frac{b_{lw,6}}{\ln\left(\frac{\rho}{1\times10^9}\right)} \tag{A-4}$$

where T, ν, and ρ denote the temperature in K, the fluid velocity in mm/s, and the pore radius in nm respectively. The DMM parameters were determined using least-squares regression to fit PCE-derived statistical data-points computed at various reactor temperatures, fluid velocities, and pore radii for each of the four uncertainty descriptions implemented in this work. These uncertainty descriptions consist of *Scenario 1A* (spatially-constant uncertainty in $E_{d,A}$ as described by Eq. (6-1)), *Scenario 1B* (spatially-varying uncertainty in $E_{d,A}$ as described by Eq. (6-2)), *Scenario 2A* (spatially-constant uncertainty in $E_{d,A}$ and E_r as described by Eq. (6-3)), and *Scenario 2B* (spatially-varying uncertainty in $E_{d,A}$ and E_r as described by Eqs. (6-2) and (6-4)). The parameters for each DDM are provided in Tables A-1 through A-4 below. Additionally, Tables A-5 through A-7 compare the results obtained from the DDMs and from PCE approximations for the five randomly-generated combinations of T, ν, and ρ for *Scenario 1A*, *Scenario 2A*, and *Scenario 2B*, respectively.

Table A-1. DDM parameters to estimate the expected value of the outlet product concentration $\mu(C_{C,out})$.

	Scenario 1A	***Scenario 1B***	***Scenario 2A***	***Scenario 2B***
$b_{\mu,0}$	45.123	47.058	49.597	49.272
$b_{\mu,1}$	0.217 50	0.211 70	0.208 07	0.207 22
$b_{\mu,2}$	-2.2861×10^{-4}	-2.2232×10^{-4}	-2.1869×10^{-4}	-2.1759×10^{-4}
$b_{\mu,3}$	7.8704	7.728	8.1097	7.9575
$b_{\mu,4}$	305.68	300.97	313.67	308.63
$b_{\mu,5}$	0.302 25	0.350 04	0.353 57	0.358 69
$b_{\mu,6}$	841.80	866.38	868.14	871.05

Table A-2. DDM parameters to estimate the variance of the outlet product concentration $\sigma^2(C_{C,out})$.

	Scenario 1A	***Scenario 1B***	***Scenario 2A***	***Scenario 2B***
$b_{\sigma^2,0}$	-16.486	-9.6107	-6.8512	-2.9203
$b_{\sigma^2,1}$	2.3123×10^{-2}	5.3188×10^{-3}	3.8976×10^{-3}	-7.3941×10^{-3}
$b_{\sigma^2,2}$	32.980	15.420	15.128	2.4507
$b_{\sigma^2,3}$	26.679	14.406	16.538	0.895 38
$b_{\sigma^2,4}$	-5.1531×10^{-2}	-1.3128×10^{-2}	-1.4147×10^{-2}	1.2740×10^{-2}
$b_{\sigma^2,5}$	-3.8118×10^{-2}	-1.0908×10^{-2}	-1.6991×10^{-2}	1.6123×10^{-2}
$b_{\sigma^2,6}$	-42.266	-21.490	-17.653	18.317
$b_{\sigma^2,7}$	8.7922×10^{-2}	4.0692×10^{-2}	3.7080×10^{-2}	-3.9571×10^{-2}

Table A-3. DDM parameters to estimate the upper bound of the outlet product concentration $C_{C,out}^{up}$.

	Scenario 1A	***Scenario 1B***	***Scenario 2A***	***Scenario 2B***
$b_{up,0}$	49.025	53.339	80.254	62.837
$b_{up,1}$	0.160 96	0.158 01	0.104 43	0.147 73
$b_{up,2}$	-1.6748×10^{-4}	-1.6555×10^{-4}	-1.1074×10^{-4}	-1.5551×10^{-4}
$b_{up,3}$	7.793	6.4618	8.867	7.8388
$b_{up,4}$	303.03	258.8	338.8	304.67
$b_{up,5}$	-0.073 98	0.292 71	0.448 69	0.342 14
$b_{up,6}$	652.91	837.01	918.04	862.81

Table A-4. DDM parameters to estimate the upper bound of the outlet product concentration $C_{C,out}^{lw}$.

	Scenario 1A	***Scenario 1B***	***Scenario 2A***	***Scenario 2B***
$b_{lw,0}$	-78.257	29.698	-29.163	35.323
$b_{lw,1}$	0.591 28	0.277 25	0.527 02	0.267 09
$b_{lw,2}$	-6.2029×10^{-4}	-2.9091×10^{-4}	-5.5053×10^{-4}	-2.7941×10^{-4}
$b_{lw,3}$	5.6773	7.9957	9.5261	8.3118
$b_{lw,4}$	231.56	309.95	360.42	320.57
$b_{lw,5}$	-0.692 24	0.243 46	0.098 04	0.327 05
$b_{lw,6}$	332.89	813.41	724.89	857.72

Table A-5. Accuracy of the DDMs for $\mu(C_{C,out})$, $\sigma^2(C_{C,out})$, $C_{C,out}^{up}$, and $C_{C,out}^{lw}$ compared to five randomly-generated sample points determined via PCE for *Scenario 1A*.

			$\mu(C_{C,out})$ (mmol\L)	$\sigma^2(C_{C,out})$ (mmol^2/L^2)	$C_{AB,out}^{up}$ (mmol/L)	$C_{AB,out}^{lw}$ (mmol/L)
Point 1: MC sampling	***T* (K)**	485.88	1.8040	0.093 92	2.3092	0.9131
	***v* (mm/s)**	10.500				
PCE			1.8110 (0.39%)	0.087 10 (7.26%)	2.3407 (1.36%)	0.9982 (9.31%)
	***ρ* (nm)**	10.263				
Point 2: MC sampling	***T* (K)**	447.82	1.0179	0.037 11	1.2676	0.4125
	***v* (mm/s)**	13.108				
PCE			1.0212 (0.32%)	0.034 50 (7.03%)	1.2847 (1.35%)	0.4076 (1.19%)
	***ρ* (nm)**	11.532				
Point 3: MC sampling	***T* (K)**	467.89	2.3738	0.151 98	2.8883	1.1541
	***v* (mm/s)**	7.3199				
PCE			2.3664 (0.31%)	0.151 05 (0.61%)	2.9506 (2.16%)	1.2653 (9.63%)
	***ρ* (nm)**	10.859				
Point 4: MC sampling	***T* (K)**	473.52	2.1384	0.110 39	2.7014	1.1833
	***v* (mm/s)**	7.6877				
PCE			2.1252 (0.62%)	0.116 98 (5.97%)	2.6504 (1.89%)	1.1596 (2.00%)
	***ρ* (nm)**	11.802				
Point 5: MC sampling	***T* (K)**	463.65	2.7231	0.190 66	3.3037	1.3593
	***v* (mm/s)**	8.7780				
PCE			2.7306 (0.27%)	0.210 90 (10.6%)	3.4223 (3.59%)	1.4351 (5.58%)
	***ρ* (nm)**	7.6514				

Table A-6. Accuracy of the DDMs for $\mu(C_{C,out})$, $\sigma^2(C_{C,out})$, $C_{C,out}^{up}$, and $C_{C,out}^{lw}$ compared to five randomly-generated sample points determined via PCE for *Scenario 2A*.

			$\mu(C_{C,out})$ (mmol\L)	$\sigma^2(C_{C,out})$ (mmol^2/L^2)	$C_{AB,out}^{up}$ (mmol/L)	$C_{AB,out}^{lw}$ (mmol/L)
Point 1: MC sampling	***T* (K)**	485.88	1.7899	0.147 27	2.4600	0.6816
	***v* (mm/s)**	10.500				
PCE			1.7934 (0.19%)	0.134 62 (8.59%)	2.4631 (0.12%)	0.7792 (14.3%)
	***ρ* (nm)**	10.263				
Point 2: MC sampling	***T* (K)**	447.82	1.0147	0.062 53	1.5273	0.3343
	***v* (mm/s)**	13.108				
PCE			1.0197 (0.50%)	0.067 27 (7.57%)	1.5708 (2.84%)	0.3176 (4.99%)
	***ρ* (nm)**	11.532				
Point 3: MC sampling	***T* (K)**	467.89	2.3636	0.264 70	3.3103	0.9121
	***v* (mm/s)**	7.3199				
PCE			2.3441 (0.82%)	0.252 27 (4.70%)	3.2587 (1.56%)	0.9706 (6.41%)
	***ρ* (nm)**	10.859				
Point 4: MC sampling	***T* (K)**	473.52	2.1309	0.178 69	2.8975	0.9356
	***v* (mm/s)**	7.6877				
PCE			2.1048 (1.22%)	0.192 01 (7.45%)	2.8940 (0.12%)	0.9036 (3.42%)
	***ρ* (nm)**	11.802				
Point 5: MC sampling	***T* (K)**	463.65	2.7297	0.341 94	3.9217	1.1804
	***v* (mm/s)**	8.7780				
PCE			2.7043 (0.93%)	0.363 72 (6.37%)	3.8066 (2.94%)	1.0618 (10.1%)
	***ρ* (nm)**	7.6514				

Table A-7. Accuracy of the DDMs for $\mu(C_{C,out})$, $\sigma^2(C_{C,out})$, $C_{C,out}^{up}$, and $C_{C,out}^{lw}$ compared to five randomly-generated sample points determined via PCE for *Scenario 2B*.

			$\boldsymbol{\mu(C_{C,out})}$ **(mmol\L)**	$\boldsymbol{\sigma^2(C_{C,out})}$ **(mmol^2/L^2)**	$\boldsymbol{C_{AB,out}^{up}}$ **(mmol/L)**	$\boldsymbol{C_{AB,out}^{lw}}$ **(mmol/L)**
Point 1: MC sampling	***T* (K)**	485.88	1.7733	0.031 78	2.1513	1.3072
	***v* (mm/s)**	10.500				
PCE			1.7750 (0.10%)	0.032 55 (2.44%)	2.1593 (0.37%)	1.3122 (0.38%)
	***ρ* (nm)**	10.263				
Point 2: MC sampling	***T* (K)**	447.82	1.0010	0.017 14	1.2875	0.6656
	***v* (mm/s)**	13.108				
PCE			1.0013 (0.03%)	0.016 35 (4.60%)	1.2894 (0.16%)	0.6814 (2.37%)
	***ρ* (nm)**	11.532				
Point 3: MC sampling	***T* (K)**	467.89	2.3242	0.058 03	2.8216	1.6968
	***v* (mm/s)**	7.3199				
PCE			2.3127 (0.49%)	0.060 25 (3.83%)	2.8263 (0.16%)	1.6854 (0.67%)
	***ρ* (nm)**	10.859				
Point 4: MC sampling	***T* (K)**	473.52	2.1007	0.048 71	2.5739	1.5329
	***v* (mm/s)**	7.6877				
PCE			2.0790 (1.03%)	0.046 16 (5.23%)	2.5254 (1.88%)	1.5267 (0.41%)
	***ρ* (nm)**	11.802				
Point 5: MC sampling	***T* (K)**	463.65	2.6797	0.084 93	3.2917	1.9266
	***v* (mm/s)**	8.7780				
PCE			2.6672 (0.47%)	0.085 88 (1.12%)	3.2847 (0.21%)	1.9272 (0.03%)
	***ρ* (nm)**	7.6514				